DEVELOPMENT OF PREDICTABLE PALLADIUM BASED OPTOMECHANICAL HYDROGEN SENSORS

BY

STEVEN JAMES MCKEOWN

DISSERTATION

Submitted in partial fulfillment of the requirements
for the degree of Doctor of Philosophy in Electrical and Computer Engineering
in the Graduate College of the
University of Illinois at Urbana-Champaign, 2016

Urbana, Illinois

Doctoral Committee:

Associate Professor Lynford Goddard, Chair
Associate Professor Jean Paul Allain
Professor Stephen Boppart
Dr. Peter D. Dragic

ABSTRACT

In addition to its use as an energy storage medium or fuel, hydrogen gas has a variety of commercial applications such as methanol and ammonia production. Given the volatility and flammability of hydrogen, as well as its small molecular size, fast and accurate sensors capable of operating in a variety of environments are necessary. A large subset of hydrogen gas sensors rely on palladium metal, which is known to reversibly react with hydrogen to form palladium hydride. This results in a change in the optical, electrical and mechanical properties of the film. These changes are a result of a change the Fermi level and band structure of the metal, as well as an increase in lattice constant in the presence of hydrogen. The change in complex refractive index plays a role in both reflection/transmission, and for determining resonances or guided modes in waveguides and other sub-wavelength features. However, the increase in the lattice constant of the metal, a process called hydrogen induced lattice expansion, was found to be equally important in modeling the response of the sensors, both from an optical and a mechanical perspective.

This dissertation is concerned with the simulation, fabrication, and testing of palladium based optomechanical sensors, particularly to elucidate the role of hydrogen induced lattice expansion in their design and functionality. Two specific sensor designs: a nano-aperture based sensor and a cantilever based sensor were designed, fabricated, characterized, and modeled. The first sensor developed was based on a single nano-aperture etched into a palladium coated fiber facet. Designed to operate based on the principle of extraordinary transmission and the change in optical constants of the palladium, this sensor showed experimental sensitivity down to 150ppm in transmission and 50 ppm reflection. However, without inclusion of the mechanical effects, the device behavior was unpredictable. Separate work was thus carried out to characterize lattice expansion in thin palladium films using quantitative phase imaging techniques, so that a new sensor could be designed and accurately modelled. This second fabricated sensor consisted of a Pd coated cantilever which operated based on optical probing of mechanical deflections. For more thorough characterization, the cantilever was measured using the same phase imaging techniques. The results of this analysis further improved the understanding of thin film expansion and the capabilities of diffraction phase microscopy for material analysis. Furthermore, this culminated in the fabrication of a sensitive and reliable optomechanical hydrogen sensor whose response matched theory.

To my family, for their unending support.

ACKNOWLEDGMENTS

First and most importantly, I would like to thank my adviser, Professor Lynford Goddard, for his guidance and limitless patience. I would also like to thank my fellow Photonic Systems Laboratory members for all the help and feedback they have given over the years. Special thanks is given to Ben Griffin for helping me with the gas testing as well as Young Mo Kang and Xin Yu for their help with fabrication.

Finally, I would like to thank my sponsors; this work was funded in part by the National Science Foundation under Award ECCS-0901388 and by a research gift award from Cisco Systems, Inc. Some of the simulation work was performed on the Cisco Arcetri cluster. The device fabrication and materials characterization were carried out in the Micro and Nanotechnology Laboratory and in the Frederick Seitz Materials Research Laboratory Central Facilities at the University of Illinois.

TABLE OF CONTENTS

CHAPTER 1

INTRODUCTION

Interest in the development of low cost and accurate trace gas detection platforms has grown recently due to their potential use in a variety of commercial, agricultural, and security industries. Small footprint, unobtrusive, point-based detection of gases or solutes is particularly important since such a device could easily be integrated into existing systems and would allow for high spatial accuracy and modeling for distributed systems. Optical fiber meets these desired criteria since it is cheap and robust, and can have a very small footprint. Optical sensors also offer an inert detection paradigm, have low risk of sparking, negligible electrical interference, a robust material platform that can survive in harsh environments such as high temperature and humidity [1], and the ability to be distributed as a point sensor network covering long distances.

Concern over diminishing fossil fuels and the environmental and ecological issues raised by their use has intensified interest in developing and implementing more sustainable sources of energy. Solar, wind, and geothermal have all seen substantial support as technologies to supplant fossil fuels as our primary source of power generation; however, none of these represent a viable alternative to petroleum based fuels in portable applications. Being both energy dense (by weight) and easily transportable, hydrogen gas is one of the most promising candidates for a replacement fuel and as a storage medium for intermittent energy sources. Hydrogen is also used in methanol and ammonia production, among other applications. A major concern with hydrogen gas is its flammability in air, with a lower explosive limit of 4% [2]. This is compounded by the fact that hydrogen is a small molecule and hard to contain, necessitating early leak detection. Furthermore,

whether in a combustion engine, reactor vessel, or some other process, it is often required to know the exact concentration present.

Unlike other gases, hydrogen does not have a strong optical absorption spectrum, making absorption spectroscopy difficult. Due to this, one of the primary methods for optical hydrogen detection is the use of a functional layer such as a palladium or platinum film [3]. Pd alloys with Ag, Au, and WO_3 have also been studied [4]–[6]. These films catalyze the dissociation of the hydrogen molecule through adsorption, at which point it diffuses into the material. This reaction can change many characteristics of the film such as the conductivity, mechanical properties, and optical properties [7]. For optical sensors, the latter two are important, notably the changes in refractive index and structure of the film. The refractive index describes how light travels through the medium, affecting the optical phase and loss during propagation. Mechanical changes include deformation of the film, which for nanostructures can have a significant impact on device operation.

1.1 Palladium-Hydrogen System

Palladium is known for its ability to absorb large amounts of hydrogen, up to 900 times its own volume [2]. This property makes it attractive for hydrogen storage applications. Furthermore, palladium and platinum films also catalyze the dissociation of diatomic hydrogen, leading to a high absorption rate or facilitating diffusion into other materials. For ideal films, this process is limited by surface adsorption described by the Langmuir equation [8], which for diatomic molecules, the fractional coverage of the surface, θ, is given by:

$$\theta(H) = \frac{\theta_{\max}\sqrt{H/H_0}}{1+\sqrt{H/H_0}}, \qquad (1.1)$$

where H is the hydrogen gas concentration and θ_{max} and H_0 are constants representing the maximum coverage and the concentration for half maximum coverage, respectively. However, for rough films, the Freundlich equation, which is a power law fit:

$$\theta(H) = kH^n, \tag{1.2}$$

where k and n are constants, is more suitable [9], [10]. Even more importantly, this process is also reversible below a certain threshold. Once hydrogen is removed from the external atmosphere, the hydrogen will diffuse out of the palladium and the optical properties of the film can be recovered.

When hydrogen diffuses into the metal lattice, it bonds to interstitial sites creating palladium hydride (PdH). PdH can exist in three states: the α phase which occurs at low concentrations, the β phase which exists at high concentrations, and the α+β phase that exists in the miscibility gap between the two, which is present at normal temperature and pressure. The transition from α to β phase can occur anywhere from 0.1-2% hydrogen and is dependent on the quality and structure of the film [7], [11].

1.2 Optical and Mechanical Properties

As hydrogen is incorporated into the lattice, the electrical, optical, and mechanical properties change. Of interest for the devices presented in later chapters, the changes in optical constants and mechanical structure are most important. The optical constants change as a result of an increase in the Fermi level. The hydrogen atoms bonded at interstitial sites act as electron donors and lead to orbital hybridization with the 4d band of the palladium atoms. The overall result is a

lowering of the density of states at the Fermi level and hence a reduction in the optical transition rate. This causes a decrease in reflection [7], [11], [12].

The change in mechanical structure is a result of hydrogen induced lattice expansion (HILE) in the palladium film. The incorporation of hydrogen into the lattice results in an increase in the lattice constant from the bulk value of 3.890Å to 4.025Å at the onset of the β phase [7]. However, for nanoscale devices, the effects of strain resulting from bonding and deformation mechanics at vertices or edges, such as along the perimeter of the aperture, play a large role. The entire film cannot expand equally in all directions, as this would amount to several microns of expansion laterally across the bonded film. Since Pd bonds weakly to oxides, this could result in buckling of the film in places and an unknown exact change in shape of small features. Even an alteration of a few nanometers could have a large impact on the spectral response of small resonant structures. Research has been done to investigate the mechanics of HILE for thin films and nano-scale structures and will be presented in Chapters 4 and 5 [13], [14].

1.3 Current Research

The Pd-H system has been used in the development of a variety of optical hydrogen sensors ranging from plain film monitoring [15] and functionalized lasers [16]–[19] to specialized nanostructures such as apertures [20] or antennas [21]. There has also been significant work on developing fiber optic based hydrogen sensors. Most designs use a thin Pd layer either along the fiber length or at the fiber tip to alter the amplitude or phase of the light interacting with the layer. One of the earliest designs, a Mach-Zehnder fiber optic interferometer with a Pd coated fiber as the sensing arm, was realized in 1984 by Butler [22].

The most basic fiber sensor is simply a cleaved facet coated with palladium or some other reactive material. These “fiber mirror” designs are some of the simplest and were demonstrated in

1994 by Butler [23]. Such devices were fabricated with varying film thicknesses and the change in reflected power was measured as the fiber was exposed to a wide range of hydrogen concentrations. Results showed around a 3% power decrease at 0.5% hydrogen and up to a 20% power decrease at 2% hydrogen in nitrogen for a 10nm thick film.

More interesting however, was the identification of an additional contribution to the reflected power change in these sensors, besides the change in the refractive index. Due to film expansion (HILE), micro-blistering and micro-cracking of the films were seen. The micro-blistering depended highly on surface adhesion between the Pd film and the substrate. Further, it was reversible, at least for some time. The presence of this effect did not depend on film thickness directly, but rather was a function of bonding, and hence deposition conditions. The contribution of these two effects to the reflectivity change was very large, with a $\Delta R/R = 80\%$ at 10% hydrogen for some films. By depositing films with random thicknesses, other values for $\Delta R/R$ of 23% and 7% were found, which most likely correspond to varying states of film clamping.

To test this, Butler also fabricated sensors with a Ni adhesion layer to provide a solid bond between the Pd layer and the substrate. These sensors showed a reduced response in reflectivity, regardless of Ni layer thickness. This suggests that the reduction was due to a bonding effect, rather than some kind of alloying. The sensitivities of these fully bonded sensors also matched very closely to the $\Delta R/R = 7\%$ for the plain Pd films, suggesting those were samples with abnormally high adhesion between the SiO_2 and Pd. These simple facet mirror based sensors required very little fabrication and demonstrated a large sensitivity of nearly 10% per percent of H_2 when measured in reflection. Response times were not discussed, but should be comparable to other Pd hydrogen sensors with similar film thicknesses. These results, specifically the microblistering, will

be important later in the analysis of the nano-aperture sensor. Some more thorough reviews and comparisons of hydrogen sensors in general can be found in [3], [24], [25].

CHAPTER 2

NANO-APERTURE FIBER SENSOR: TRANSMISSION

In an aperture with minimum dimensions comparable to, or well above, the wavelength of light in the enclosed media, the majority of the propagating mode's energy resides in the cavity formed by the aperture. However, for extremely sub-wavelength apertures, the transmission drops rapidly as a function of w/λ^4, where w is the size of the confining direction and λ is the wavelength of light in the aperture cavity media [26], [27]. For sub-wavelength metallic apertures, or nano-apertures in the visible-NIR regime, propagating surface plasmon polaritons (SPPs) allow for enhanced throughput, or so-called extraordinary transmission. SPPs are collective oscillations of surface charge on a dielectric-metal interface that result from a coupling of the electromagnetic field to the charges on the metal surface [28]. In certain configurations, such a wave can propagate along a metal interface for several microns or more at optical frequencies, despite the expected loss introduced by the metal [29]. Furthermore, due to the high permittivity of the metal, the wavelength of a SPP can be extremely small leading to a highly confined field inside the aperture. Specifically, this wave propagates along the interface, placing the majority of the energy along the aperture boundaries, rather than in the aperture cavity [30]. This coupling of the field to the SPP aperture mode can be highly resonant in the appropriate frequency range depending on the metal and aperture dimensions [31].

These metallic nano-apertures and cavities are interesting from a sensing standpoint due to the highly localized fields, potentially strong resonance, and high power throughput [32]. For a sensor based on a functionalized metal coating, this is ideal because the field transmitted through the aperture is localized primarily along the metal interface, rather than in the aperture cavity,

which is away from the functional material. Not only does the nano-aperture confine the light to the functional layer, but due to resonant effects resulting from SPP coupling and excitation, changes in the transmission and reflection due to a change in optical properties of the metal or physical dimensions of the aperture are amplified.

The resonance of the aperture is determined by the aperture dimensions and the material properties of the metal [33]. The effects of aperture dimensions can be broken down into three sections. First, there is the scattering and excitation of surface plasmons from the light incident on the aperture. Second, there is the propagation of the light through the aperture, which can be thought of as a small metallic waveguide. Finally, there is back-scattering from the exit port of the aperture and decoupling of the SPPs back into a transmitted field. The modes of the metallic waveguide primarily determine the resonance of the aperture [31]. For rectangular waveguides, these can be broken down into metal-dielectric-metal (MDM) or metallic slot waveguides, and dielectric-metal-dielectric (DMD) or metallic ridge waveguides [34]. MDM waveguides have higher loss, but more localized confinement of the field, which is more useful for a Pd based hydrogen sensor. For sub-wavelength MDM waveguides, the field is localized along the metal interfaces that are perpendicular to the incident polarization. This results from sub-wavelength dimensions being needed to maintain coupling between the SPPs on each metal interface, and from the zero tangential electric field boundary condition on Maxwell's equations. For the fundamental mode, transverse electric (TE_{10}), the cut-off frequency is determined by the length of the longest side of the rectangle. Hence, the transmission through a rectangular nano-aperture can be spectrally tuned by changing the size parallel to the incident polarization. An optimal gap distance can also be found to maximize the transmission for a given wavelength.

Based on this waveguide formulation for nano-aperture transmission, several variations on rectangular apertures were proposed, notably the ‘C’ and ‘H’ apertures [31], [35]. The C aperture was shown to have highly resonant transmission and a large increase in power throughput compared to a rectangular aperture with the added benefit of producing a largely circular output beam. For these reasons, the C aperture was chosen for use in designing a single nano-aperture palladium based hydrogen sensor.

As mentioned earlier, sensor designs using a plain palladium facet mirror offer several advantages over FBGs or tapered fiber designs. They are simple to fabricate and can work at multiple wavelengths for self-referencing or can be measured with a broadband light source without the need for a spectrometer or tunable laser. FBGs can be expensive depending on the desired wavelength and reflection spectrum, and tapered fiber designs can involve wet etching of the cladding which must be done in a controlled manner. Furthermore, tapered fiber designs result in an inherently fragile sensor since the protective layers of the fiber have been etched away. By themselves, facet mirrors do not offer the sensitivity of FBGs or tapered fiber sensors; however, by incorporating nanostructures onto the facet, higher sensitivity and easier self-referencing can be achieved while maintaining the small form factor of a facet at the cost of some fabrication complexity. Chapters 2 and 3 will focus on the design and experimental analysis of such a device as presented in [20], [36]–[40].

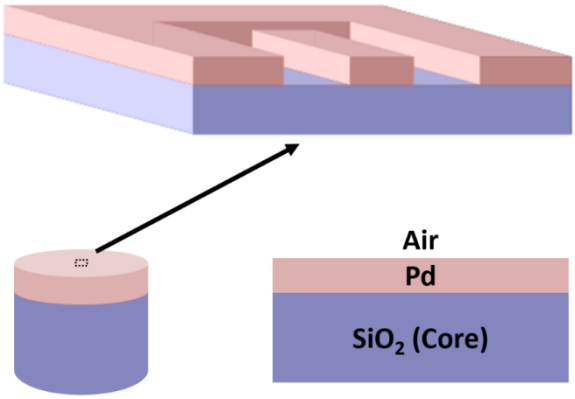

Fig. 1: Schematic of the C-shaped nano-aperture optical fiber hydrogen sensor. Figure adapted from [38].

The on-fiber layout for the nano-aperture sensor is shown in Fig. 1. By integrating the sensor onto the fiber facet, as opposed to along its axis, the footprint of the actual sensing region is greatly reduced and spatial accuracy is enhanced. Furthermore, a bundled array of sensors with different functionalized metals can be placed in close proximity for the determination of the various constituent concentrations in a gas mixture. Since the optical properties of sub-wavelength apertures are highly dependent on the material properties, changes in the palladium layer will couple to changes in transmission and reflection by affecting the guided surface plasmons in the nano-aperture. The transmission and reflection spectra of the aperture are simulated to determine the optimal dimensions for a given aperture type or shape in order to maximize the transmitted or reflected power, improve signal-to-noise ratio (SNR), or improve the sensitivity; the latter requiring the optical properties of the film as a function of the analyte to be well known. The C aperture demonstrates extraordinary transmission, providing both high power as well as resonant characteristics. This aperture is also asymmetric, which produces different responses and sensitivities for different polarizations of light and thus has a functional polarization dependent loss. Such a mechanism allows for self-referencing and the reduction or elimination of common

mode noise along the fiber. There are several methods for fabricating micro and nano-structures on a fiber tip such as traditional or nano-imprint lithography and film transfer. For accurate and versatile prototyping, focused ion beam (FIB) milling can be used to etch the aperture. This technique allows for in-situ monitoring of the fabrication, as well as the fabrication of sensors with a variety of parameters.

Along with the C aperture, circle apertures and plain-film sensors also show a hydrogen response and can be used as controls to measure the effect of aperture shape and to demonstrate the presence of a polarization dependent sensitivity. The devices can be used in both transmission and reflection (Chapter 3) by using a detector opposite the facet and an optical circulator, respectively. To experimentally test the apertures, special care needs to be taken so that the gas flow and pressure can be accurately controlled. As a sensing metric, the fractional change in transmitted or reflected power can be measured. In transmission mode, the C aperture demonstrates a sensitivity much larger than that of both the circle and plain film designs, showing the importance of using structures with resonant or extraordinary transmission. The magnitude of the change was about 3 times larger compared to the circle aperture and eight times larger compared to the plain film, improving the SNR and allowing for the detection of lower concentrations of hydrogen.

2.1 Aperture Design & Simulation

To use this information to maximize the performance of a structured optical device, such as a nano-aperture, simulation techniques such as the finite-difference time-domain (FDTD) method and the finite element method (FEM) can be employed to model the spectral response as a function of device parameters. The reflection and transmission properties of C apertures have been studied in general, but the properties of the materials used play an important role. In the case

of the hydrogen sensor described in Fig. 1, the optical properties of the palladium layer as well as the three dimensional (3D) nature of the problem must be taken into account. A fundamental problem with simulating this structure in 3D is the widely varying dimensional scales of the device.

To accurately simulate the fiber, a cross section several tens of microns in diameter must be modeled. Coupled with the nanometer scale of the aperture, this represents an extremely large computational domain when meshed, which is unfeasible to simulate on most standard computer systems. Given the large mismatch of modes and the radiative nature of the aperture, mode matching is also difficult to employ. However, if the film is optically thick, then only transmission through the aperture is important. Furthermore, the reflection from a plain film is easily understood in terms of the Fresnel equations [41], and the aperture only has a localized effect. Therefore, the overall reflection can be thought of as a superposition of the surrounding plain film region and the aperture region. Some results are included here, but a more thorough discussion of the reflection simulations will be given in Section 3.2 where a computing cluster was used to expand and verify the data shown here.

To model the aperture, a thin cross section of the facet can be simulated using FDTD and FEM. For FDTD simulations, the dispersion of the palladium film can be taken into account through a Lorentz-Drude oscillator model [42]

$$\varepsilon_r(\omega) = 1 - \frac{f_0\omega_p^2}{\omega(\omega - i\Gamma_0)} + \sum_{j=1}^{k} \frac{f_j\omega_p^2}{(\omega_j^2 - \omega^2) + i\omega\Gamma_j}, \qquad (2.1)$$

where ε_r is the relative permittivity, ω is the optical frequency, Γ_j is a damping term, ω_p is the plasma frequency, and f_j is the oscillator strength for the j^{th} interband resonance; f_0 and Γ_0 relate to intraband effects. Since the aperture overlaps a small portion of the center of the fundamental

mode, the incident guided mode can be approximated by a plane wave here, removing the need to simulate the entire optical fiber. Thus, only a small area around the aperture is simulated. Furthermore, by using a Gaussian impulse excitation and taking Fourier transforms, the transmitted and reflected power can be found across a range of frequencies with a single FDTD simulation.

FEM can also be used to model the transmission and reflection by using a frequency sweep and the plane wave excitation can be modeled by a current sheet. Both techniques can also be used to obtain the electric and magnetic fields of the modes propagating inside the aperture. Electric field profiles along with the corresponding aperture design can be seen in Fig. 2. Bulk values for the refractive index of the palladium film are used [42] and the thickness is set to 150nm. As expected, the simulations show the field strongly confined to the air-palladium interfaces that are perpendicular to the incident polarization. There is also a polarization dependence given the asymmetry of the aperture. These two modes are referred to as quasi-transverse electric (quasi-TE) and quasi-transverse magnetic (quasi-TM), where quasi-TE has a majority E_x field and quasi-TM has a majority E_y field. However, these modes are hybrid modes and E_x and E_y cannot actually be fully decoupled. Excitation of the quasi-TE and quasi-TM depends on the input polarization, with an E_x polarized input field producing a quasi-TE mode, and an E_y input producing a quasi-TM mode. Since these two modes propagate in different parts of the aperture and have different overlap with the Pd layer, it is conceivable that they would have different magnitudes of their response to hydrogen-induced changes. This is indeed the case and will be experimentally shown in Section 3.5.

The smaller aperture in Fig. 2b is a typical design for a C aperture. However, for a sensor based on transmission changes, it is useful to maximize both the total transmitted power to improve

the SNR as well as the differential response due to hydrogen induced changes. Modeling hydrogen induced changes requires specific knowledge about how such a nanostructured film expands, as well as accurate refractive index data as a function of hydrogen concentration. While general trends are known, these are both areas of continuing research [43], [44]. It is easy, however, to optimize the structure so that there is a transmission peak at or near the target wavelength without hydrogen present. To maintain low cost, it is desirable to operate in the telecom band near 1550nm. As was mentioned previously, the transmission peak can be altered the most by changing the arm length and waist gap. A second aperture design is the longer aperture shown in Fig. 2a where the transmission peak has been shifted to be near 1550nm for the quasi-TM mode. The quasi-TM reflection and transmission spectra for this new design can be seen in Fig. 3 compared to the original C aperture in Fig. 2b. This particular aperture was also designed to emphasize the polarization difference and resolve a fabrication problem that arose from having too short of a ridge.

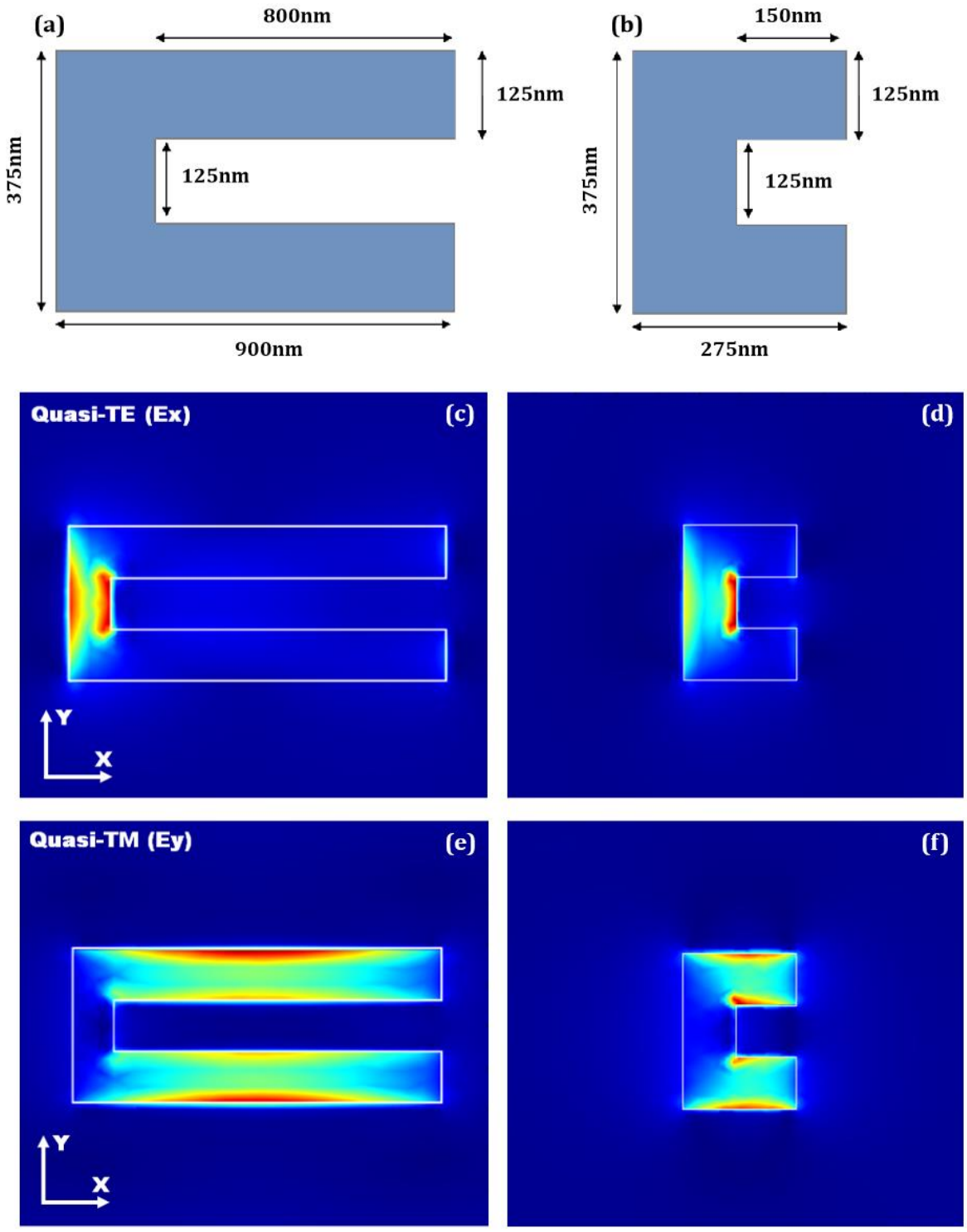

Fig. 2: (a) Nano-aperture design used to fabricate devices for experiment. (b) Typical C aperture design. (c-f) Electric field profiles for the two aperture designs. Adapted from [20], [38].

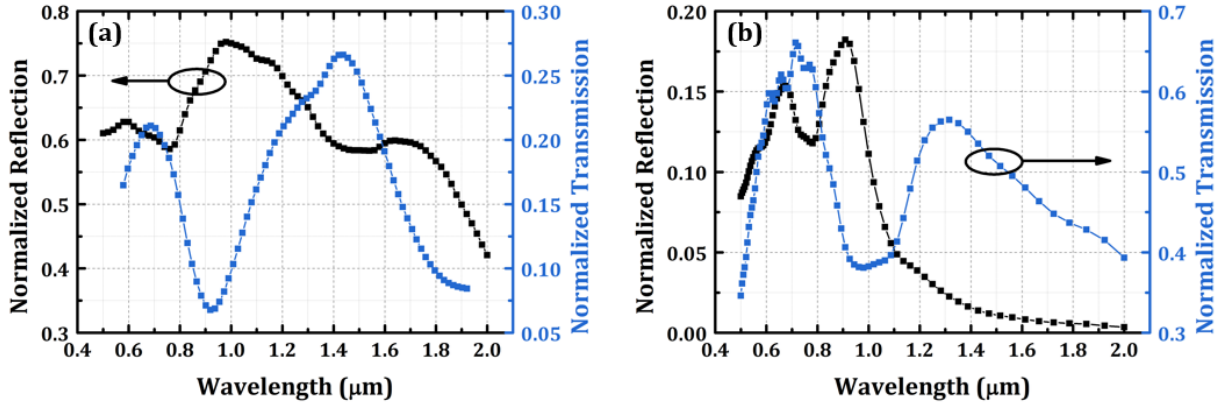

Fig. 3: Reflection and transmission of the quasi-TM mode for the (a) exaggerated and (b) typical C aperture. Adapted from [38].

2.2 Fabrication and Experimental Setup

Based on these concepts, transmission based hydrogen sensors using plain films and facet-etched nano-apertures have been fabricated and experimentally verified. Fabrication was done by cleaving pieces of optical fiber and coating them with palladium using electron beam evaporation. For the aperture sensors, apertures were milled using a focused ion beam (FIB). It has been reported that Ga+ ion implantation into the fiber substrate from the beam can result in an increase in loss in the SiO_2 layer [45], which would be detrimental to sensor performance. Thus, for the transmission based sensors it was ideal to minimize etching into the substrate. It was found that this was not entirely possible, resulting in a minimum etch depth of 50-100nm for the apertures.

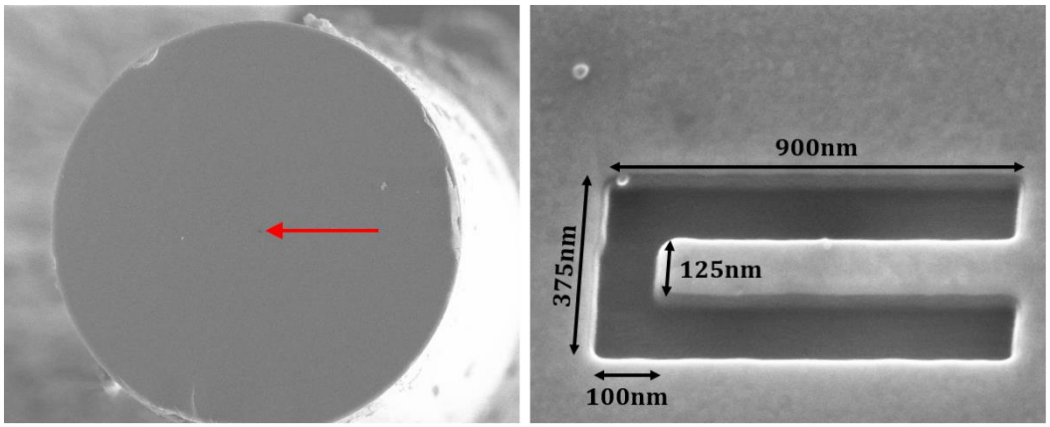

Fig. 4: Scanning electron microscope (SEM) images of a fabricated Pd nano-aperture sensor with design dimensions. The film thickness was 150nm.

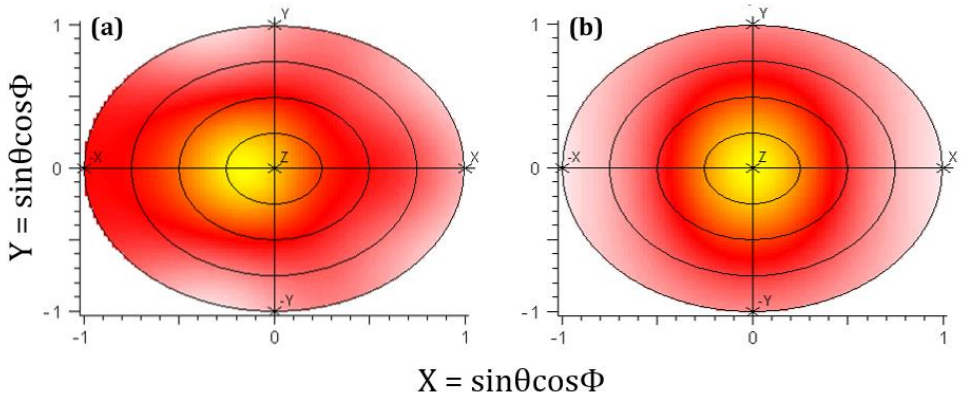

Fig. 5: Simulated far-field radiation patterns along the z-axis for the (a) quasi-TE and (b) quasi-TM modes of the fabricated C aperture. Figure adapted from [38].

Also, due to the insulating substrate, the resulting charge build-up can produce uneven or lateral over-etching of the aperture, particularly the ridge. Images of a well fabricated C aperture with the same dimensions as Fig. 2b can be seen in Fig. 4. Much work was done fine tuning the etching and tool parameters to optimize the etch. These aperture dimensions will be the same for all of the work to be presented, unless otherwise noted.

Since the light in the aperture is going from a highly confined mode to free space there will be significant diffraction resulting in a diverging beam at the output. The radiation patterns for

such an aperture can be seen in Fig. 5 for the two modes. In order to capture this light, a high numerical aperture (NA) lens near the sensor head is required. The light is then focused onto a detector, but could also be coupled back to an output fiber for remote measurements.

A typical measurement setup is shown in Fig. 6. An optical splitter is used to monitor input power so that the output can be normalized. An optical isolator is used to prevent feedback into the laser cavity and a polarization controller or polarization scrambler is used to respectively set or randomize the input polarization of the light going to the sensor. An optical circulator can then be used to collect reflection data in addition to transmission. After the sensor head is spliced back to fiber, the tail end is connected to the laser input and the head is placed in a flow chamber for testing with a detector to monitor the transmission. Gas flow and data acquisition from the detectors can then be controlled and recorded through the use of LabVIEW. In a standard pulse measurement, the sensor is exposed to a certain concentration of hydrogen in nitrogen and then purged with nitrogen for a set amount of time. This is then repeated for as many concentrations or pulses as needed.

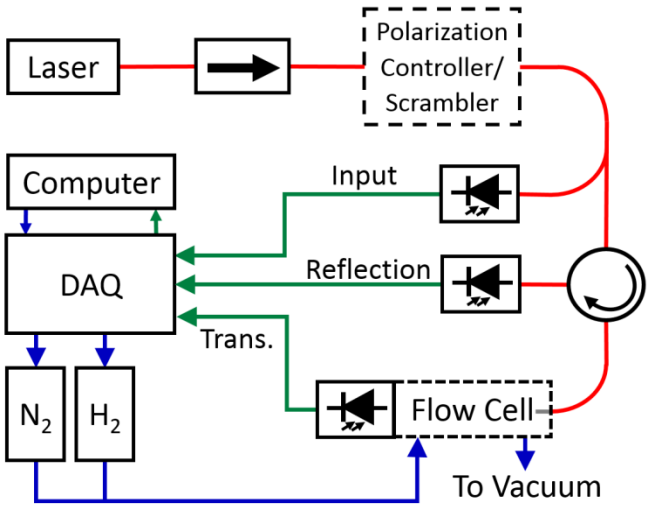

Fig. 6: Schematic of the typical experimental setup. Red denotes fiber paths, green denotes data acquisition, and blue denotes gas flow and gas flow control.

2.3 α-Phase Measurements

Using this control and measurement setup, the nano-aperture sensor was investigated in several different ways. Initially the behavior of the sensor at low concentrations in the α phase was studied. As a metric, the change in transmitted power is measured relative to the power in nitrogen ambient after being mounted in the flow chamber. The input polarization is kept fixed using a polarization controller and copious amounts of tape. To test, the sensor is exposed to increasing hydrogen concentration pulses of 30 minutes, separated by 30 minutes of nitrogen until the β phase transition becomes apparent.

In this experiment, several sensor types are tested for comparison purposes. These include the same C aperture as before, a circular nano-aperture with equal area, and a simple plain film facet mirror sensor. The sensors were tested down to 0.25% hydrogen in nitrogen and the change in transmitted power was measured. A time-domain plot of the pulses and the associated change in transmission for each sensor are shown in Fig. 7a. The response of the sensor is then defined as the average over the last 5 minutes of the pulse, averaged across several pulses. These results are shown in Fig. 7b for each type of sensor on a semi-log plot.

The response times for each type of sensor were the same order of magnitude, varying from 4 to 10 minutes depending on the hydrogen concentration. This is because the response time is largely determined by the diffusion and adsorption rates of the Pd film, as well as the thickness, which is the same for all three designs. On average the aperture sensors responded slightly faster because of the shallow penetration depth of the guided mode. Since this is mostly a surface phenomenon as opposed to a volumetric one, these regions quasi-saturate faster. The C aperture sensor, however, showed a much larger magnitude of response to hydrogen than the plain film, and the circle aperture was in-between. This is attributed to the extraordinary transmission

resulting from guided modes in the C aperture. The circle aperture lacks the MDM or DMD waveguide structure present in the C aperture and therefore its modes are less confined than the C aperture modes. Thus, the circle aperture is less affected by changes in the refractive index or dimensions of the aperture walls. The C aperture showed a maximum response of 13% at 1% hydrogen and a response of 8.5% at 0.25% hydrogen, whereas the circle aperture only reached a 4.5% power change, and the plain film only had a 1.8% power change at 1% hydrogen. Compared to the value measured here, and the reported value of a 3% change at 0.5% hydrogen by Butler for a plain film, the aperture sensor features a transmission change almost an order of magnitude higher.

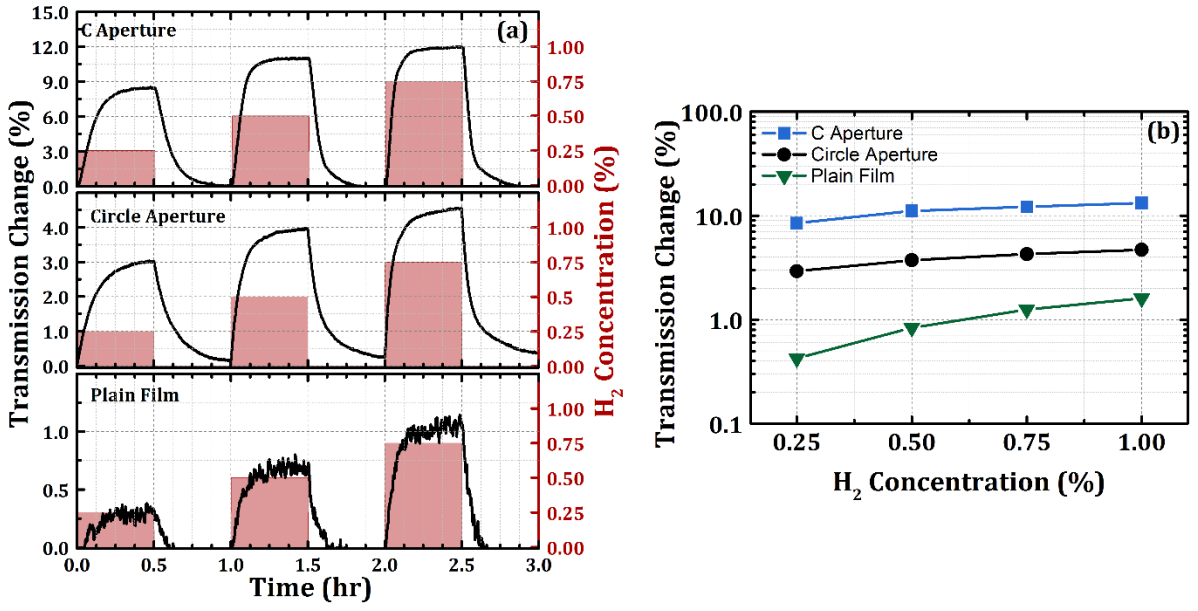

Fig. 7: (a) Pulse measurements showing the time dependent response of the three sensor types for various hydrogen concentrations. (b) Semi-log plot of the response of each sensor type versus hydrogen concentration. Adapted from [39].

2.4 β-Phase Measurements

Another area of interest is the behavior of the sensor at high hydrogen concentrations, above the α-β phase transition. Here, only data for the C aperture sensor is presented. The sensor is again exposed for 30 minutes at the target concentration and 30 minutes of nitrogen to purge. The phase change can be seen starting at concentrations of around 1.5% in Fig. 8a, as evidenced by a second increase in the measured transmission. Up until a certain point in time, determined by the diffusion coefficient and adsorption, the film will remain in the α phase or in the miscibility gap even though the ambient concentration is high enough for a transition to the β phase. After enough hydrogen diffuses into the lattice, the film will enter the β phase and the optical and mechanical properties will begin to rapidly change again. It is also worth noting the relatively large change in transmission after the film enters the β phase. The sensitivity to hydrogen in the β phase is much larger than in the α phase, due to a larger change in the film's properties. In general, the concentration at which this occurs is a property of the film and is highly dependent on the deposition conditions and thickness.

It has been suggested that exposure to high concentrations of hydrogen can act to "work harden" the material [46]. However, it is also known that prolonged exposure to high concentrations can also degrade film quality [7]. To evaluate this, the sensor was also exposed to alternating 15 minute pulses of 5% hydrogen in nitrogen and 0.75% hydrogen in nitrogen with 15 minute nitrogen purges interleaved. The 5% pulse is above the α-β phase transition threshold. In this regime, the PdH film enters the β phase and undergoes plastic deformation. The results of this can be seen in Fig. 8b and 8c. Overall this process slightly improved the response magnitudes and response times; however, an interesting side effect was the behavior of subsequent low concentration pulses. The response there seemed to cycle between a power increase and a power

decrease, with each 5% pulse advancing the location of the low concentration response in the cycle. This can be seen in Fig. 8d and 8e which plots the 0.75% traces labeled incrementally. The response to 5% hydrogen was always a large power increase, whereas the low concentrations alternated. This behavior was repeatable in that the response at low concentration was monotonic until it was again exposed to a large hydrogen concentration. The exact cause of this is unknown, but it is most likely attributable to plastic deformation and very slow relaxation of changes induced during the β phase.

Also noticeable with the 5% pulses is the consistent delay in response and the lack of the "kink" seen in Fig. 8a. This is most likely due to the large concentration gradient immediately transitioning the surface to the α+β or β phase and not allowing the film time to relax as it expands. Because this process happens so quickly and randomly it creates a lot of noise rather than the smooth transition seen in Fig. 8a. Note that the magnitude of the "noise" is comparable to the magnitude of the power change at 0.75%.

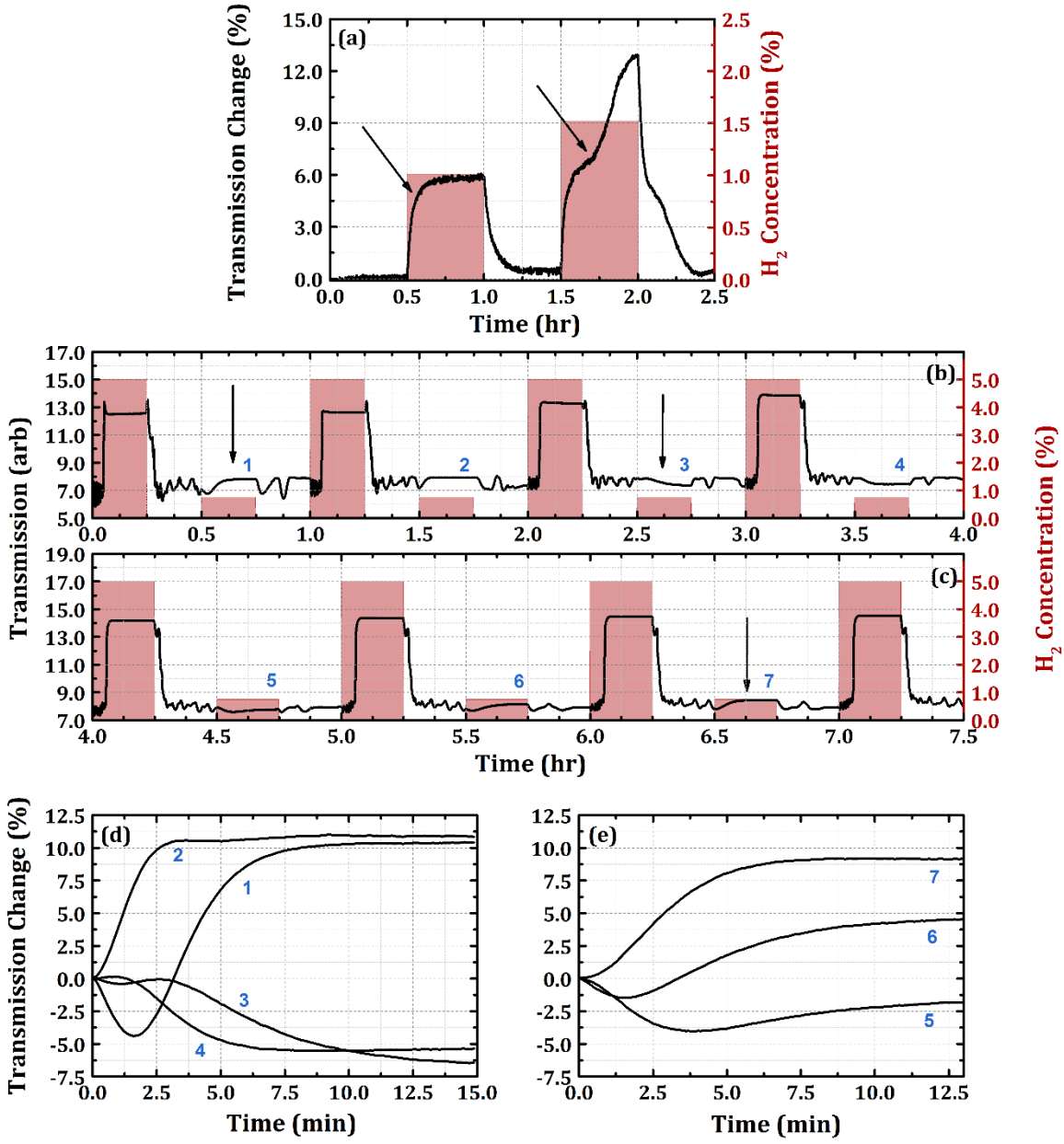

Fig. 8: (a) Sensor response at high concentrations; the kink in the transmitted power denotes the onset of the β phase. (b, c) Pulse test for the sensor alternating between 5% hydrogen and 0.75% hydrogen; arrows highlight the unusual effect of the 5% hydrogen on the subsequent low concentration pulse. (d, e) Traces of the labeled low concentration pulses show the change in temporal response as a result of exposure to the 5% hydrogen. Figure adapted from [39].

2.5 Polarization Dependent Loss

A final property of the C aperture sensor to measure in transmission is the polarization dependence and in particular the polarization dependent loss (PDL), which as discussed is a result of the two asymmetric modes of the aperture. These measurements were carried out in the same way as the prior pulse tests, except that a polarization scrambler was used to continuously vary the input polarization and thereby sample all possible states of input polarization. This is necessary since without polarization maintaining fiber it is difficult to know the orientation of polarization with respect to the aperture. The scrambler cycles through the entire Poincaré sphere at 10Hz. Data was acquired at 15 kHz for 1s so that the polarizations of minimum and maximum transmission could be properly sampled. A median filter was applied to remove spikes arising from the non-uniform sampling of the polarization states. Since the transmission change is monotonic over the test concentration range for any polarization state and the two modes can be well approximated as orthogonal, they can be extracted by measuring the minimum and maximum of the transmitted power over some period as long as the response curves for the two polarizations do not cross. Such a crossing would be indicated by kinks in the response curves, as well as a crossing or contact point which was not observed. Comparisons of measured power to simulated data are difficult to make because of the sensitivity of the quantity to detector alignment. However, as seen in Fig. 5, there is significant overlap in the radiation patterns for the two modes; hence, the measured and simulated PDL, i.e., the TM/TE power ratio, should be close. For the fabricated aperture, the measured PDL was 2.9, while the simulated value gave a ratio of 3.3. This discrepancy is easily within errors introduced by the uncertainties in the film thickness and its refractive index, which can vary for thin films, as well as fabrication imperfections such as over-etching.

The polarization response for the C aperture in transmission, as well as the circle aperture and plain film sensors can be seen in Fig. 9. As expected, the circle aperture and plain film sensors show no polarization dependence. Response curves similar to Fig. 7b can be found for the two states and roughly fit to a line in the 0.5-1% H_2 region. From this, an approximate sensitivity can be calculated. This corresponds to a 3.8% increase in power per percent hydrogen for the minimum transmission polarization and a 5.7% power increase per percent hydrogen for the maximum state.

The C aperture, however, shows both a difference in transmitted power between the two polarizations as well as a dependence of the PDL on hydrogen as shown in Fig. 10. A 0.07dB increase in the PDL was measured at 0.25% hydrogen, and a 0.14dB increase was measured at 1% hydrogen. Since both modes must propagate through the same fiber and radiate to the same detector over the same path, as long as a sufficiently high NA lens is used, the PDL is a self-referencing sensing metric that can be used to reduce common mode noise from mechanical disturbances to the fiber or changes in detector alignment.

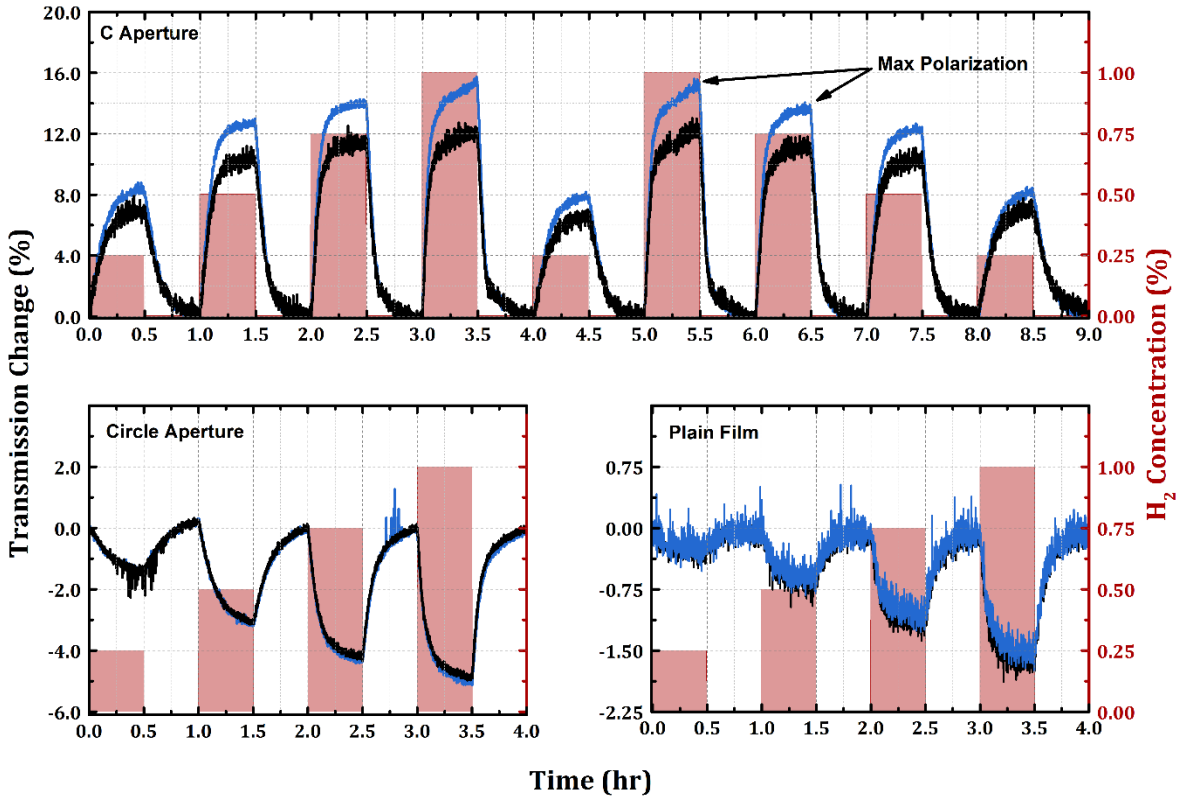

Fig. 9: Response of the minimum (black) and maximum (blue) transmission polarization for each sensor type versus time. Figure adapted from [39].

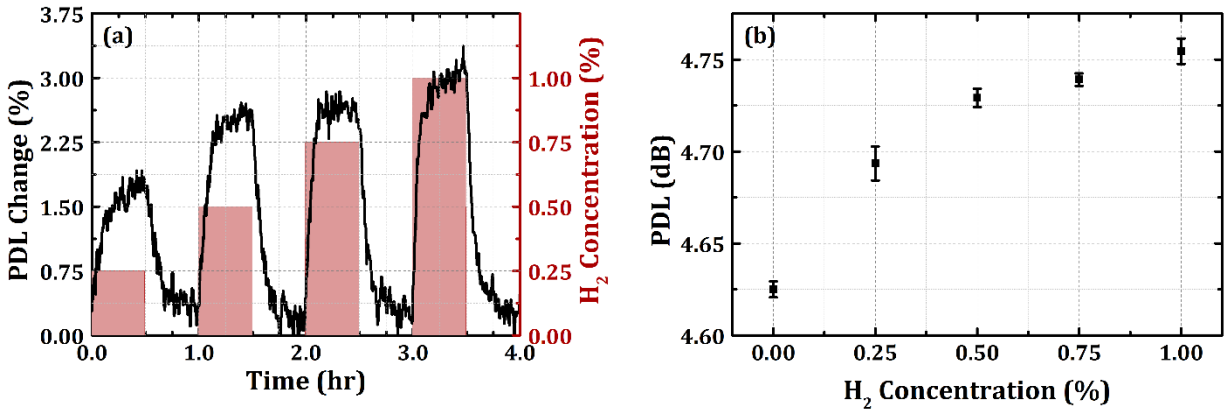

Fig. 10: (a) PDL of the C aperture versus time during a hydrogen pulse test. (b) Summary of the PDL response versus hydrogen concentration. Figure adapted from [39].

2.6 Discussion

For trace gas detection, specifically the detection of hydrogen, nanostructures such as apertures can be used to enhance the change in optical properties of the functional layer. A fiber sensor consisting of a palladium film with a single C-shaped aperture etched over the core was fabricated and compared experimentally to a simple plain film structure to show the increase in response due to the presence of the aperture. The C aperture was also compared to a circle aperture to show that aperture shape, and not just aperture size, can greatly affect the sensitivity of the device. Such a device offers a substantial improvement in hydrogen sensitivity over plain film sensors with minimal added fabrication complexity. The sensor was tested in several ways. The response to hydrogen in both the α and β phases of PdH was measured, showing a sharp increase at the onset of β phase and evidence of deformation of the film. The polarization dependence of the aperture was also investigated, revealing a hydrogen dependence in the PDL of the sensor. The C aperture showed high sensitivity well below the lower explosive limit of hydrogen in air of 4%. A summary of the results for the various sensors and configurations can be found in Table I.

Table I
Nano-aperture Sensor Performance

Mode	Sensor	ΔP at 0.25% H_2	ΔP at 1% H_2	Sensitivity: $\Delta P/\Delta H_2$ for H_2 between 0.5 and 1%
Transmission	C Aperture, TE (Max)	8.5%	15.3%	5.6
	C Aperture, TM (Min)	6.9%	12.0%	3.8
	Circle	2.9%	4.7%	1.9
	Plain Film	0.4%	1.6%	1.5
	PDL	0.07dB	0.14dB	0.09 dB per %H_2

CHAPTER 3

NANO-APERTURE FIBER SENSOR: REFLECTION

Interestingly, in reflection mode, both the C and the circle apertures presented in Chapter 2 show an order of magnitude improvement in sensitivity over the plain film. A change in reflected power of almost 20% at 0.25% hydrogen was demonstrated for the C aperture, over double the value for the same sensor when measured in transmission. From an implementation standpoint, reflection based sensing is preferred to transmission based. A reflective sensor is less invasive than a transmissive sensor in that only a single tiny entry point to the gas volume is needed. This entry point only needs to be wide enough for the tip of the fiber sensor to fit. This results in an extremely small sensor footprint and allows for true point-based detection. In comparison, a transmissive sensor needs both an entry and an exit point and possibly also free space optics in the gas flow volume to couple between the two. This can possibly disrupt the gas flow. Furthermore, the output from the reflective sensor is not affected by detector misalignment since the light is intrinsically coupled back into the fiber. This direct coupling allows the reflected light to then be directed to the measurement and control system, which can be co-located with the laser source, e.g. at a remote facility.

3.1 Sensing Mechanism and Initial Results

In reflection mode, the presence of a nano-aperture would not be expected to produce a noticeable effect in the overall reflection since the reflection from the surrounding film should be dominant. However, Fig. 11 shows that this is not necessarily the case for the nano-aperture sensor

types when tested with a fixed polarization that maximizes the reflection. These results also show a much smaller difference between the C and circle apertures than the transmission mode results. This suggests that the physical mechanism for the enhanced sensitivity in reflection mode might not be an aperture resonance effect since the resonances would be different for the two aperture types. Instead, simply the presence of an aperture seems to be enhancing the sensitivity. Such an effect could arise if the surrounding film has very low reflectivity, which can happen if the film is sufficiently rough. Given the poor adhesion of Pd to oxide and the expansion of the film, this could result from localized buckling or a micro-blistering effect similar to that demonstrated by Butler. In addition, it may be possible that FIB etching process somehow clamps the film to the substrate in the vicinity of the aperture. At the moment the correlation between the presence of the aperture and the increase in sensitivity is not fully understood. As will be shown later through simulations, however, the large change in reflected power is most likely related to mechanical properties of the film.

One possible explanation is that since the reflections from the aperture and film are coherent, there will be interference between the two fields. It is expected then that the etch depth can be optimized to maximize the sensitivity of the reflectance to hydrogen. An etch depth study etching through the Pd and into the SiO_2 fiber substrate was conducted and those results will be presented in the next section.

The fabricated C apertures have dimensions of W_a = 900nm, W_b = 100nm, H_t = 375nm, and H_b = 125nm [20], [31]. The apertures were etched through focused ion beam milling (FIB) with an FEI Dual-Beam DB-235 FIB/SEM into a 200nm thick film [20]. In addition to etching through the metal functional layer, the SiO_2 fiber tip was also etched to a controlled depth of 100-1100nm. Due to charge build up from ion implantation, the sidewalls of the aperture slope inward

as the etch depth increases. This effect can be seen in Fig. 12a, which shows a fabricated aperture. After fabrication, the apertures were packaged in a protective polymer and metal jacket and spliced back onto connectorized SMF-28e fiber for testing.

A schematic of the experimental setup can be seen in Fig. 12b. The light source was a 1550nm laser which was passed through an optical isolator and a polarization controller. A 99/1 splitter was used to monitor the input power, and an optical circulator was used to measure the power reflected by the sample. The photodetector voltages were measured using a data acquisition (DAQ) card on a computer running LabVIEW. The fiber tip sensors were mounted in a machined polycarbonate flow chamber. The flow rates through the chamber were controlled in LabVIEW using the DAQ to set the nitrogen and hydrogen mass flow controllers (MFCs), respectively. The sensors were exposed to hydrogen concentrations ranging from 90 to 10000 ppm with a cycle of 30 minutes hydrogen in nitrogen mixture and 30 minutes pure nitrogen. The lower limit was determined by the mass flow controllers and the upper limit was chosen to remain below the α-β phase transition.

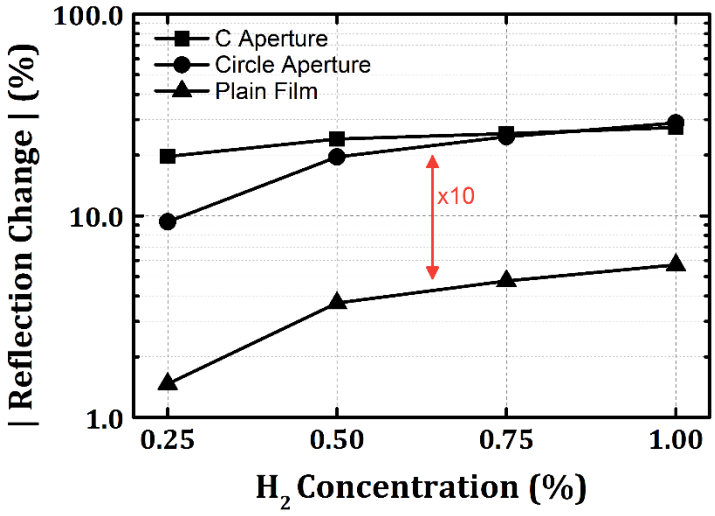

Fig. 11: Summary of the response in reflection for the three sensor types.

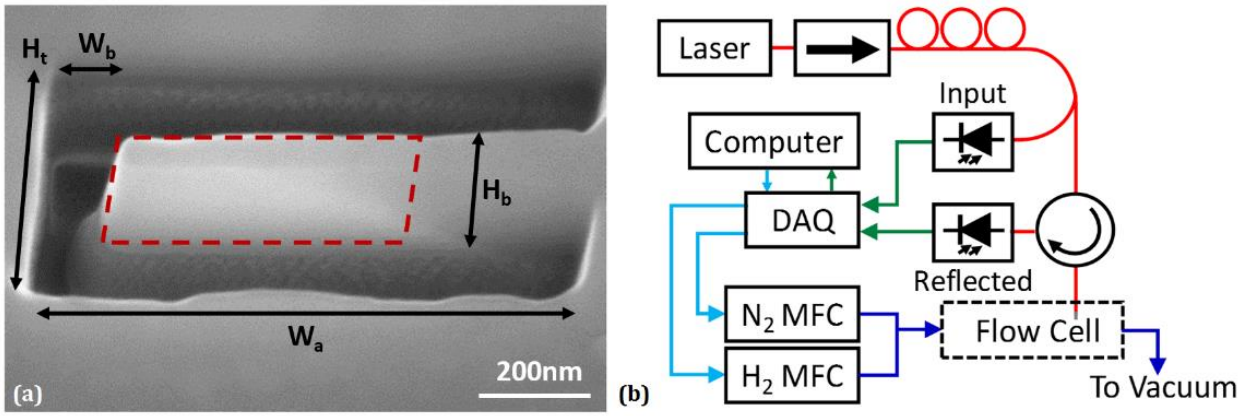

Fig. 12: (a) SEM image of an aperture, the discoloration of the 125nm ridge in the highlighted box is caused by over-etching. Dotted lines at the edges of the ridge serve as a guide for the eye. (b) Schematic of the experimental setup showing the optical fiber path in red, the fiber sensor tip in gray, the electrical measurements in green, the voltage control signals in cyan, and the gas flow path in blue.

3.2 Effect of Etch Depth

Measured data for a C aperture etched to a depth of 100nm can be seen in Fig. 13a in the form of a pulse train. Each sensor was initially exposed to hydrogen concentrations ranging from 0.25% to 1% in a series of hydrogen-nitrogen pulses. The sensor demonstrated a 20% decrease in reflected power at 0.25% hydrogen and up to a 27% decrease at 1% hydrogen. This response is approximately three to four times stronger than that of plain film fiber sensors. The measured decrease in reflected power agrees with the predicted changes in the band structure of Pd with the addition of hydrogen. In addition, the overall reflection from the palladium films was almost an order of magnitude lower than what would be expected based on the Fresnel coefficient for the SiO_2-Pd interface. This is attributed to deposition conditions and a poor interface since Pd, like most noble metals, does not adhere well to oxides and may buckle in places as the film stabilizes. SEM imaging shows that the film remains intact and does not lift off or peel back after exposure to concentrations below the beta phase transition, consistent with the reversible microblistering reported by Butler.

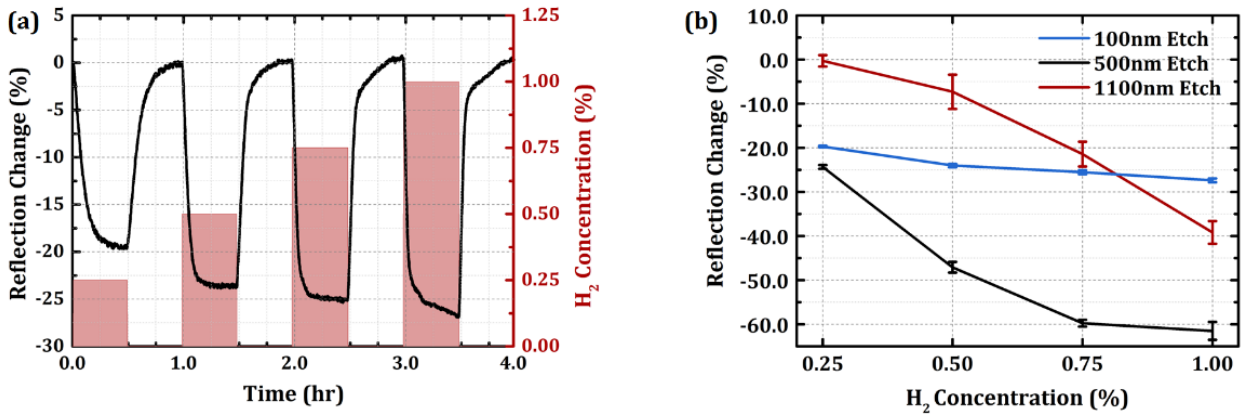

Fig. 13: (a) Pulse test for a 100nm over-etched aperture at 0.25-1% hydrogen in nitrogen. Hydrogen pulses are represented by the shaded regions. (b) Summary of the hydrogen response for 100nm, 500nm, and 1100nm etches into the SiO_2 fiber tip.

The enhancement of the effect in the nano-aperture can be explained by several phenomena. One hypothesis is based on interference and is investigated by studying the etch depth: The C aperture is known to have resonant effects that produce extraordinary transmission, which greatly affects the reflection from the aperture itself. The sub-wavelength C aperture also enables the excitation of surface plasmons that propagate along the fiber-palladium interface which can backscatter due to interface irregularities. Most importantly, however, there is a difference in both the functional dependence of the reflection coefficient with hydrogen and the phase of the fields reflected in the aperture region and those reflected by the surrounding film. Since these fields add coherently, small changes in the aperture properties can affect the reflected intensity greatly.

This is further amplified by the fact that the overall reflection from the film is low. Since the reflection from the aperture is mostly determined by the aperture itself and not the interface, this results in a less disparate field amplitude ratio between the two regions than would normally be expected. In practice, the etched aperture extends beyond the Pd layer into the SiO_2 fiber tip underneath. Since the etched region has a different refractive index and propagation constant than

the surrounding SiO_2, this suggests that we can control the sensitivity by using the etch depth to set the initial phase difference between the two regions without hydrogen.

To investigate this, several apertures were fabricated at a variety of etch depths. Apertures with an etch depth of 100nm, 500nm, and 1100nm were tested. The lowest etch depth, 100nm, was chosen because some over-etching is required to form a well-shaped aperture. Specifically 100nm was chosen because it is a small but accurately measurable depth. A maximum etch depth of 1100nm was chosen because etching is not completely vertical as the etch time into the dielectric increases and the aperture begins to erode. The sloped sidewalls in the SiO_2 and some etching of the top metal layer can be seen in Fig. 12a. These apertures were also exposed to the same 0.25% to 1% pulse train as the previous batch and a summary of the results averaged over 6 pulses can be seen in Fig. 13b. The 100nm etch sensor is the same as shown in Fig. 13a and had a 27% decrease in reflected power at 1% hydrogen. Increasing the etch depth to 500nm improved the response of the sensor significantly, with a decrease of 60% in the reflected power at 1% hydrogen. However, upon further increasing the etch depth to 1100nm, the response was reduced. The overall shape of the response also changed, and the noise in the measurement increased. It can also be seen that the 1100nm etch sensor has almost no response at 0.25% hydrogen.

These results show that the etch depth has an important effect on sensitivity, and that there is an optimal etch depth for detecting low H_2 concentrations. This value depends on both the differential response of the aperture reflection and the effects of over-etching on the loss and mode shape. Since air has a lower index than the SiO_2, the guided portions of the mode will begin to spread away from the over-etched area; therefore, too deep of an etch will prevent the mode from interacting with the aperture. Further, it has been shown that Ga+ implantation in SiO_2 from FIB milling produces an increase in loss [45]. The etch rate of the SiO_2 begins to decrease substantially

as etch time increases, and hence Ga+ build-up increases non-linearly. Scattering and loss from the FIB-damaged portion of the fiber tip will also prevent interaction with the aperture, and will lower the overall reflected power. These factors contribute to the increase in noise and lower measured power for the 1100nm etch.

To further test the 500nm over-etched sensor, a different mass flow controller and diluted 5% hydrogen in nitrogen were used to achieve much smaller concentrations. Using this setup, flow rates ranging from 90 ppm to 660 ppm of hydrogen in nitrogen were attainable. The sensor was exposed to low concentrations using a pulse train analogous to that shown in Fig. 13a while maintaining the same total flow rate as before. A pulse test for these results is shown in Fig. 14a. A summary of both the low and high concentration results is shown together in Fig. 14b along with a plot of the response times in Fig. 14c. A response of 1.7% was measured for 90 ppm hydrogen, and a 10% decrease was measured for 700 ppm hydrogen.

The response time of the sensor decreased from 19 to 4 minutes as the concentration increased. The decrease was very rapid at high concentrations. The recovery time also decreased from 20 minutes at 90ppm to 10 minutes at 2500ppm, after which point it began to rapidly increase, going back up to 14 minutes. The aperture's response is determined primarily by the surface concentration. During exposure, this reaches steady state more quickly because it is close to the source. During recovery, the surface concentration is held higher due to out-diffusion from the film interior, resulting in a longer recovery time. At high concentrations, physical deformations due to the onset of the beta phase are more pronounced and thus the sensor begins to take longer to recover.

The response begins to saturate at higher concentrations; this state most likely is due to reflection solely from the fiber-air interface, due to the microblistering effects. This combined with

the large power changes suggests that in addition to any interference effects, there is also a large mechanical effect not being considered, as will be discussed later.

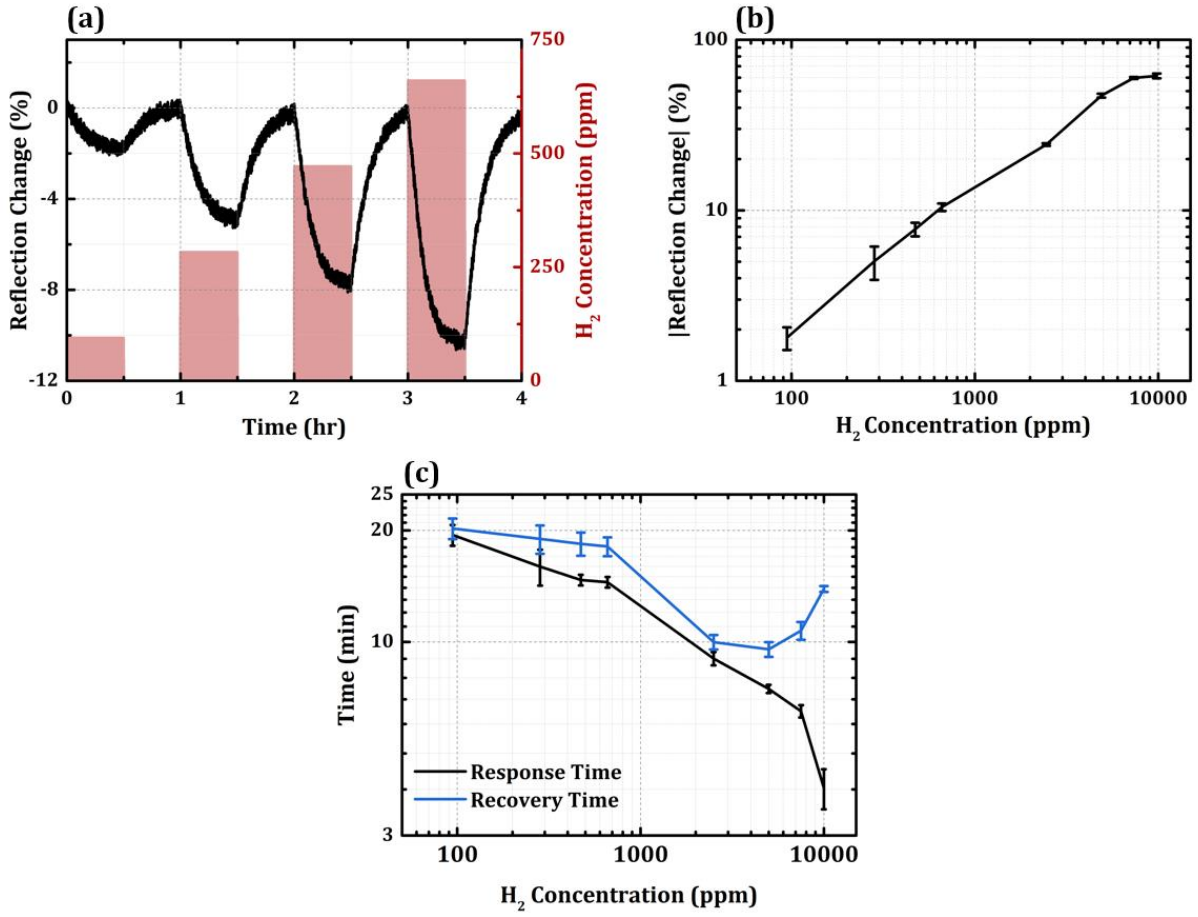

Fig. 14: Pulse test for a 500nm over-etched aperture at 90-660ppm hydrogen in nitrogen. Hydrogen pulses are represented by the shaded regions. (b) The change in measured reflected power spanning 90ppm to 1% hydrogen in nitrogen. (c) The response and recovery times based on a 10-90% metric.

3.3 Minimum Detection Limit

The functional behavior shown in the Fig. 14b log-log plot can be analyzed by considering the mechanics of the sensor. First, hydrogen is adsorbed at the Pd surface. This dissociated hydrogen then diffuses through the lattice forming PdH and changes the refractive index and aperture/film geometry. Hence, the refractive index and geometry are functions of the surface

adsorption. Additionally, the overall reflection itself is a function of the refractive index and geometry. Over a wide range of concentrations, these dynamics are non-linear and complex to model, especially at higher concentrations when buckling and blistering are occurring in the film. At very low concentrations, however, assuming changes to the geometry and optical properties are small, 1st order linear approximations can be made. Therefore the changes in refractive index and geometry are assumed to be linear with PdH content and the change in field reflection linear with refractive index and geometry. At steady-state, the measured response is then proportional to the adsorbed hydrogen in the Pd film, H_{Pd}, which, because of the rough surface, can be modeled as a function of the ambient hydrogen concentration, H, by the Freundlich equation [9], [10]:

$$H_{Pd} = \theta(H) = kH^n, \tag{3.1}$$

where k and n are constants. At steady-state, for low concentrations, the sensor's response is:

$$\frac{\partial r}{\partial H} = \left(\frac{\partial r}{\partial \tilde{n}_{Pd}} \frac{\partial \tilde{n}_{Pd}}{\partial H_{Pd}} + \sum_i \frac{\partial r}{\partial g_i} \frac{\partial g_i}{\partial H_{Pd}} \right) \frac{\partial H_{Pd}}{\partial H} = S \frac{\partial \theta(H)}{\partial H} \tag{3.2}$$

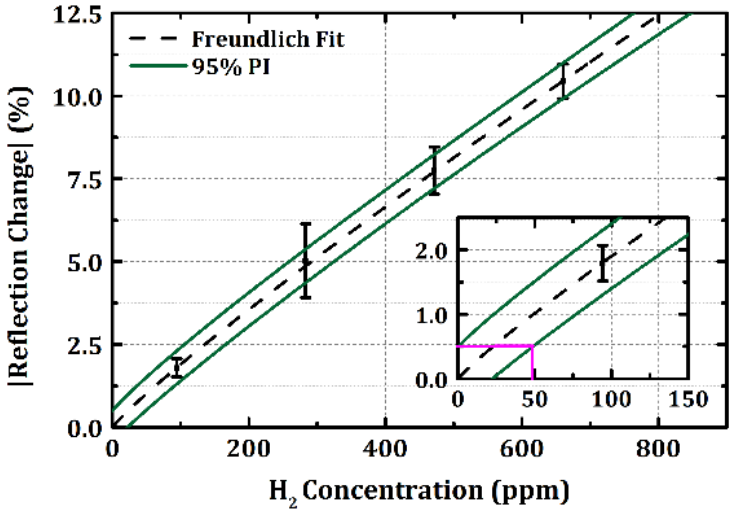

Fig. 15: A fit of the response at low concentrations to the Freundlich equation.

$$S = \left(\frac{\partial r}{\partial \tilde{n}_{Pd}} \frac{\partial \tilde{n}_{Pd}}{\partial H_{Pd}} + \sum_i \frac{\partial r}{\partial g_i} \frac{\partial g_i}{\partial H_{Pd}} \right). \tag{3.3}$$

Here $\tilde{n}_{Pd}$ is the complex refractive index of the Pd film, $\mathbf{g}$ is a vector of parameters describing the aperture geometry, r is the field reflection coefficient, and S is a constant (due to linear approximations) that describes the sensitivity of the reflection to changes in the PdH content of the film. Integrating yields:

$$r(H) = S\theta(H) + r_0 \tag{3.4}$$

Given that $R = |r|^2$:

$$R = |S|^2 \theta^2(H) + \left(S^* r_0 + S r_0^* \right) \theta(H) + R_0, \tag{3.5}$$

where R_0 is the reflected power at 0% hydrogen. Measurements made based on the fractional change in power can be fit by:

$$\begin{aligned} \left| \frac{R(H) - R_0}{R_0} \right| &= \left| \frac{|S|^2 \theta^2(H) + \left(S^* r_0 + S r_0^* \right) \theta(H)}{R_0} \right| \\ &= \left| \frac{k^2 |S|^2 H^{2n} + k \left(S^* r_0 + S r_0^* \right) H^n}{R_0} \right|. \end{aligned} \tag{3.6}$$

For the concentrations below 1000 ppm the data in Fig. 14b was fit to Eq. (3.6). The fit results are shown in Fig. 15. Using this fit, a value of n = 0.45 ± 0.1 was found. This is in agreement with Sievert's law for diatomic gases which predicts n = 0.5. Note that the hydrogen concentration in the experiment is proportional to the partial pressure of the gas. Additionally, by using the 95% prediction interval of the fit, the minimum detection limit (MDL) of the sensor can be extrapolated

using the method of Hubaux and Vos [47]. Through this method, the MDL is defined as the smallest concentration with a prediction interval that does not overlap the prediction interval for 0% based on the fit. This was found to be approximately 50 ppm of hydrogen.

3.4 Simulation Methods & Results

As mentioned, the change in reflection would be expected to be dominated by the plain film surrounding the aperture. However, experimental results showed that the aperture clearly plays some kind of role in enhancing the sensitivity of the reflected power to hydrogen. To ensure that previous simulations based on separating the aperture and the plain film were accurate, as well as to test some potential structural differences, such as an angled facet, full scale FEM simulations were done using the Cisco Arcetri computing cluster in collaboration with Mingfeng Xue from Professor Jin's group at the University of Illinois. Using the much larger memory and computing capacity, as well as a domain decomposition technique developed by Prof. Jin's group, it was possible to simulate an entire cross section of the fiber, meshed to include the aperture and enough longitudinal distance to accurately calculate reflection and transmission. The method, a dual-primal finite element tearing and interconnecting (FETI-DP) method, employs second order transmission conditions on subdomain interfaces (SOTC-TE). More information about the simulation method can be found in [48]. The simulation domain can be seen in Fig. 16. The PML truncates the cladding layer at a radius well outside the mode diameter which is mostly confined to the core. Previous simulations were only able to simulate a small region around the aperture, much less the entire core and part of the cladding.

Initial simulations were done to verify the accuracy of the method by computing field profiles and comparing them to those obtained through prior FDTD and FEM simulations of just

the aperture. These results are shown in Fig. 17 along with field profiles for the entire domain a distance 1.5μm above the aperture.

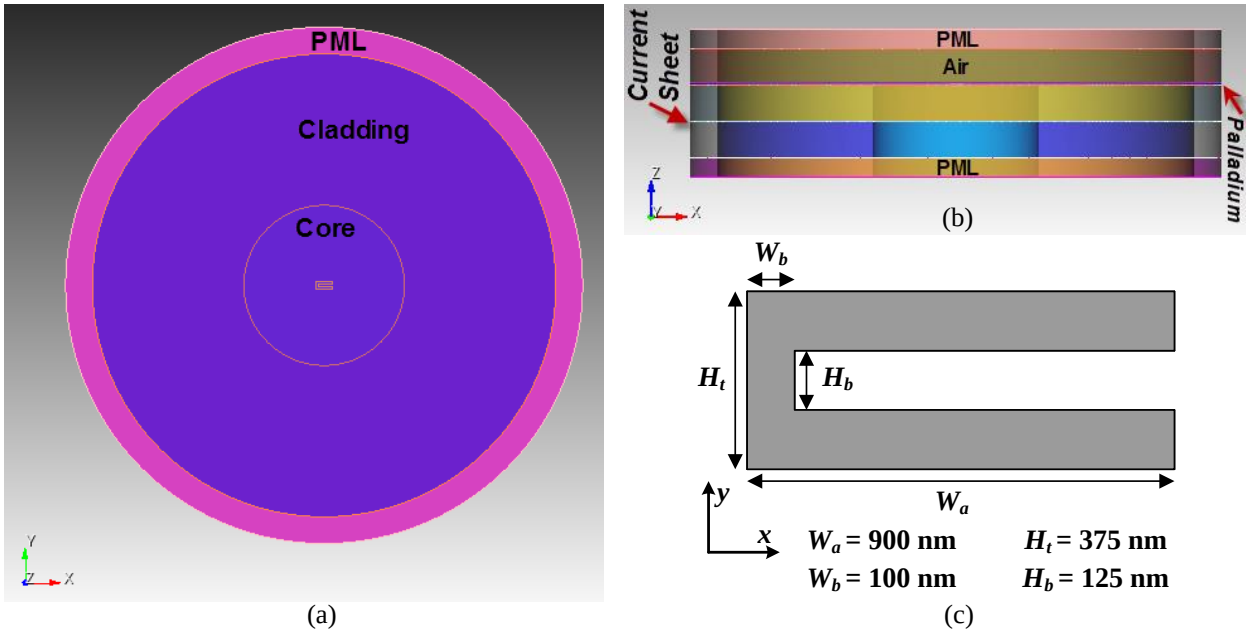

Fig. 16: Simulation domain for the FDTD domain decomposition method simulations on the Cisco Arcetri cluster. (a) Lateral view (b) longitudinal view, a current sheet is used to excite the incident plane wave (c) aperture dimensions. Figure credited to Mingfeng Xue.

The next step was to try to simulate the experimental results by adjusting the etch depth. Several simulations were done at various etch depths. Some of the results can be seen in Fig. 18. The simulations showed that there was a correlation between reflection and the etch depth. However, given the known changes in refractive index, the calculated change in reflection with hydrogen (Fig. 19) was about two orders of magnitude lower than experimentally seen. As expected, the reflection change is not solely due to interference effects; the aperture is too small for that to be the case.

The possibility of a cleaved facet reducing overall reflectivity and thus emphasizing the aperture was also investigated for a variety of cleave angles. The reflectivity drops as the cleave angle is increased, which is also expected as more of the reflected light is not guided back down

the fiber. However, even for large cleave angles of 2.0° or higher, the change in reflection with hydrogen was off by an order of magnitude or more and the overall reflectivity was still higher than experimentally recorded.

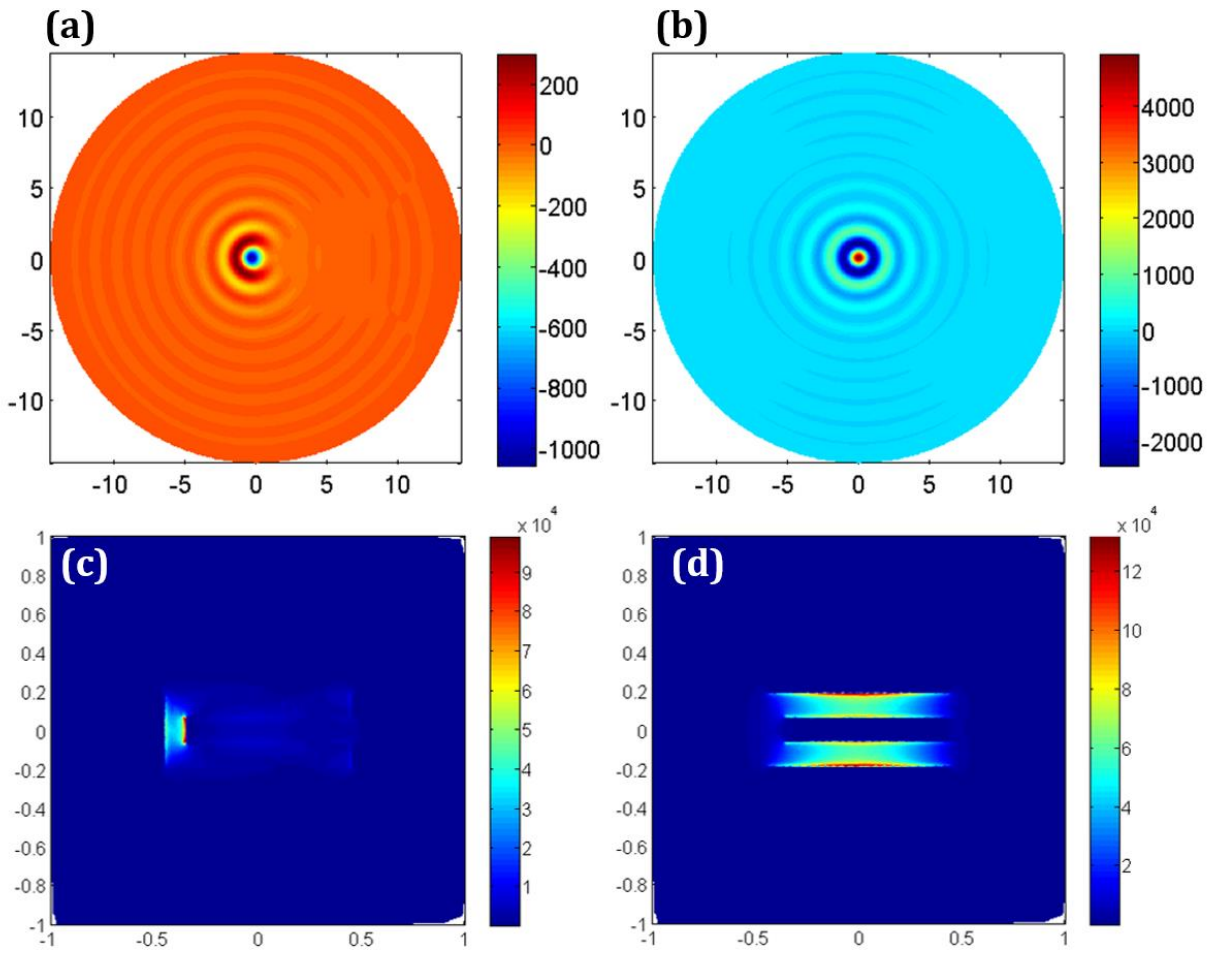

Fig. 17: (a) Field slice 1.5 µm above aperture for E_x polarization. (b) Field slice 1.5 µm above aperture for E_y polarization. (c) Computed aperture field profile for incident E_x polarization. (d) Computed aperture field profile for incident E_y polarization. Figure credited to Mingfeng Xue. Reprinted with permission.

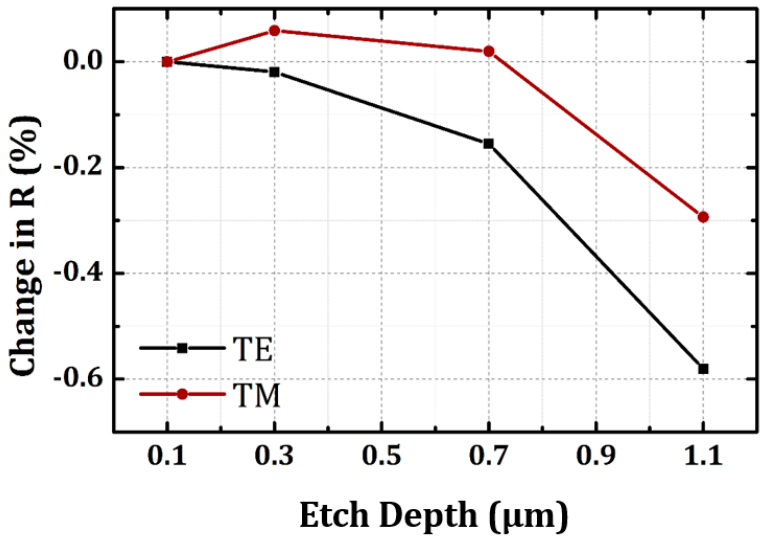

Fig. 18: Simulated change in reflection (compared to a 100 nm etch) as a function of over-etch depth.

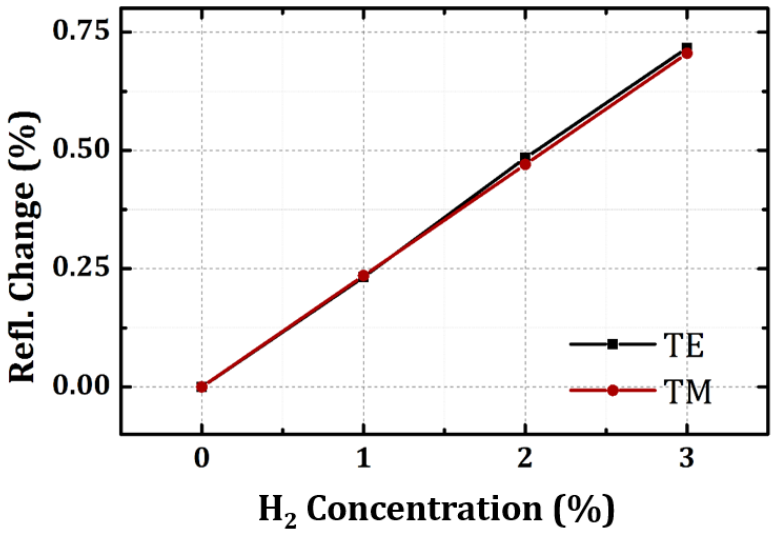

Fig. 19: Change in reflection as a function of hydrogen concentration for a 100 nm over-etched aperture.

3.5 Discussion

Even though the refractive index of PdH is not well known, the change required to produce such large reflection changes is unreasonable. Combined with the simulations done on the Cisco Arcetri cluster, this leaves structural changes or deformities such as buckling, delaminating, expansion, and roughness as the most likely candidates to the explain the discrepancy. These effects are harder to simulate and require knowing more about the mechanical behavior of the film. However, it is possible to rule out simple expansion or alteration of the aperture dimensions as the reason for the large reflection change as this does not solve the problem of the large amount of power reflected from the surrounding film. Additional simulations showed the sensitivities to the aperture dimensions were rather small, on the order of 0.1 %/nm change in transmission and 0.001 %/nm in reflection. The very low sensitivity in reflection is expected due to the small aperture. It is also possible the FIB process affects the adhesion of the surrounding film, and this is why the presence of an aperture consistently improves the performance of the sensor.

The difficulties arising from modeling the aperture device, as well as the large improvements in performance these effects cause, are the catalyst for the remainder of the work presented and the new sensor design proposed in the last chapter. Despite the inability to accurately model and predict the behavior of the sensor, this design still showed good performance and repeatability. The 500nm etch depth sensor showed a large repeatable response for hydrogen concentrations ranging from 90 ppm to 1% in nitrogen. A maximum power decrease of 60% at 1% hydrogen was recorded, while a 1.7% power decrease was seen at 90 ppm hydrogen. By constructing 95% prediction intervals for the response at low concentration, a minimum detection limit of 50 ppm was predicted. These results make this design a very promising sensor. An updated summary of the nano-aperture results in shown in Table II.

For all of the nano-aperture sensors presented and discussed in Chapters 2 and 3, the limiting factor contributing to pulse-to-pulse variation in response appears to be a systemic result of the behavior of the Pd film upon hydrogen absorption and not the measurement setup. For practical applications, simple power based measurements are subject to noise through alterations in the optical path, such as fiber bending and temperature fluctuations. In the case of fiber bending, the loss can be rather large for bending radii of less than 10 cm for typical single mode fiber - increasing by roughly a factor of 100 every 1 cm. For larger radii, the loss is negligible; however, bending and slight alterations to the fiber can still result in random polarization changes at the facet. These can either be countered through self-referencing techniques such as the PDL measurements in Chapter 2, or by ensuring the fiber is well protected and by implementing redundancy. In the case of polarization uncertainty, polarization-maintaining fiber or a scrambler system similar to the way the PDL was measured could be used to ensure the same polarization state is always measured. Although not tabulated, the experimental sensitivity to fabrication was relatively small, with multiple sensors showing a deviation in response of less than 5%.

Table II
Nano-aperture Sensor Performance

Mode	Sensor	ΔP at 0.25% H_2	ΔP at 1% H_2	Sensitivity: $\Delta P/\Delta H_2$ for H_2 between 0.5 and 1%
Transmission	C Aperture, TE (Max)	8.5%	15.3%	5.6
	C Aperture, TM (Min)	6.9%	12.0%	3.8
	Circle	2.9%	4.7%	1.9
	Plain Film	0.4%	1.6%	1.5
	PDL	0.07dB	0.14dB	0.09 dB per $\%H_2$
Reflection	C Aperture	19.7%	27.4%	6.8
	Circle	9.3%	28.9%	18.7
	Plain Film	1.5%	5.7%	4.0

CHAPTER 4

MECHANICAL CONSIDERATIONS

4.1 Hydrogen Induced Lattice Expansion

It is well known that palladium absorbs and expands with hydrogen through a process called hydrogen induced lattice expansion (HILE). When gaseous H_2 molecules come in contact with Pd, they disassociate into single atoms and diffuse into the face-centered cubic (FCC) Pd lattice. The H atoms bond to the interstitial sites and form PdH, which starts in the α-phase, causing small changes in the lattice constant. Once the H_2 concentration reaches the lower critical limit α_{max}, regions containing PdH begin to swell forming β regions where the lattice constant can increase up to 3.5% [7] since Pd can absorb up to 900 times its volume in hydrogen [2]. This expansion is highly isotropic due the symmetry of available bonding sites for hydrogen within the FCC lattice structure of Pd [7]. When the Pd is weakly bonded to the substrate, such as with a quartz substrate, the isotropic expansion can lead to micro-blistering, micro-cracking, and buckling of the Pd film [22], [23]. As the adhesion strength increases, this can lead to anisotropy in the expansion (Fig. 20). Fortunately, these changes and also lattice expansion are reversible, at least for some time at low concentrations [22], [23]. However, at higher H_2 concentrations, the transition to the β phase can induce plastic deformations, resulting in permanent structural changes. Evidence of the β phase can be seen at about 1.5% H_2 for our films. In practice, a high volume of repeated exposures or even a single prolonged exposure at a high enough concentration can lead to film embrittlement or delamination [11], [49]. In general, the sensitivity, response time, and recovery

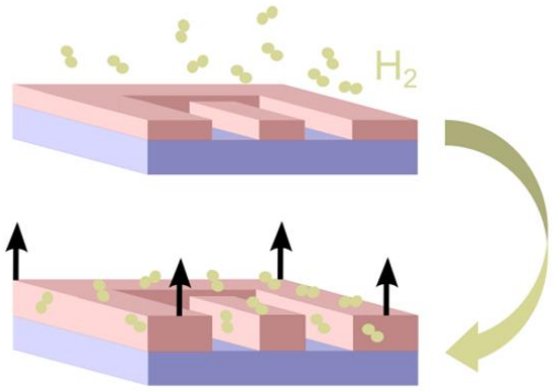

Fig. 20: Illustration of hydrogen induced lattice expansion

time of a Pd sensor that undergoes structural changes will depend on the surface adhesion, substrate material, film thickness, method of deposition, and the geometry of the sensor.

These effects are the most likely reason for the extremely high power changes seen in the nano-aperture sensor and are integral to the design of optomechanical sensors. In order to simulate these kinds of effects, accurate data about the rates and dynamics of HILE on a thin film scale are needed. A sensitive technique is required to measure the nanoscale changes during H_2 exposure. To accomplish this, an imaging technique known as diffraction phase microscopy was employed to image, in-situ, the nanometer scale expansion and contraction of Pd micropillars. This work was done in collaboration with Christopher Edwards and Professor Gabriel Popescu at the University of Illinois and published [50]. Epi-illumination diffraction phase microscopy (epi-DPM) is a proven technique with sub-nanometer height measurement accuracy; it has been used to monitor wet etching of semiconductors [51], photochemical etching [51], [52], and material deformation, as well as to detect defects in patterned semiconductor wafers [53].

Figure 21 shows the time dependent change in height of a 250nm thick Pd micropillar on quartz measured using diffraction phase microscopy during and after exposure to various hydrogen concentrations. Beyond the α-β phase transition, more drastic changes occur in the Pd lattice,

which result in permanent damage through plastic deformation as seen in Fig. 22. However, even though the structure of the film is irreversibly altered, the hydrogen can still completely diffuse out. Prolonged exposure to high concentrations of hydrogen in metals can also lead to further degradation as the repeated deformations result in embrittlement or delamination of films [11], [49].

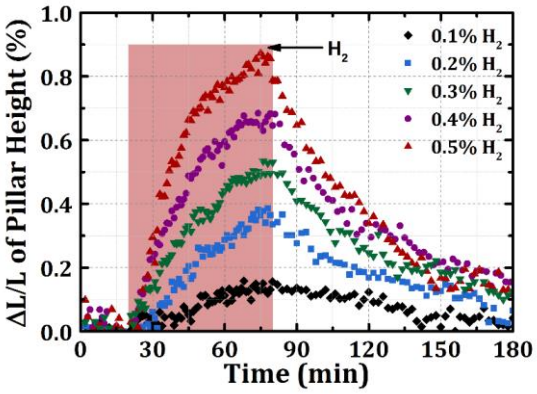

Fig. 21: Measured change in the height of a 250nm thick Pd micropillar on quartz using diffraction phase microscopy. Figure adapted from [39].

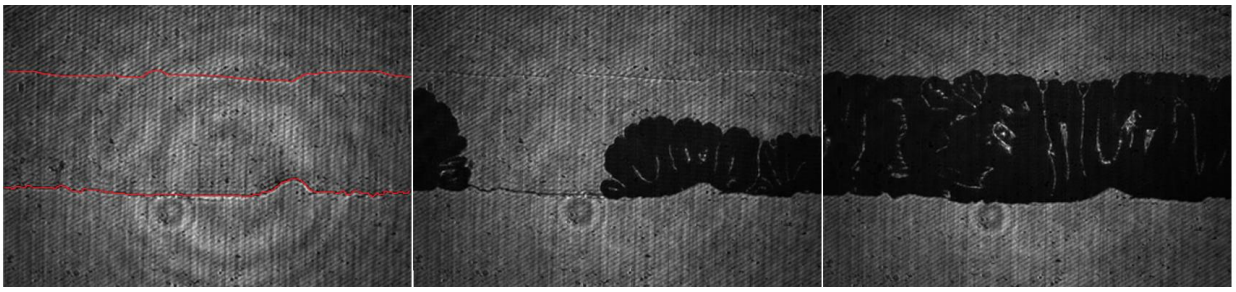

Fig. 22: Time lapse from left to right of a Pd ridge (outlined in red) exposed to 4% hydrogen in nitrogen showing buckling, delamination, and plastic deformation.

4.2 Measurement of the Axial Expansion of Palladium Microdisks

The experimental setup is shown in Fig. 23; the optics and microscope were assembled and calibrated by Chris Edwards and other members of the Quantitative Light Imaging (QLI) and Photonic Systems Laboratory (PSL) research groups. The imaging system uses a 532nm frequency-doubled Nd:YAG laser, a diffraction grating, 4f lens system, spatial filter, and CCD camera to create a compact Mach-Zender interferometer. The interferogram is imaged by the CCD and is processed using a Hilbert transform and bandpass filtering the measured signal. This allows reconstruction of the topography with sub-nanometer accuracy because it is a phase measurement, rather than amplitude [54]. Phase shifts exist in the reflected light image either because of a spatially dependent complex reflection coefficient or because of height differences. The point-to-point (spatial) noise of the system was measured at 0.55nm and frame-to-frame (temporal) noise was measured at 0.43nm [51], [52]. These values can be further reduced through spatial or temporal averaging. Since this is an optical and non-destructive technique that requires no staining or coating, it allows for in-situ monitoring of surface and material dynamics at the nano-scale. Additional information about the technique can be found in [51], [54]–[56].

A custom designed aluminum flow chamber was fabricated to hold the samples in a controlled atmosphere of hydrogen and nitrogen. A glass slide was used as a transparent imaging window to view the sample, and was mounted on top of the chamber at a slight angle. This was required because it was found that the imaging technique was sensitive to multiple reflections within the slide when it was mounted normal to optical path. The slight angle prevented the multiple reflections from being imaged. The nitrogen and hydrogen flow rates were controlled with LabVIEW through mass flow controllers (MFC) and a data acquisition (DAQ) card. Since low flow rates were being used, solenoid valves were also mounted close to the chamber to quickly

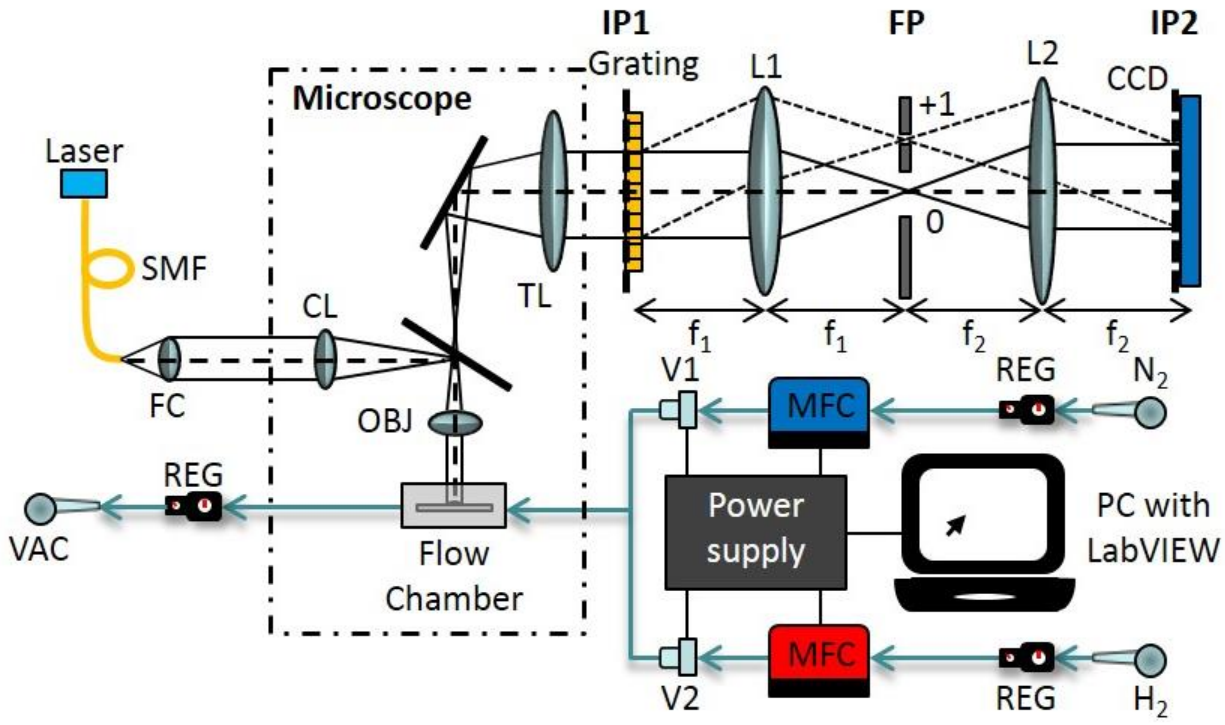

Fig. 23: Experimental setup. Epi-DPM was used to monitor height changes to the Pd microdisk sample housed in a flow chamber with H2 and N2 rates set via LabVIEW. Abbreviations: SMF, single mode fiber; FC, fiber collimator; CL, collector lens; OBJ, objective; TL, tube lens; L1/L2, lenses; V1/V2, valves; MFC, mass flow controller; REG, regulator; VAC, vacuum line. Figure from [50].

turn on and off the flow of gas. This prevented the gas left in the line from slowly diffusing into the chamber, even after the MFC had been turned off, distorting the H_2:N_2 pulse shape.

Pd microdisks on quartz (SiO_2) substrates were fabricated using e-beam evaporation and a shadow mask. SiO_2 is of particular interest due to its extensive use in fiber-based H_2 sensing applications [20], [25]. Poor substrate adhesion prohibited the use of standard lithography and lift-off techniques. The shadow mask has 180 µm diameter holes with a 350 µm pitch and was placed very close to the substrate. As shown in Fig. 24(a), a 260 nm Pd layer was deposited, the shadow mask was removed, and 40 nm of Pd was blanket deposited. The blanket deposition of this optically thick Pd layer ensures that both the microdisks and the background have the same complex refractive index, which allows changes in the microdisk height to be decoupled from

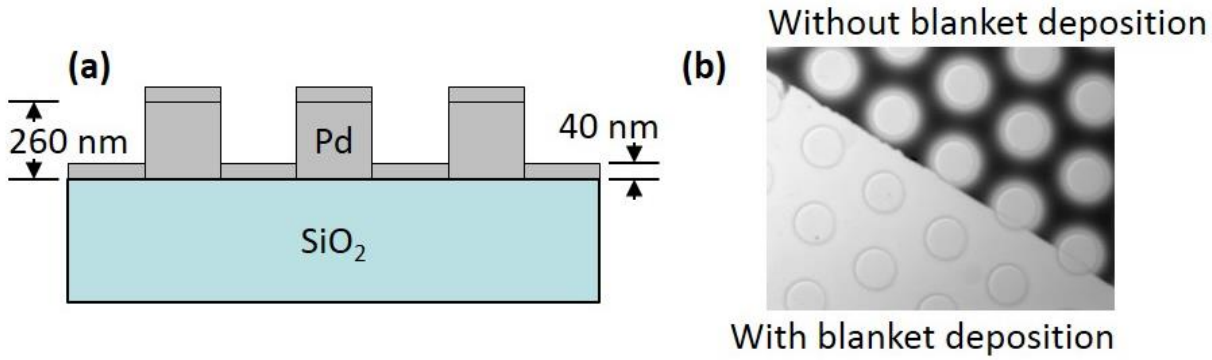

Fig. 24: Pd microdisk sample. (a) Schematic of 260 nm tall Pd microdisks on a quartz substrate and the 40 nm blanket deposition. (b) Bright-field image shows an edge of the blanket. Figure from [50].

changes in the reflection coefficient's phase due to changes in the complex refractive index of the Pd layer. Variable angle spectroscopic ellipsometry (VASE) data yielded a complex refractive index of 1.56 +3.64j for our Pd structures. Furthermore, the shadow mask approach creates smoother edges, which prevents phase unwrapping errors in our measurements [26]. Note that the blanket deposition was also masked to verify the thicknesses of the blanket layer. See Fig. 24(b).

Figure 25(a) shows the surface topography of a Pd microdisk and its initial dimensions. The initial height relative to the background before H_2 exposure was 264.4 nm and the full width at half maximum was 181 μm. The height was measured by averaging over a circular region containing the top flat portion of the microdisk. Figure 25(b) shows the temporal stability of the system during an N_2 calibration run. The temporal noise for the mean microdisk height in the presence of 300 standard cubic centimeters per minute (sccm) of N_2 flow was 0.16 nm.

Figure 25(c) shows the change in microdisk height versus time for a 0.4% H_2 pulse. An initial 30 min baseline was acquired using pure N_2 at 300 sccm. H_2 was then switched on and the flow rates were adjusted to maintain the 300 sccm total rate. The H_2 ran for 90 min and was shut off at the

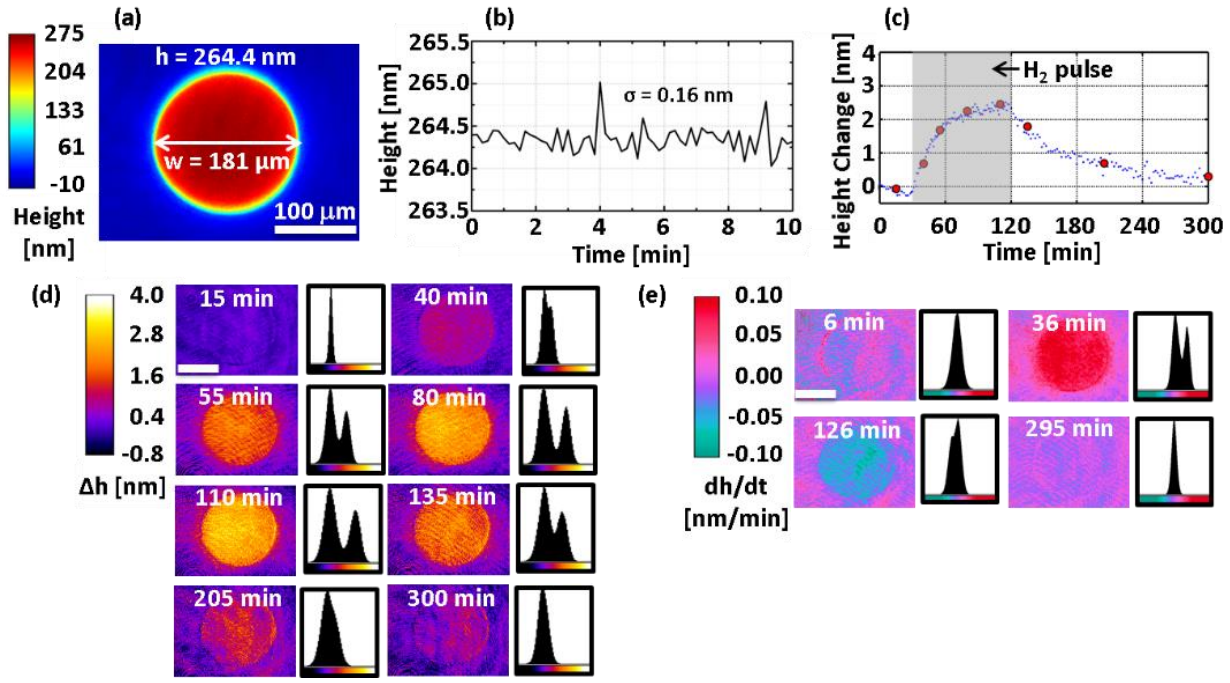

Fig. 25: Differential height measurements during H2 exposure. (a) Height map of a Pd microdisk before H2 exposure using epi-DPM. (b) Stability of height measurement during N2 baseline run. (c) Average height change of the Pd microdisk. H2 was turned on to 0.4% at 30 min and turned off at 120 min. (d) Selected frames and their histograms for the local height change at various times indicated in (c). (e) Instantaneous expansion rate before exposure, during expansion, during recovery, and after recovery. All scale bars are 100 µm. Figure from [50].

120 min mark. The chamber was then purged with pure N_2 at 300 sccm for 3 hours. Frames were acquired every 6 s during pure N_2 exposure and every 3 s during the H_2 pulse. During the experiment, the sample drifted very slightly, on the order of 100 nm in the sample plane or ½ of a CCD camera pixel at the image plane. To obtain the most accurate instantaneous height change images, this in-plane motion was corrected by registering the epi-DPM height images with sub-pixel resolution as follows. First, each frame of the 30 min N_2 baseline was registered by performing a cross-correlation with the very first frame, finding the position of maximal cross-correlation r_{max} with sub-pixel precision by fitting the cross-correlation image with a 2^{nd} order polynomial in the neighborhood of its largest value, and then linearly interpolating the epi-DPM height image onto a grid that is shifted by $-r_{max}$. After registration, these baseline epi-DPM images

were averaged to reduce noise and thereby produce the most accurate baseline image against which to compute the instantaneous height change. Next, each image of the entire pulse test was registered to this baseline image and the instantaneous height change images were computed by subtraction. To reduce temporal noise, these instantaneous height change images were then averaged for 1 min, i.e. 10 frames during the N_2 exposures and 20 frames during the H_2 pulse. The axial expansion of the microdisk is thereby measurable in a spatially and temporally resolved manner with very high accuracy.

Figure 25(d) shows instantaneous height change images of the microdisk during the pulse test and their associated histograms, where the frames were selected from Fig. 25(c) to evenly sample the axial expansion process. The expansion can be clearly observed in Fig. 25(d) as the initial histogram peak with zero height splits into two peaks during H_2 exposure, one remaining at a height of zero and the other revealing the expansion, and subsequently the peaks merge back into a single one upon purging the chamber with N_2. Furthermore, small deformations, or local heterogeneities, can be observed during parts of the expansion and recovery process. These are observed in the histogram by considering the width of the peaks, but are more easily identifiable in the instantaneous height change images.

Figure 25(e) shows a select subset of the spatially and temporally resolved instantaneous rate of axial expansion at four key moments: before exposure (6 min), at the beginning of expansion (36 min), at the beginning of recovery (126 min), and far into recovery (295 min). For best accuracy, the instantaneous axial expansion rate images were computed pixel by pixel by performing a simple linear regression of the height change versus time for a 10 min window centered at the times specified in Fig. 25(e). From these images, we see a negligible expansion rate before exposure and far into recovery and about a 0.1 nm/min expansion rate at the onset of H_2

exposure and a 0.1 nm/min contraction rate as the H_2 is turned off. Further, the expansion and contraction rates are relatively uniform across the Pd microdisk.

The standard pulse test was repeated for other H_2 concentrations to be able to quantify the dependency of axial expansion on concentration. Figure 26(a) shows the height changes for the various pulse tests. The response times were all approximately 30 min. After recovering in N_2, the height returned to its initial value to within the noise of the system. The recovery time was approximately 2-3 hours for all cases. Figure 26(b) shows the change in height in percent, Δh, for each pulse test as a function of the H_2 concentration in percent, c. For ideal films at constant temperature, the axial expansion process is limited by surface adsorption which is governed by either the Langmuir or Freundlich isotherms [8]. Given the low adsorbate concentrations used in this study, the Freundlich equation is more appropriate. Assuming that the axial expansion is linear with PdH content, this power law fit can be applied to the percent height change data [31]. This provides a model for the microdisk height change $\Delta h(c) = k \cdot c^n$. Fitting the data to a power law gives $k = 1.28 \pm 0.06$ and $n = 0.51 \pm 0.04$, which agrees well with Sievert's law ($n = 0.5$) and the anticipated square root dependence for diatomic gas [57].

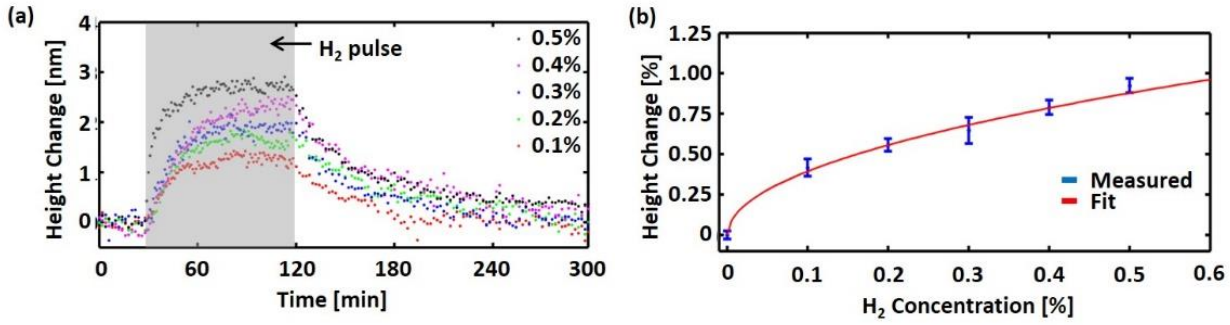

Fig. 26: H2 induced height changes of a Pd microdisk. (a) Measured height change for different H2 concentration pulse tests. (b) Percent change in height, Δh, versus percent H2 concentration, c, with Freundlich fit: $\Delta h(c) = k.c^n$, where k = 1.28±0.06 and n = 0.51±0.04. Figure adapted from [50].

4.3 Adhesion Layer Effects

It is well known that noble metals such as Pd have poor adhesion to oxides such as SiO_2. This was a notable problem when it came to fabricating both the on fiber devices, and planar samples for ellipsometry and the HILE measurements. They required both careful handling and limited exposure to high concentrations of hydrogen or air to prevent film deformation that would result in delamination. Experimental testing of the fiber devices often involved losing many samples to mechanical abrasion when mounting, which resulted in the design of a packaging method to prevent the tip from being brought into contact with anything.

However, that poor adhesion is also most likely what made them so sensitive when measuring the reflected power. Several different adhesion layers were tested. Titanium is a popular adhesion layer, and tests showed that samples with a thin Ti adhesion layer of a couple nanometers had remarkably improved durability. This did not result in much degradation of the sensitivity in transmission – the devices still showed the same overall response magnitude, but it did cause an almost 10x deterioration in response time.

Since such a long response time does not make a useful sensor, other metals including Ni and Cr were tested. The adhesion produced by a Cr layer was not as good as the Ti layer, but still provided an improvement. However, the Cr also worsened the response time significantly, by about a factor of 5x. The Ni samples did not show much change in response time, making for good sensors, but the adhesion was not as strong as the Cr and Ti samples. These conclusions are summarized in Table III. Currently a Cr/Ni stack adhesion layer is being employed when adhesion is required.

Table III
Nano-aperture Sensor Performance

Adhesion Layer	Response Time	Adhesion Strength
Titanum (Pd/Ti)	Extremely Poor	Excellent
Chromium (Pd/Cr)	Poor	Good
Nickel (Pd/Ni)	Good	Poor
Pd/Ni/Cr stack	Good	Good

4.4 Discussion

A more detailed analysis of the expansion of the microdisk requires us to consider adhesion effects and to allow the expansion coefficient to vary as a function of hydrogen concentration. In addition to the axial expansion due to the hydrogen induced isotropic expansion, there is a further enhancement to the axial expansion when the Pd film is adhered to the substrate. To understand this, we begin by assuming that the Pd is not adhered to the substrate and can undergo isotropic expansion and that the hydride concentration is uniform. The induced free expansion in the disk in Fig. 25 would then be given by

$$\frac{\Delta h_1}{h_0} = \alpha\left(H - H_0\right) \tag{4.1}$$

and

$$\frac{\Delta w_1}{w_0} = \alpha\left(H - H_0\right), \tag{4.2}$$

where h and w are the height and width of the microdisk respectively, α is the expansion coefficient at a given concentration, H is the atmospheric hydrogen concentration, and the "zero" subscripts denote initial conditions in the absence of hydrogen. However, when the Pd is constrained at the

surface due to adhesion, the inability to expand in the lateral dimension can be seen as a compressive stress. We approximate the hydrogen expansion effect and the compressive stress from the adhesion effect as independent. Because the strains are related by Poisson's ratio, ν, the width can according to:

$$\frac{\Delta w_2}{w_0} \simeq -\nu \frac{\Delta h_2}{h_0 + \Delta h_1} \tag{4.3}$$

with

$$\Delta w_2 = -\Delta w_1 . \tag{4.4}$$

The $h_0 + \Delta h$ term appears in the denominator because the initial height of the unconstrained expanded disk is that given by the isotropic expansion following Eq. (4.1). Combining Eqs. (4.1) through (4.3) gives the following relationship for the measured height change:

$$\Delta h = \Delta h_1 + \Delta h_2$$

$$\Delta h = \alpha \left(1 + \nu^{-1}\right)\left(H - H_0\right) h_0 + \frac{\alpha^2 \left(H - H_0\right)^2}{\nu}$$

$$\Delta h \simeq \alpha \left(1 + \nu^{-1}\right)\left(H - H_0\right) h_0 , \tag{4.5}$$

where the quadratic portion is negligible. Assuming that the reference condition is 0% hydrogen, Eq. (4.5) becomes

$$\Delta h \simeq \alpha H \left(1 + \nu^{-1}\right) h_0 , \tag{4.6}$$

which is linear with the strain represented by the product term αH. To verify this assumption a 3D FEM simulation of the Pd disk was carried out in COMSOL using the thermal module, which is well suited for material expansion. The simulation results for multiple hydrogen concentrations are shown in Fig. 27a as a function of the expansion coefficient, and are linear as expected based on the thermal model used. Furthermore, the height change vs. the strain is plotted in Fig. 27b for

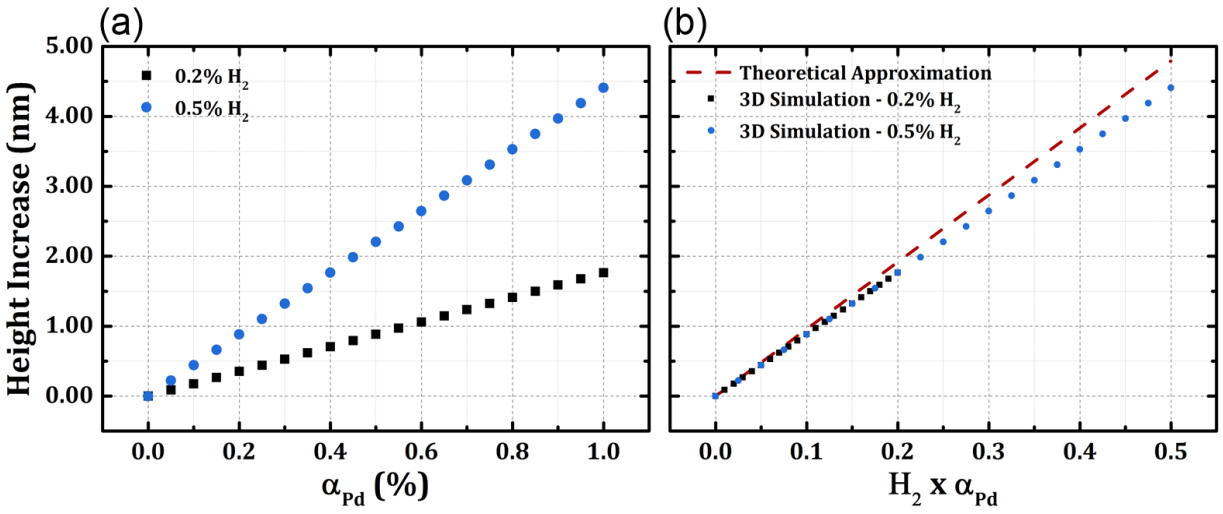

Fig. 27: 3D simulation results for the Pd disk. (a) Height increase as a function of expansion coefficient. (b) Height increase as a function of the strain, shown as the product of the expansion coefficient and hydrogen content.

two different simulations, which serves to verify things are working properly. Also shown in this plot is the theoretically calculated height change as a function of the strain from Eq. (4.6) which shows good agreement with the more time-consuming simulations. Literature values for the Young's modulus of E = 73 GPa and for Poisson's ratio $\nu = 0.44$ were used for the Pd layer [58]. The substrate was treated as fixed. The slight discrepancy between the theoretical and the simulated values is attributable to the fact that Eq. (4.6) assumes the disk is uniformly constrained laterally, which it is not. While the simulations can be used directly to relate the height change to the expansion coefficient, it is sometimes useful to have a heuristic relationship. Noting that the simulation results are also very linear, the slopes of the two data sets can be compared to give a correction factor of 0.92: in other words

$$\Delta h_{corrected} \simeq 0.92 h_0 \left(1+\nu^{-1}\right)\varepsilon\,, \qquad (4.7)$$

where

$$\varepsilon = \alpha H\,. \qquad (4.8)$$

This correction factor is dependent on the disk geometry. Using these results, the measured height changes and their corresponding hydrogen concentrations, the expansion coefficient can be extracted as a function of hydrogen. Furthermore, according to Eq. (4.7) if the change in height with hydrogen is linear then the strain is also linear with H. Allowing α to have a functional dependence on H and differentiating Eq. (4.8) yields

$$\frac{\partial \varepsilon}{\partial H} = \frac{\partial \alpha}{\partial H} H + \alpha \equiv const., \tag{4.9}$$

which has solutions of the form

$$\alpha(H) = \alpha_{\max} + \frac{\zeta_0}{H}. \tag{4.10}$$

The extracted expansion coefficients and a fit according to Eq. (4.10) are shown in Fig. 28. The fit was performed for the linear portion of the height vs. hydrogen data. The cut-off of 0.3% for the fit is somewhat arbitrary but agrees with other collected data, as will be shown later in Chapter 5. For lower concentrations tabulated data can be used as the expansion appears increasingly non-linear with hydrogen content. The $\alpha_{\max}$ term is related to the expansion for an ideal isotropic Pd film and the coefficient denoted by ζ_0 is a function of geometry and constraints. The results of the fit yield values for $\alpha_{\max}$ and ζ_0 of 0.45 ± 0.01 and 0.08 ± 0.01 respectively. It is very important to note that these expansion coefficients are given as a function of the atmospheric hydrogen concentration, not the concentration of PdH_x. While these results are strictly empirical compared to Eq. (3.1) and Fig. 26, they are potentially very useful for device design.

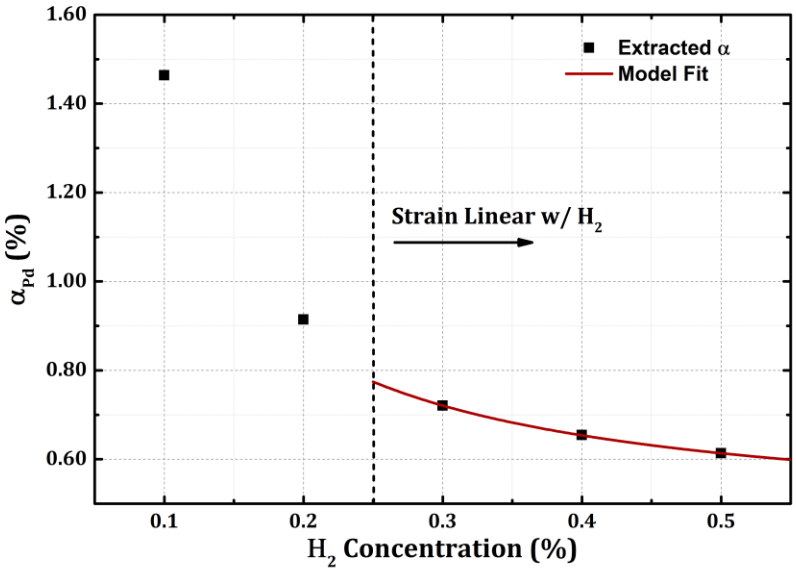

Fig. 28: Expansion coefficients extracted from DPM data using Eq. (4.7) and fit to a strain model that is linear with H_2 concentration according to Eq. (4.10).

CHAPTER 5
OPTOMECHANICAL SENSORS

A significant amount of effort was spent in trying to accurately model the devices presented in Chapters 2 and 3. However it was eventually realized that due to incomplete knowledge of the dynamics of the film, specifically accurate refractive index data for PdH and little to no inclusion of mechanical effects such as HILE in the simulations, that these simulations would not match the experimental data. Research into the complex refractive index of the film has been an ongoing effort, but is complicated by the fact that it depends so strongly on deposition conditions and varies from film to film. The research done on the palladium expansion, presented in Chapter 4, was done in part so that the mechanical dynamics of the sensors could be quantified and simulated.

The data obtained from those measurements, combined with the impressive sensitivity demonstrated by the reflective sensor, almost certainly attributable to lattice expansion and poor adhesion, led to the optomechanical sensor designs presented here. The proposed designs are based on a cantilever structure. By coating the cantilever with Pd, not only will the reflectivity change, but stresses induced by HILE will cause the cantilever to flex. Such designs have been used before to create capacitive sensors [59]–[61]. Incorporating this mechanical action directly into the sensor design allows for much more accurate device simulation, and the ability to predict sensor behavior based on past measurements. This work is mainly concerned with establishing and modeling the dynamics of the cantilever from basic principles and past measurements using the DPM characterization technique, but a more compact sensor could be made by forming a cavity using the cantilever as a mirror. There is also the potential of integrating resonant optical structures onto the cantilever mirror, further increasing the sensitivity.

5.1 Sensing Method

Depending on the form of the probe measurement, the sensing mechanism is based on the flexure and/or reflectivity change of the cantilever. Upon exposure to hydrogen, the refractive index of the palladium layer will change and the layer will expand. The expansion of the Pd layer will cause stress that will flex the membrane. When incorporated into a cavity this would effectively change the length of the cavity. Furthermore, the refractive index and surface angle of the membrane will also change, changing the reflectivity and coupling efficiency of the top mirror. For the latter, simulations and measurements show deflections large enough to scatter the light out of the acceptance angle of single mode fiber are easily obtainable. Such a device would essentially represent a controlled and improved version of the reflective nano-aperture sensor.

Several different membrane geometries can be considered. The two basic structures are a suspended membrane, either rectangular or circular, anchored on at least two sides (Fig. 29a), or a cantilever structure anchored only at one end (Fig 29b). An extension of the latter is the butterfly structure shown in Fig. 29c with a thin anchor at the center, essentially two cantilevers back to back. One final consideration is where to place the Pd layer, and whether or not it should coat the entire cantilever, specifically in relation to the anchor point. Simulations showed that this effect was not large, but more overlap with the anchor point slightly reduced the total flexion of the cantilever or membrane.

Each structure has advantages and disadvantages which depend on the design constraints. The cantilever structure would allow for larger deflections, which may or may not be desirable, but would be mechanically weaker than the suspended membrane. The butterfly structure shares the same properties as the cantilever while keeping the design more symmetric. Depending on the width and placement of the anchor with relation to the mode, however, it could be weaker or less

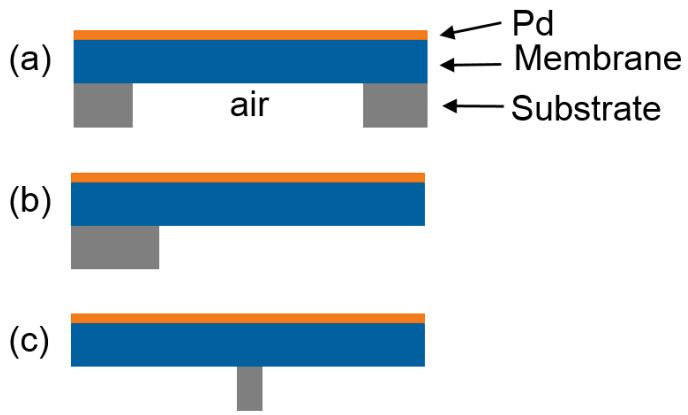

Fig. 29: Various possible cantilever or membrane designs. (a) Suspended membrane. (b) Cantilever. (c) Butterfly or dual cantilever.

sensitive. In addition, for the butterfly and cantilever structures, at large deflections, the membrane may flex out of the optical path of, or scatter the light. This would result in a further change in reflection on top in addition to that due to the refractive index change. The suspended membrane structure would be the most stable, but would also result in smaller deflections for similar dimensions. As a compromise favoring sensitivity, the cantilever structure (Fig. 29b) will be examined in detail. The results can be easily extended to either the butterfly or membrane structures.

5.2 Simulation Methods & Results

Before fabrication, simulations were used to determine suitable design dimensions. These simulations make use of the expansion data acquired through the HILE measurements to model hydrogen exposure. A 3D model of the cantilever was constructed in COMSOL and the thermal module was used to simulate the expansion with hydrogen content taking the place of temperature, and the hydrogen expansion coefficient replacing the thermal expansion coefficient. No reaction from the substrate materials and complete and uniform saturation of the PdH film were assumed.

Several variables exist that can be used to tune the device sensitivity: the cantilever geometry, the thickness of the cantilever beam layer, the thickness of the palladium layer, and the length and width of the cantilever beam. The cantilever beam material is chosen to be SiN_x and literature values for the mechanical properties of the different materials were used such as Poisson's ratio, density, and bulk modulus. These values are listed in Table IV. For the following simulations in this sub-section the model assumes zero stress before hydrogen exposure. In the case of SiN_x or even with the addition of Pd, the cantilever will have some initial deflection depending on deposition conditions and film properties. These effects, to be discussed later, can only be taken into account once the initial stress is known. Figure 30 shows the predicted deflections due to 0.5% H_2 exposure for a cantilever design (Fig. 29b) using the expansion coefficients extracted from the DPM data in Section 4. This particular sensor has a cantilever thickness of 1000 nm with 50 nm of Pd on top. The cantilever showed a maximum tip deflection of 0.6 μm for 0.5% hydrogen.

Table IV
Material Parameters

Material	**Young's Modulus**	**Poisson's Ratio**
Pd	72 GPa	0.44
SiNx	250 GPa	0.23

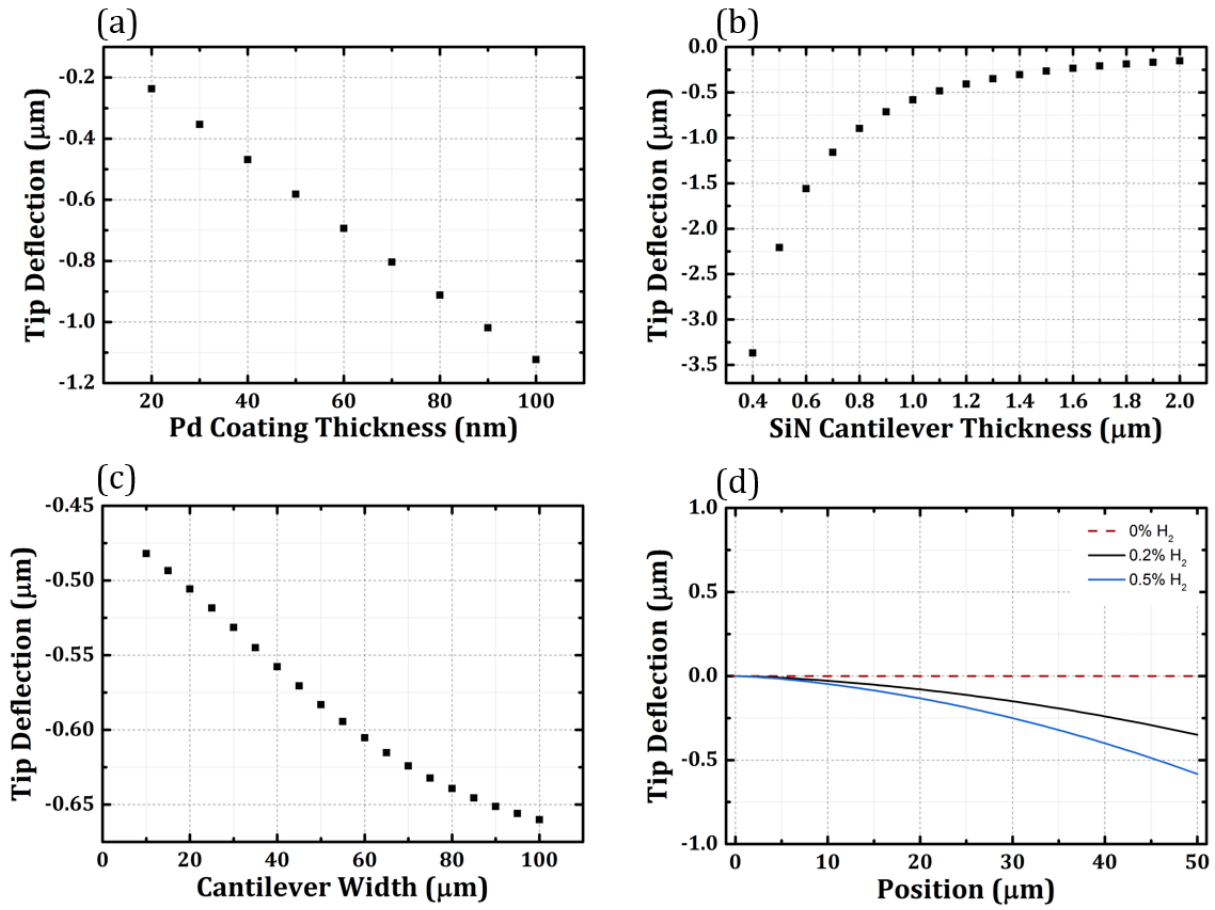

Fig. 30: Simulated deflections for a cantilever with a SiN_x thickness of 1 μm, a Pd thickness of 50 nm, a length of 50 μm, and a width of 50 μm, and hydrogen = 0.5% unless otherwise stated.

Simulations were also done to determine the trends associated with adjusting each variable for exposure to 0.5% H_2 for a 50 μm long cantilever. Figure 30a shows the tip deflection as a function of Pd thickness. The cantilever was 50μm in width, with a thickness of 1μm. As expected, for thicker Pd layers the cantilever flexes more, almost linearly with thickness for these values resulting in a constant deflection sensitivity of 10 nm/nm of Pd thickness. Figure 30b shows that thinner cantilevers should flex more, which is also expected. The sensitivity to the nitride thickness depends on the operating point, but for a 1 μm of SiN_x design, the deflection shows a sensitivity of 1.2 nm/nm of SiN_x thickness. The sensitivity increases to 9 nm/nm of SiN_x at 500nm of nitride. The reduced SiN_x thickness results in a sensitivity that is about $8 = 2^3$ times larger. As will be

explained shortly, the sensitivity is expected to be inversely proportional to the cube of the SiN_x thickness. Figure 30c shows the tip deflection as a function of cantilever width. The sensitivity is 2 nm/μm of width, which is much lower than the other parameters. These values can be better understood if the cantilever is considered as a substrate-thin film system; the dynamics can be approximated by Stoney's equation [62] which showed good agreement with simulations:

$$\kappa = \frac{6h_f\left(1-\nu_s\right)}{E_s h_s^2}\sigma, \qquad (5.1)$$

where σ is the stress in the thin film, h is the layer thickness, κ is the curvature, 's' denotes the substrate, and 'f' denotes the film. In this case, the SiN_x layer is the substrate and the Pd is the film. For a fixed cantilever length, the tip deflection is proportional to the curvature. For a given stress, Eq. (5.1) shows that the curvature varies linearly with the film thickness, and follows an inverse square law for the substrate thickness. Thus, the sensitivity, which is proportional to the derivative of the curvature, should be constant with Pd film thickness and inversely proportional to the cube of the SiN_x thickness. These trends agree with the measured results. The width does not appear in Eq. (5.1) and therefore the tip deflection should not change much as the width is varied. This is also observed in the data because the measured dependence on width is small compared to the other variables and becomes increasingly irrelevant for long cantilevers. Finally, Fig. 30d shows the simulated cantilever profiles for two different hydrogen concentrations. For comparison with the experimental results to be shown later, the sensitivity of the simulated curvature to variations in the important material and design parameters is shown in Table V for a cantilever with a SiN_x thickness of 1μm, a Pd thickness of 50nm at 0.5% hydrogen. The Pd film stress at this concentration was assumed to be 216 MPa based on the measurements in Chapter 4, with an associated curvature of 0.2 mm^{-1}.

Table V
Nano-aperture Sensor Performance

Parameter (x)	**Assumed Value**	**Sensitivity** $\left(\partial\kappa/\partial x\right)$	**Sensitivity (%Δ at κ = 0.2 mm^{-1})**
Pd Thickness $(x = h_f)$	50 nm	4.0 μm^{-1}/nm	2.0 %/nm
SiN Thickness $(x = h_s)$	1000 nm	0.4 μm^{-1}/nm	0.2 %/nm
SiN Young's Modulus $(x = E_s)$	250 GPa	-0.8 μm^{-1}/GPa	-0.4 %/GPa
SiN Poisson Ratio $(x = v_s)$	0.23	-2.6 μm^{-1}/pph	-1.3 %/pph

In addition, **t**here are several other trade-offs not shown in Fig. 30. Firstly, the rupture and tensile strength of the anchor point and Pd layer adhesion strength are not included. For thick Pd layers and long, thin, cantilevers something may break before it achieves the calculated deflection. Secondly, the Pd layer is much denser than the SiN_x layer, hence thick Pd layers and long, thin membranes will not be feasible beyond a certain limit. Deposition of the metal layer may result in collapse of the membrane or cantilever. Based on these simulations cantilevers ranging in length from 15 to 150 μm, in width from 15 to 50 μm, and in thickness from 500 to 1000 nm were fabricated. These devices were then coated with Pd layers 25 – 50 nm thick.

5.3 Fabrication and Experimental Setup

Fabrication of the devices is fairly straightforward from a microelectromechanical systems (MEMS) perspective. Aside from adhesion, the substrate is relatively unimportant for quantifying the dynamics of the cantilever. In light of that, <100> silicon was chosen as there exist many well documented anisotropic etch processes for undercutting this material. Since these devices are not electronic or CMOS-based, KOH was chosen as the etchant for simplicity due to its high selectivity to the <111> plane, as well as its capability to undercut. The [100]:[111] selectivity of KOH is around 100:1 or more, depending on temperature and other factors, which results in the formation

of pyramidal cavities. Furthermore, it has been shown that KOH and similar etchants will attack convex corners, with one proposed mechanism being due to dangling bonds. This will allow for undercutting of the cantilever while maintaining anisotropy at the outer walls of the cavity surrounding the cantilever. While not completely necessary, this feature will allow tighter spacing of different cantilever designs and allow multiple devices to fit into the field of view of the DPM system used to characterize them. It also ensures that the regions around the cantilever used as the reference height do not flex due to undercutting. Finally, SiN_x was chosen as the beam layer since it is unaffected by the KOH etch. While SiO_2 has a small etch rate in KOH, it could still be used due to the high selectivity. However, CVD deposition of SiO_2 usually results in higher film stresses than SiN_x, particularly when compared to mixed frequency SiN_x. For large stresses the initial deflections and stress gradients will complicate modeling, and potentially break or make characterization difficult due to numerical aperture limitations in the DPM system.

Figure 31 shows the process flow for fabricating the structures. First, a bare lightly doped <100> Si wafer was cleaved into bars and various SiN_x thicknesses were deposited at mixed frequency to minimize stress. The final SiN_x layer thickness was confirmed with ellipsometry. The next step was to lithographically define etch windows and dry etch through the SiN_x. With the underlying silicon exposed a KOH wet etch was used to undercut the cantilever. After etching was finished, the Pd layer was deposited using e-beam deposition. Figure 32 shows the undercutting process at various time steps and the computed undercut etch rate. Since the KOH etch is self-limiting and has such high selectivity in this configuration over-etching is not a concern. However, the backside was unprotected so prolonged etching would thin the wafer.

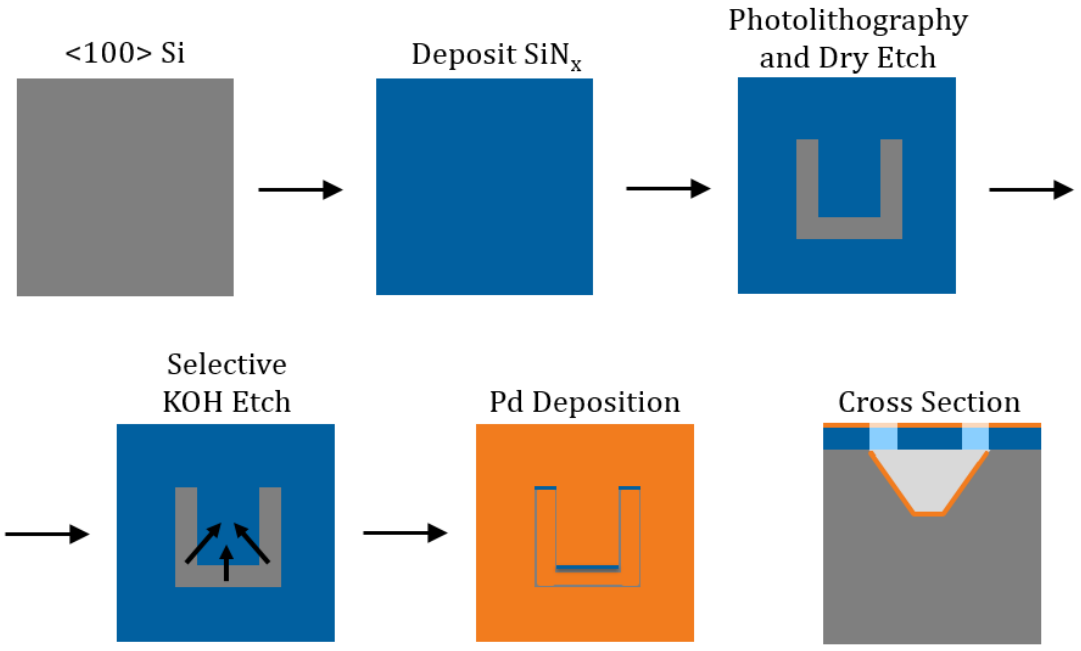

Fig. 31: Fabrication process flow for the SiN_x cantilevers with Pd blanket deposition.

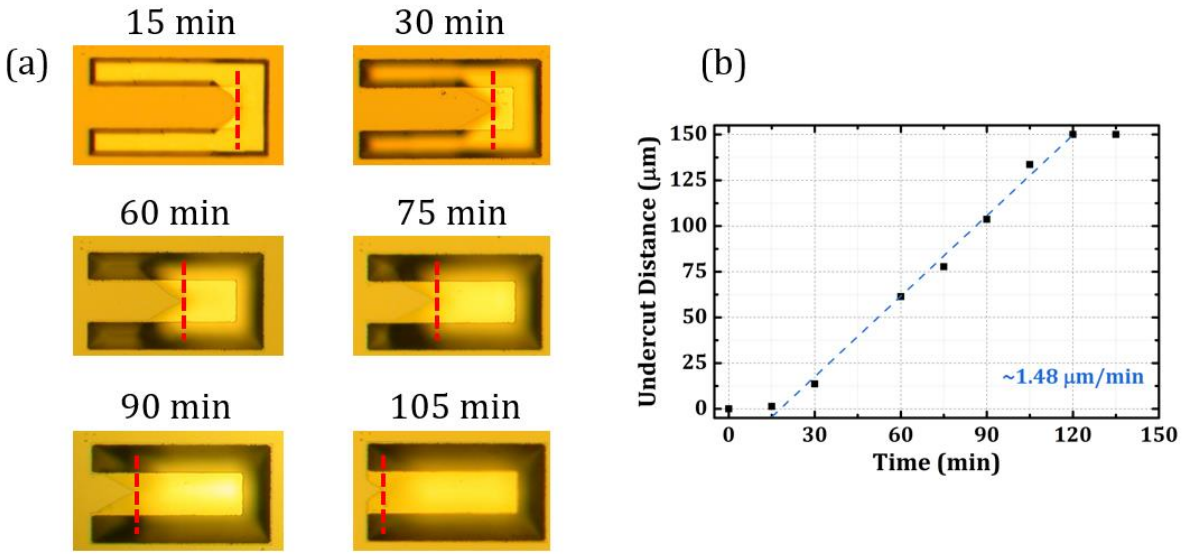

Fig. 32: (a) Optical microscope images of the convex corner undercutting process. (b) Undercut etch rate.

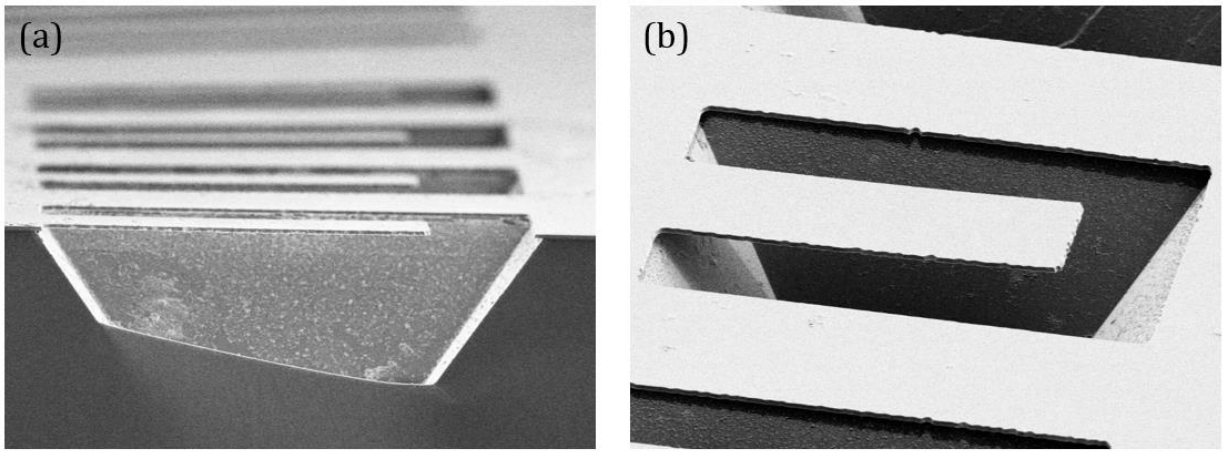

Fig. 33: SEM images of fabricated cantilevers showing final cavity structure, undercutting, and resting contour. (a) Cross section view. (b) Isometric view.

In particular, this process was carried out for two nitride thicknesses which were measured to be 560 nm and 1010 nm. Palladium thicknesses of 25 and 50nm were deposited on each. SEM images of the final devices can be seen in Fig. 33. Upon close inspection, it can be seen that the cantilevers curve slightly upward. This is due to built-in stress in the nitride. In order to measure this built-in stress, a whole wafer was included during the depositions and interferometry was used to measure the topology of the wafer before and after deposition. Using Stoney's equation and the measured radius of curvature, height, and film thicknesses, the initial stress was found to be approximately +190 MPa. This means that the SiN_x layer is compressively strained; however, since the cantilever is not formed by a bimorph the stress gradient determines the deflection of the released structure. In general, as distance from the substrate increases the stress decreases, so the top layer of the cantilever is more tensile than the bottom resulting in the upward deflection relative to the surface as shown. The curvature and height for the same wafer was also measured after the Pd deposition which indicated a slight increase in the intrinsic compressive stress.

Also visible in Fig. 33 is the slight undercutting of the nitride along the <111> plane and the irregular cavity shape due to the undercutting process. Furthermore, it was found that the

cantilevers were slightly narrower (about 5%) than designed, most likely due to the photolithography, either the mask or resist, and dry etching.

After fabrication, the cantilever arrays were mounted in a machined test chamber. The chamber had one inlet and two outlets to facilitate gas purging. One outlet was situated directly over the sample via a small hole in the chamber window. This outlet also served the dual purpose of allowing inspection via DPM without introducing the problem of multiple reflections. The presence of the outlet directly over the sample was found to have no effect on the response as long as the chamber was kept under positive pressure. The measurement setup is similar to that used for the measurements in Chapters 4 and an updated schematic is shown in Fig. 34 with the omission of the DPM configuration which has already been shown**.** However, there are two notable changes in terms of the gas flow. First is in the use of compressed air rather than nitrogen as the ambient gas. The second is in the solenoid configuration, with only one valve used to ensure that no hydrogen flows when the MFC is set to 0 sccm.

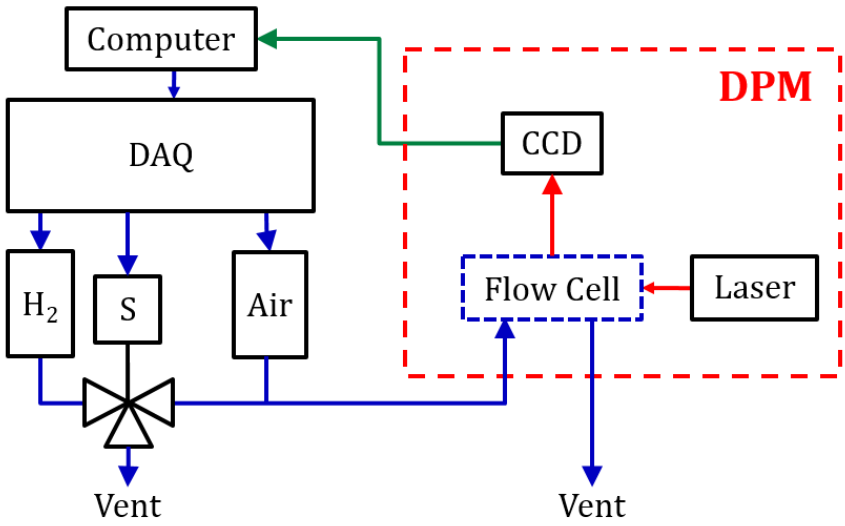

Fig. 34: Experimental setup for measuring the cantilever deflection. The DPM system is omitted for brevity. Blue lines represent gas flow, red lines the optical path, and green lines data acquisition. The 'S' block is a solenoid valve.

The removal of the other solenoid from Fig. 23 is a result of the use of air and the inclusion of the outlet port over the sample. With these two changes, it is no longer possible or necessary to seal off the chamber and stop gas flow. The use of air rather than nitrogen is a major step forward compared to the work presented thus far as it shows these sensors being tested under more realistic operating conditions.

The experimental process consists of alternating pulses of various hydrogen concentrations in air with DPM used to image the cantilever and determine its height and curvature. Test conditions were varied, but typical pulse durations were 30 minutes at a total flow rate of 200 sccm, which was held constant. All of the gas flow was automated via LabVIEW and synced to the time stamp on the DPM images for analysis. For these measurements, a 405 nm laser was used as the illumination source. Figure 35 shows an example of the topology and cantilever profile captured by the system. Due to the very large etch depth (relative to the wavelength) there are significant phase unwrapping errors around the edge of the trench surrounding the cantilevers. To avoid this, the cantilevers were cropped in post processing to remove the edge and then individually phase unwrapped.

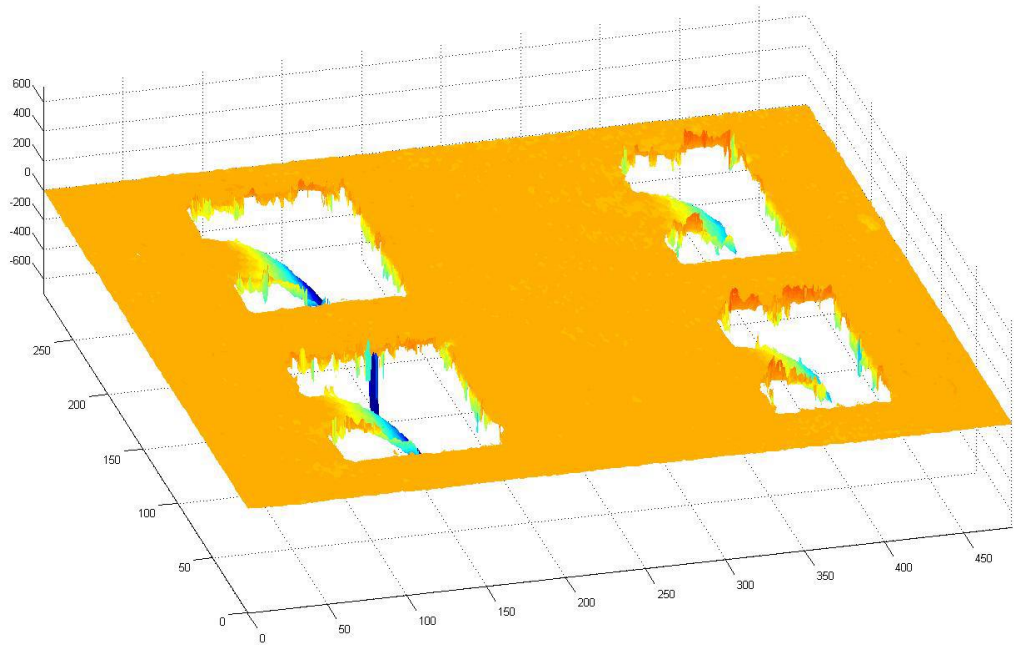

Fig. 35: Sample surface plot acquired by the DPM system. Due to the fabrication design, multiple cantilevers can be measured simultaneously. The phase unwrapping noise shown as the large spikes around the trench is due to the very large etch depths.

5.4 Deflection Measurements

To first step in characterizing the response of the cantilevers is to measure and extract the topography of the cantilever, yielding deflection values as a function of (x,y) where x is measured along the cantilever's length (longitudinally) and y is measured along its width (transversely). Given that the response is along the length of the cantilever, this 2D information can be averaged in the transverse direction to produce a surface profile cross section. It should be noted, however, that although not visible in any of the figures shown thus far, there is a slight cupping effect transverse to the cantilever direction. This effect is negligible for cantilevers with a large length to width aspect ratio. For those at or below a 1:1 aspect ratio the averaging can be confined to the center portion where the height variance due to cupping is minimal. Unless otherwise noted, the

following results are for a cantilever with dimensions L = 75 μm, w = 48 μm, h_s = 1.01 μm, and h_{Pd} = 50 nm. The cantilever was exposed to hydrogen concentrations ranging from 0.2 to 1% in air with pulses each lasting 30 minutes. The profile cross sections and corresponding surface topology can be seen in Fig. 36 for several hydrogen concentrations. The red dashed line denotes zero deflection, or a flat cantilever. Figures 36 (a) and (c) show that the initial deflection is upwards, with a tip deflection of approximately 800nm. This value is computed at the point x = 70 μm across all concentrations to avoid any edge effects. As the hydrogen concentration is increased, the Pd film expands due to HILE. The resulting strain causes a downward deflection of the cantilever. At approximately 0.38% H_2, the cantilever is in a compensated flat state and further increases in hydrogen result in a change in the concavity.

Figure 37 shows the temporal behavior of the structure. Due to the relatively thin Pd layer, the response times were under 5 minutes, an improvement compared to the fiber sensors and expansion measurements in Chapters 2-4. The baseline showed some initial drift but started to stabilize towards the end of the test. The overall response can be seen to start saturating at high concentrations, which is due to approaching the alpha to beta phase transition in the film. This transition was specifically avoided as the resulting plastic deformation could break the device if the stresses became too great. The lower limit of 0.2% H_2 is due to equipment limitations; however, the large response and SNR at this concentration suggests the device would be sensitive to much lower concentrations. A summary of the tip deflection can be seen in Fig. 38 with a dashed line at z = 0 to guide the eye.

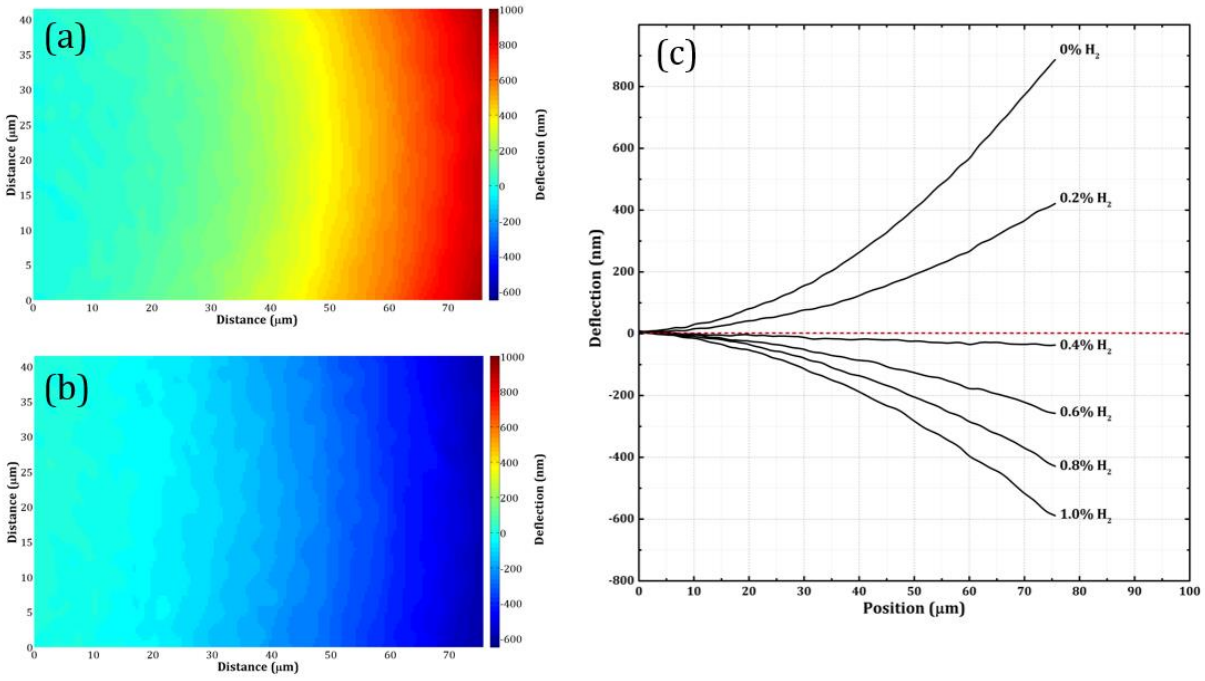

Fig. 36: (a) Cantilever topography for 0% hydrogen. (b) Cantilever topography for 1% hydrogen. (c) Averaged cross section profiles for the cantilever deflection.

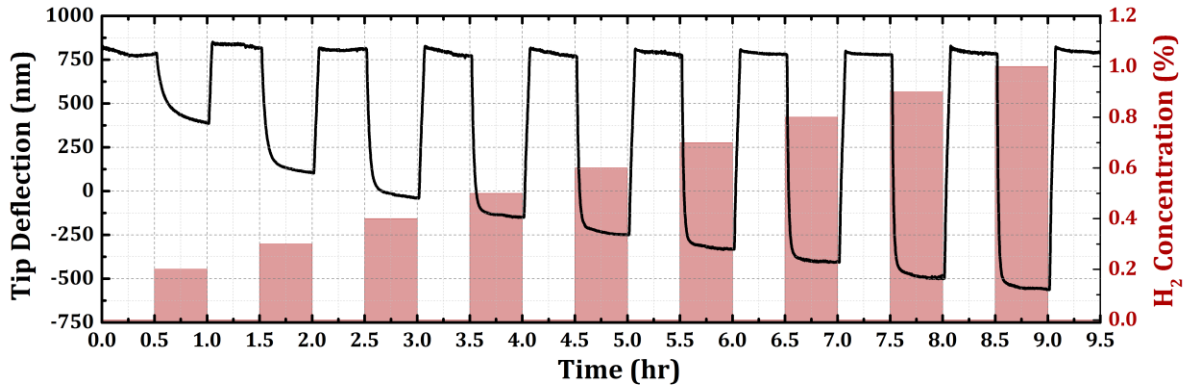

Fig. 37: Pulse response of a cantilever with dimensions L = 75 μm, w = 48 μm, h_s = 1.01 μm, and h_{Pd} = 50 nm.

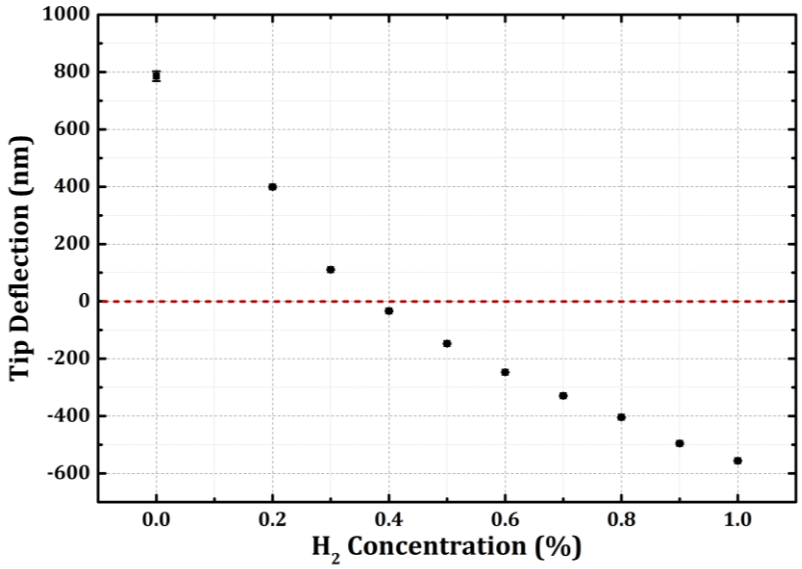

Fig. 38: Summary of the tip deflection measured at x = 70 µm from the anchor. The dashed line represents the z=0 plane.

5.5 Curvature Measurements

Based on experiments and physical models, it can be shown [63] that the deflection of a stressed cantilever as a function of x can be approximated by a quadratic

$$z \simeq \frac{1}{2R} x^2 + \theta x + z_0 , \qquad (5.2)$$

where R is the radius of curvature, z_0 is the initial height, and θ represent initial angles at the anchor point caused by stresses. Assuming perfect leveling of the DPM image, the initial height should be zero. Figure 39 shows the deflection of the cantilever at 1% hydrogen along with a fit to Eq. (5.2). While agreement between the fit and the model is very good, there is slight coupling between the 1st and 2nd degree coefficients, which increases the measured error for κ = 1/R. Combined with noise in the DPM data, this resulted in a fit error of approximately 0.2% for the curvature. Without an empirical or theoretical model for the first degree coefficient, this is difficult to improve and

many factors can affect this coefficient. However, the mean value of the curvature is consistent, as can be seen in the near zero drift of the baseline in Fig. 40**,** which shows the curvature parameter after fitting each frame in Fig. 37. The results of the curvature fitting are summarized in Fig. 41 which shows the curvature vs. hydrogen content**.**

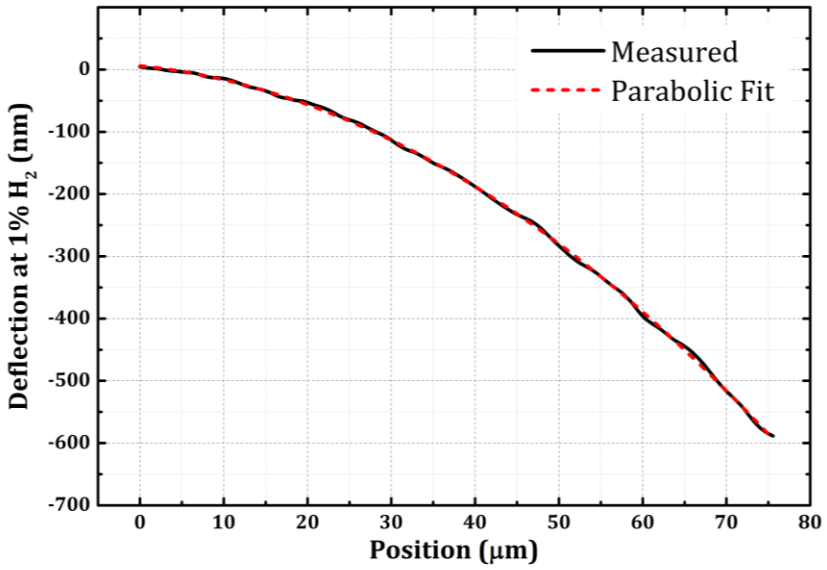

Fig. 39: Measured cross section profile and corresponding parabolic fit used to determine the curvature. Cantilever dimensions L = 75 µm, w = 48 µm, h_s = 1.01 µm, and h_{Pd} = 50 nm.

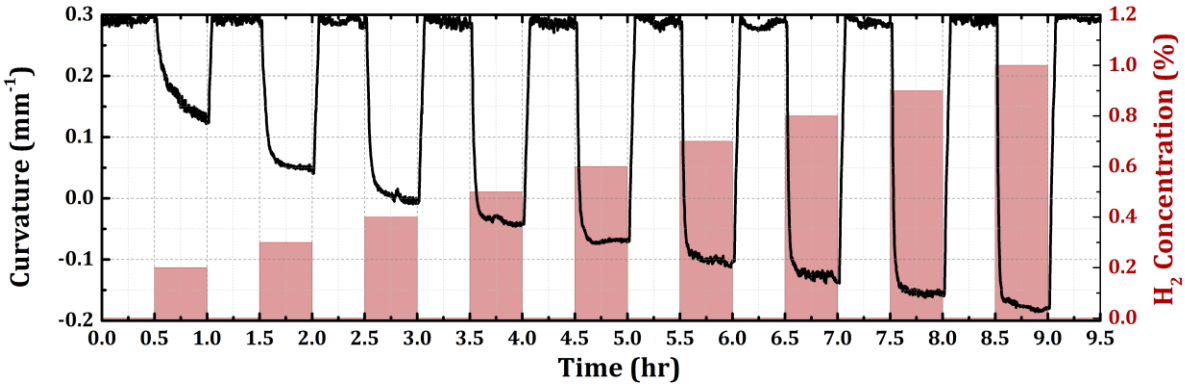

Fig. 40: Temporal response of the measured curvature under hydrogen exposure.

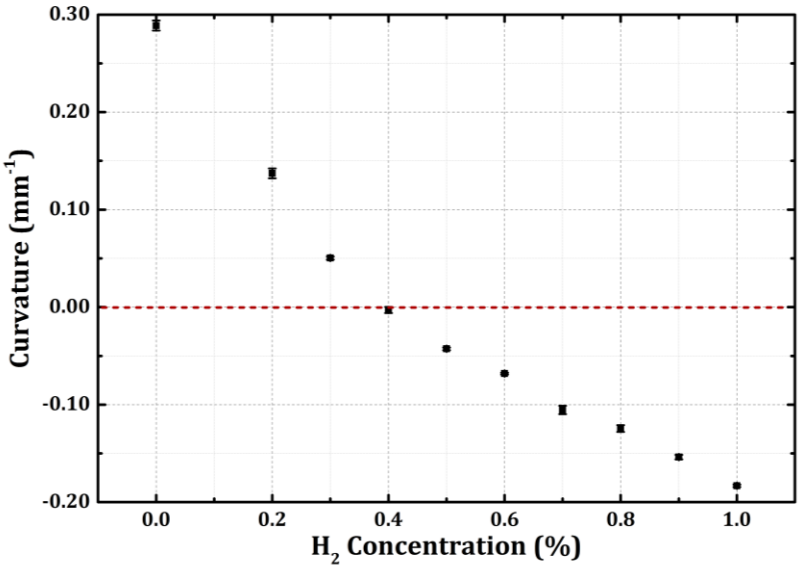

Fig. 41: Summary of the measured curvature as a function of hydrogen concentration. The dashed line represents the z=0 plane.

5.6 Discussion

The overarching goal of the cantilever sensor was to show that by incorporating mechanical effects directly into the design, the response can be more accurately simulated and that it will be consistent across devices with perturbations to the geometry or design. This can be approached in multiple ways. First, the response of the cantilever can be predicted using the previous HILE data. To accomplish this, the expansion coefficients which were extracted in Chapter 4 can be inserted into the COMSOL cantilever simulations along with updated values for the initial stress and curvature and final design dimensions. The only caveat is that the stress gradients producing some of the initial deflection are not known and hence are approximated by an initial torque of the cantilever. These simulation results are shown in Fig. 42 for the same cantilever whose experimental data was shown in Fig. 37. The average relative error for the total change in deflection between theory and experiment is 31.0%. Given that the material properties of the Pd and the SiN_x depend on

deposition conditions and that the stress gradients producing θ are unknown, there is fairly good agreement. Furthermore, these films are substantially thinner than the films from which the expansion coefficient was measured. The thinner films likely behave differently according to Eq. (4.10). Even with more accurate expansion coefficient data, the problem of accurate information about the Young's modulus and stress in the SiN_x, which can vary significantly, would not be solved. Such detailed analysis of the material parameters is beyond the scope of this work. However, these results show that the response of the cantilever device can in fact be predicted to within an order of magnitude from basic principles and DPM measurements of HILE. This is a vast improvement over the fiber sensors first presented and other previous work.

Alternatively, the expansion coefficient can be used to predict the curvature of the cantilever directly using Eq. (5.1) for the Pd/SiN_x structure. Defining the film stress as

$$\sigma = -E_P \cdot \varepsilon(H), \tag{5.3}$$

where E_P is the Young's modulus of the Pd film and $\varepsilon(H)$ is the hydrogen induced strain, the curvature of the cantilever can be predicted according to

$$\kappa - \kappa_0 = -\frac{6E_P h_P (1-\nu_S)}{E_S h_S^2}\alpha H, \tag{5.4}$$

where $\varepsilon(H) = \alpha H$ is used for consistency with the data collected in Chapter 4. The variable h represents layer thickness, E the Young's modulus and ν Poisson's ratio for the materials SiN_x and Pd denoted by the subscripts S and P respectively. The initial curvature is given by κ_0 and the negative sign is because the Pd film is under compressive stress. The benefit of this approach is that the values of the initial stresses and the variable θ do not need to be known, assuming that the Pd layer is in the thin film regime ($h_P \ll h_S$). Using this formulation, the expected curvatures from the HILE data are shown in Fig. 43**.** This resulted in a similar match to the simulated deflection

data, with a relative error of 33.7%. This prediction is still subject to errors resulting from not knowing the Young's modulus of the nitride or Pd layer, the curvature fitting, and more importantly the functional form of the expansion coefficient. According to the sensitivities calculated in Table V, and allowing for nanometer variations in the thicknesses of the Pd film and the SiN_x layer as well as uncertainties in the mechanical properties E and ν, this level of relative error is reasonable.

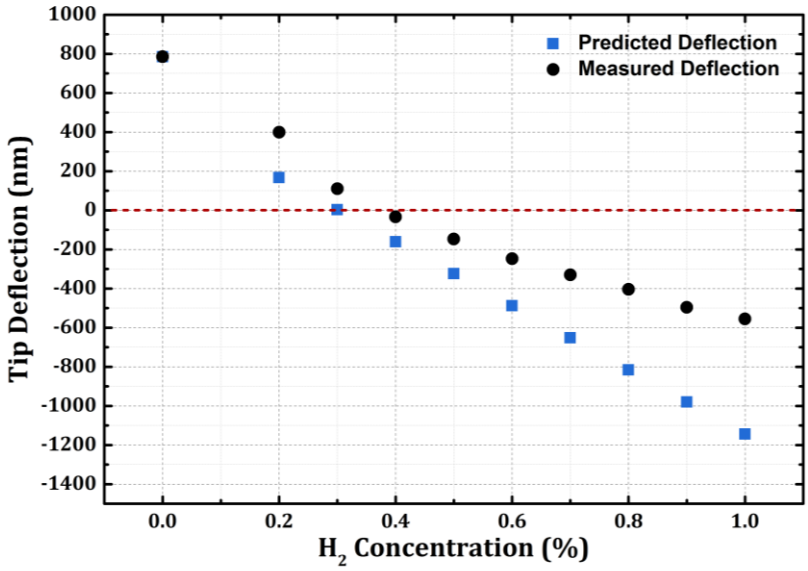

Fig. 42: Measured and predicted deflection at x=70 µm. The deflection is predicted using 3D simulations and the expansion coefficients measured previously. Cantilever dimensions L = 75 µm, w = 48 µm, h_s = 1.01 µm, and h_{Pd} = 50 nm.

To gain more insight into the dependence of expansion on film properties, the DPM data from the cantilever can be used to extract the expansion coefficient in the reverse process. Rearranging Eq. (5.4) gives an expression for α

$$\alpha = -\frac{E_S h_S^2 (\kappa - \kappa_0)}{6 E_P h_P (1-\nu_S)} \frac{1}{H}. \qquad (5.5)$$

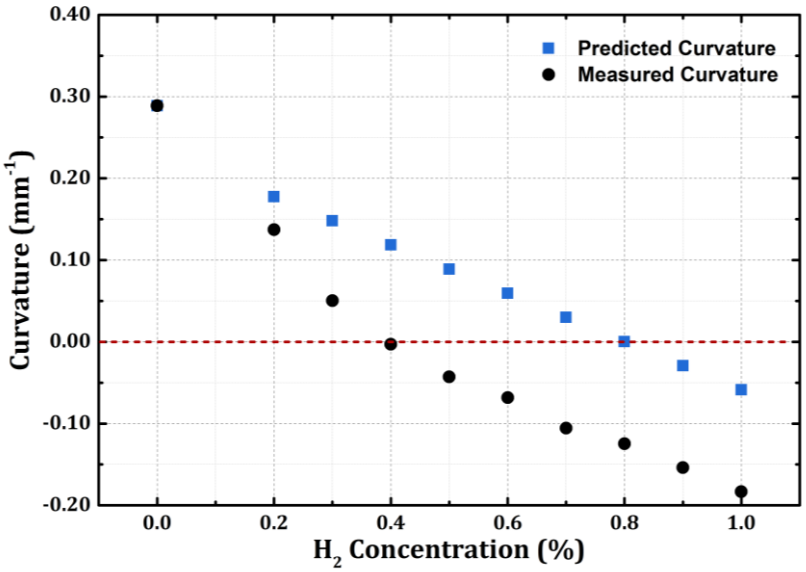

Fig. 43: Measured curvature compared to the curvature predicted by Eq. (5.4) as a function of hydrogen concentration. The dashed line represents the change in concavity of the cantilever.

Using the measured curvature values, the extracted expansion coefficients for the cantilever are shown in Fig. 44 for cantilevers of two different sizes on the sample. Ideally these numbers should be identical; however, at low concentrations they diverge slightly. This is likely due to a combination of the small change in curvature and fit errors.

The expansion coefficient and its variation with hydrogen concentration can then be used to predict the curvature for a sample with different layer thicknesses, which eliminates the error associated with not knowing the Young's modulus or the Poisson's ratio. A cantilever with a measured SiN_x thickness of 560nm and a Pd thickness of 25nm was also fabricated. Figure 45 shows the predicted curvature values using an average of the results in Fig. 44. While the values are closer, this approach still assumes that the expansion of the two films is identical, which Fig. 45 suggests may not be the case.

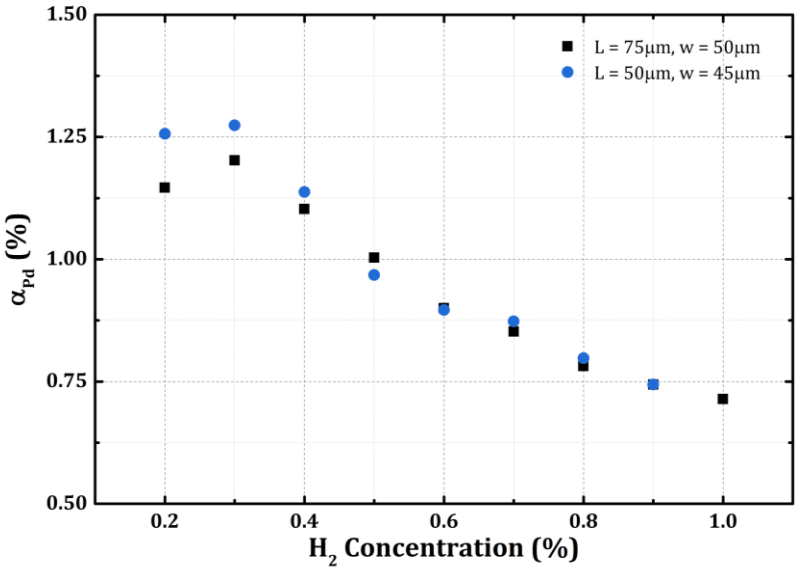

Fig. 44: Expansion coefficient extracted from cantilever curvature using Eq. (5.5).

To further analyze the thin film expansion coefficient, consider the curvature given by Eq. (5.4) which, similar to the microdisk expansion, is directly proportional to the strain and can be differentiated yielding

$$\frac{\partial \kappa}{\partial H}_0 = -\Lambda \frac{\partial \varepsilon}{\partial H}, \tag{5.6}$$

where

$$\Lambda = \frac{6E_P h_P (1-\nu_S)}{E_S h_S^2}, \tag{5.7}$$

This suggests that for curvature values that are linear with H, a similar fitting procedure can be applied to extract the functional dependence of the expansion. The curvature for the 50 nm Pd cantilever is replotted in Fig. 46 which shows a strong linear dependence for H > 0.4%. A similar trend was found for the 25 nm Pd cantilever, which can be seen by comparison in Fig. 45.

The expansion coefficients for the second cantilever were also extracted using Eq. (5.5). Combined with the data from the initial cantilever that had 50 nm of Pd, these values were then fit

according to the strain model that is linear with H_2 concentration in Chapter 4 which previously yielded the relationship

$$\alpha(H) = \alpha_{\max} + \frac{\zeta_0}{H}. \tag{5.8}$$

The results of this fit are shown in Fig. 47 along with the tails of the fits for both cantilevers and the microdisk from Chapter 4. For all three sets of data, Eq. (5.8) fit well and the resulting fit parameters can be found in Table VI. As expected the film thickness has an important effect on the expansion coefficient. Equally interesting is the very strong agreement in the value for $\alpha_{\max}$ which reinforces the validity of the fit. The other fit parameter shows a direct correlation with film thickness: as film thickness decreases, ζ_0 grows larger. The trend seems to be monotonic but with only 3 data points this is only speculation. It does however make sense that this parameter should tend toward zero for thick films, which relates $\alpha_{\max}$ to bulk expansion. Also important to note is that the lattice mismatch between the Pd and the Cr/Ni adhesion layer causes built-in compressive strain in the Pd film at the interface, which has less room to dissipate for thinner films. This implies the average lattice constant should be smaller for thinner films. Using a "ball-in-hole" analogy [64] for hydrogen absorption, the "ball" is the same size for all three films but the "hole" is smaller for thinner films, so the fractional expansion increases.

Table VI
Expansion Coefficient (%) Fit Parameters

$$\alpha(H) = \alpha_{\max} + \frac{\zeta_0}{H}$$

Pd Film	$\alpha_{\max}$	ζ_0	**Fit Range**
25 nm (Cantilever)	0.45 ± 0.02	0.34 ± 0.01	0.4% - 1%
50 nm (Cantilever)	0.45 ± 0.02	0.27 ± 0.01	0.4% - 1%
290 nm (Microdisk)	0.45 ± 0.01	0.08 ± 0.01	0.3% - 0.5%

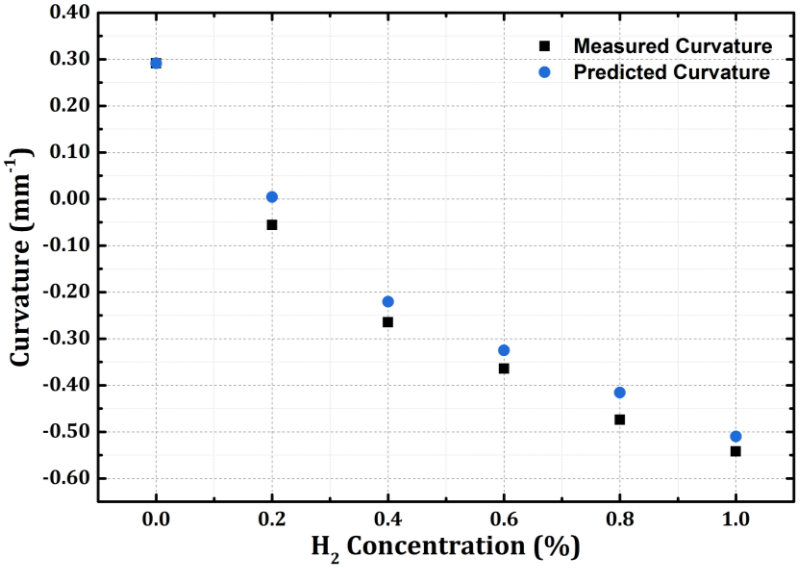

Fig. 45: Predicted curvature values based on the expansion coefficient extracted from a different cantilever geometry.

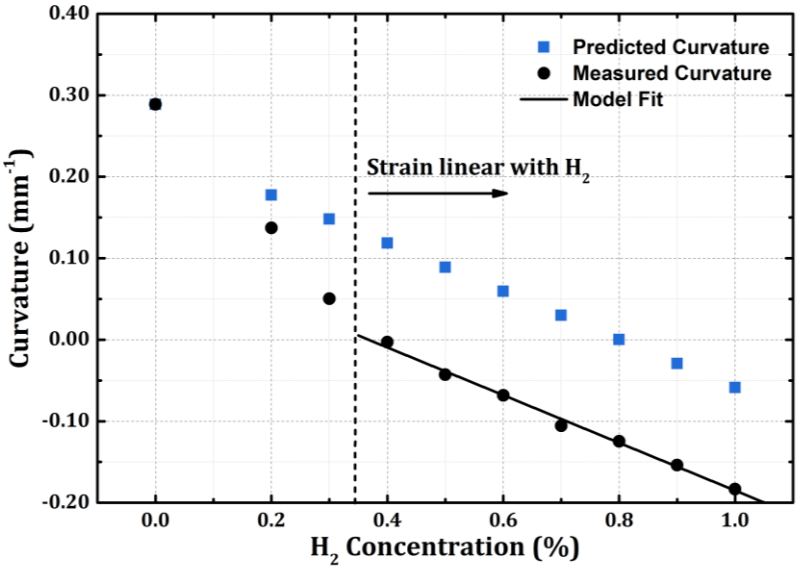

Fig. 46: Fit of the linear portion of the curvature as a function of hydrogen exposure correlating with a strain model that is linear with H_2 concentration.

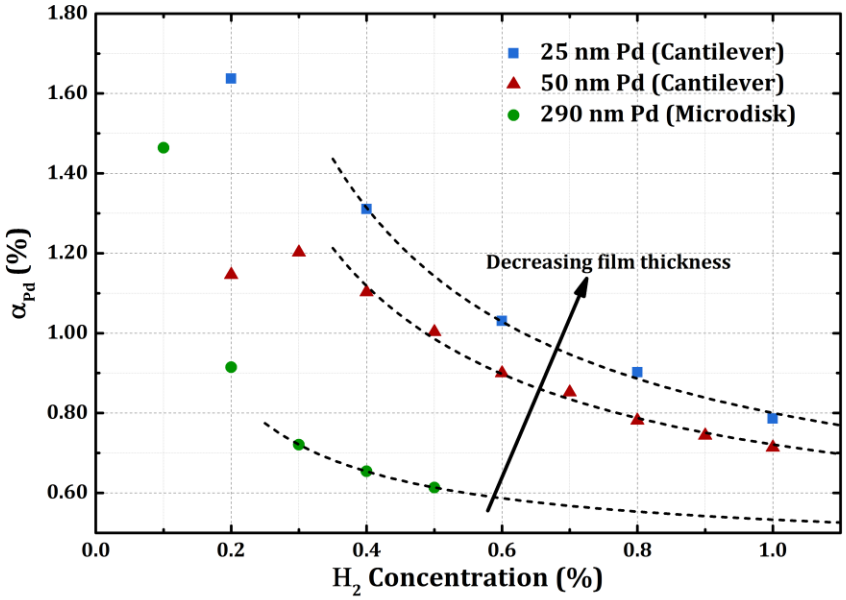

Fig. 47: Summary of the measured expansion coefficients (% expansion as a function of exposure concentration) for different film geometries and thicknesses.

Also important for designing reliable and predictable sensors is repeatability of the response between measurements, and ultimately the ability of the measured responses to be inverted and hydrogen concentrations to be determined without any a priori knowledge. To examine the repeatability of the cantilever sensor, the device was subjected to repeating pulses of 0.5% hydrogen alternating with both air and 1% hydrogen. The results of this pulse test are shown in Fig. 48 and a summary of the response can be seen in Fig. 49. Figure 48 shows a slight drift in the response initially, which is clearer in Fig. 49. However, after a long enough hydrogen exposure the response levels out as shown by pulses 8-10. For the pulses where the response is measured after returning from 1%, rather than from air, the response is slightly different but still relatively stable compared to the measurement error indicated by the error bars. These results are generally consistent with past observations that the Pd based sensors require pre-exposure to hydrogen to remove this initial drift attributed to relaxation of the film. More interesting, however, is the difference in response depending on the previous hydrogen content of the film. This suggests a

memory effect in the lattice such that the response of each pulse cannot be considered independent from the rest. Hypothetically, this could be removed by doing many different sweeps and calculating a response matrix. However, due to the large amount of time required and the relatively small error introduced (on the order of 3-4x the noise level) this analysis was not carried out.

Having established that the baseline of the sensor is stable, a set of random concentrations was chosen to test the predictability of the sensor for both return to zero measurements, as well as sequential random concentrations. The duration of each pulse was limited to a minimum of 20 minutes so that the sensor had time to fully respond. However, given that the 10-90% response times are on the order of 5 minutes, shorter pulses could have been used with the introduction of slightly more error. The measured tip deflection for the random pulse test can be seen in Fig. 50. To determine the hydrogen concentration, the calibration data in Fig. 38 was inverted.

The results of these calculations can be seen in Fig. 51. The slight shoulder seen on the tail end of some of the calculated pulses is a result of the interpolation in the gap between 0 and 0.2%. If measurement data at lower concentrations were available, this effect would be smoothed out. Any calculated negative values were floored to 0% which is why the baseline appears to be exact. There is a similar offset to the response at 0% that occurs when recovering from hydrogen exposure in that the cantilever returns to a state with compressive stress in the Pd layer resulting in more upward deflection. After some time depending on the concentration, this is released and the baseline returns to normal. The error in the calculated hydrogen concentration is summarized in Fig. 52 showing that the hydrogen concentration can be determined with an error in the range of 0-0.04%. This is relatively large compared to the noise in the measured height and curvature values; those factors alone correspond to an uncertainty of 0.003% H_2 for this cantilever. The determined hydrogen concentration is always less than the actual value, suggesting systemic

sources of error such as the memory effect of the Pd film discussed previously – most likely due to the chemistry and thermodynamics of the film.

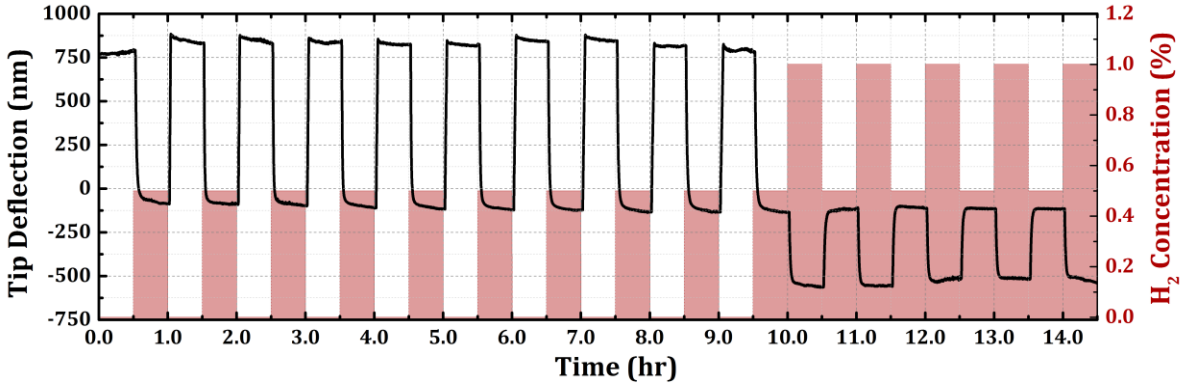

Fig. 48: Temporal response of the tip deflection at x=70 µm for a cantilever with dimensions L = 75 µm, w = 48 µm, h_s = 1.01 µm, and h_{Pd} = 50 nm to repeated hydrogen pulses.

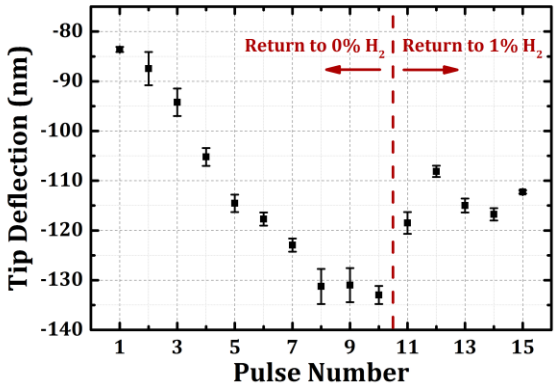

Fig. 49: Tip deflection at 0.5% H_2 as a function of pulse for data shown in Fig. 48.

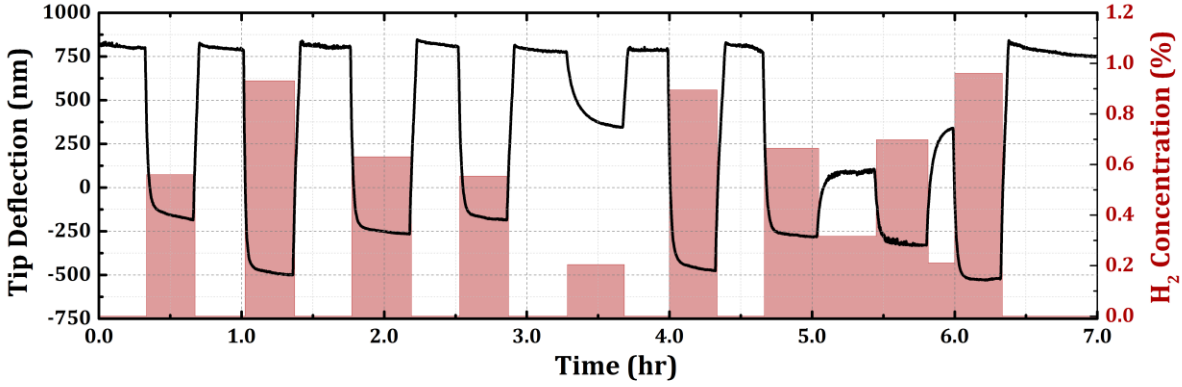

Fig. 50: Temporal response to a random pulse train of H_2.

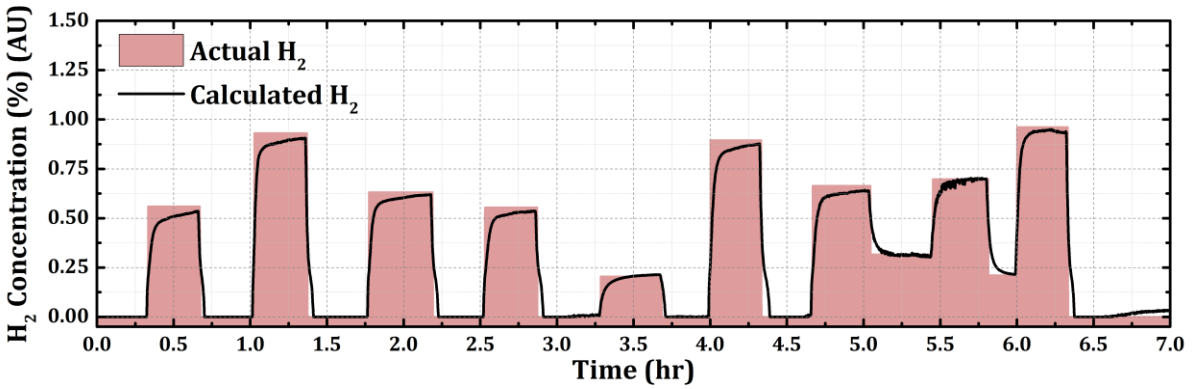

Fig. 51: Calculated hydrogen concentration using the measured tip deflection and the calibration data shown in Fig. 38.

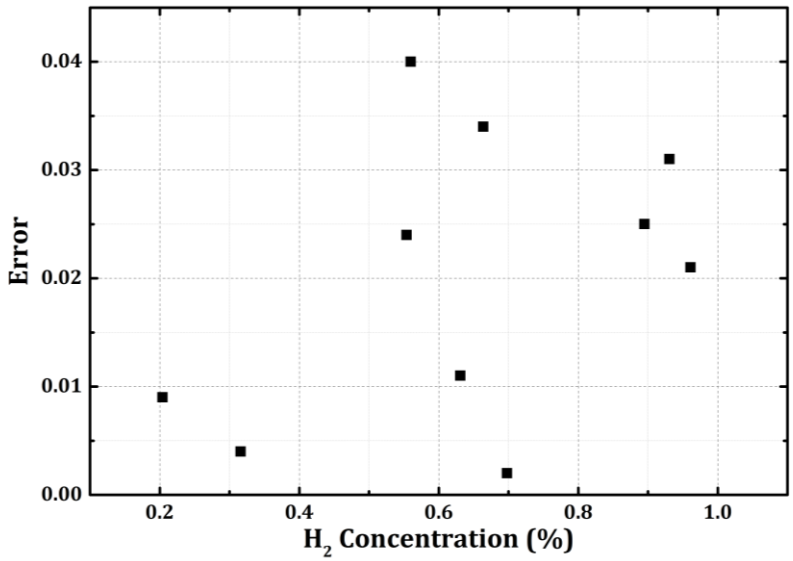

Fig. 52: Error in the calculated hydrogen concentration.

5.7 Low Concentration Measurements

To verify the accuracy of the linear strain assumption, as well as to further test the sensitivity of the cantilever device, lower concentration measurements were carried out by using a different combination of mass flow controllers and a more dilute hydrogen source (0.2% in air). Similar

pulse tests were carried out and the results of these measurements are shown in Fig. 53. Figure 53a shows the temporal response of the curvature and Fig. 53b shows a summary of the results averaged over three pulses. This data shows that the minimum detection limit based on curvature is below 0.025% (250 ppm) hydrogen in air. These curvature values are plotted together with the original data in Fig. 54a, reinforcing the bounds of the linear model used to fit the expansion coefficient. These are plotted as the change in curvature due to a slight drift between the two series of measurements. Figure 54b shows the calculated expansion coefficient for the low and high concentrations.

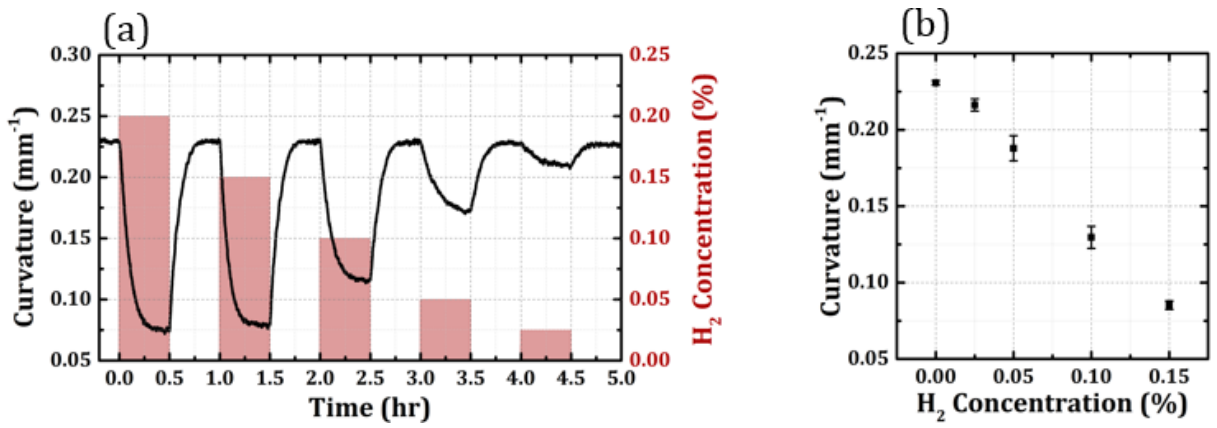

Fig. 53: Temporal response of curvature as a function of time and hydrogen concentration at low concentrations. (b) Summary of the measured curvature.

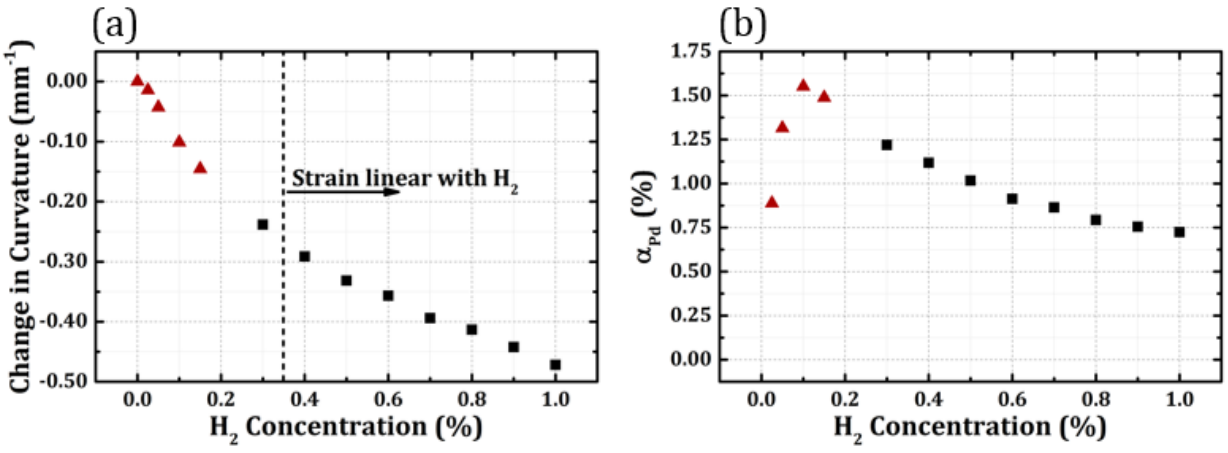

Fig. 54: (a) Change in curvature vs. hydrogen concentration. (b) Calculated expansion coefficient vs. hydrogen concentration. Red triangles indicate the new data.

CHAPTER 6
CONCLUSIONS

This dissertation discusses fabrication and analysis of several palladium based hydrogen sensors as well as potential pitfalls in design. It also explores characterization methods enabling more accurate modeling, specifically concerning the expansion of thin palladium films.

The first design, the nano-aperture sensor, shows the potential sensitivity of Pd based sensors, as well as the need for a more complete model. The improved sensitivity of this device resulted from the inclusion of a resonant structure; however, the behavior could not be modeled from only an optical standpoint, despite various attempts. It was ultimately established that the sensitivity was coupled to microscopic mechanical effects from adhesion and surface blistering, which are random and are very hard to simulate.

In order to better understand what was occurring with the Pd films, characterization was carried out, specifically on the adhesion properties and the expansion of the film. It was found through experiment that the adhesion layer can play a prominent role in the response of the Pd film. A technique was also developed to measure the hydrogen induced lattice expansion using diffraction phase microscopy. Using this data and mechanical models, we were able to extract functional information about the expansion coefficient of thin film palladium, a key parameter in device simulation.

A cantilever sensor was also fabricated and tested, operating based on stress induced deflection. The fundamental behavior of the cantilever sensor was measured and characterized using the same DPM technique and showed reasonable agreement with both the theoretical models and the previous measurements. By designing a sensor with a large macroscopic mechanical

response, the challenges that the nano-aperture sensor experienced in predicting the response were avoided. Both the repeatability and the accuracy of this device were also established while operating in atmospheric conditions. With a suitable fabrication process, a device combining the sensitivity of the nano-aperture sensor with the reliability and predictability of the cantilever structure could be realized.

One such proposed sensor is the integration of a plasmonic hole array onto the cantilever tip, similar to grating based sensors which have been previously studied [65]–[67]. In addition to the vertical displacement, such a device would be sensitive to hydrogen through the change in periodicity of the holes as a result of lattice expansion and substrate warping, the change in phase matching condition introduced by the curvature of the array, and the change in permittivity of the palladium film. The surface plasmon resonance (SPR) condition for the array can be approximated by [26], [68]:

$$\lambda_{peak} \simeq \frac{\Lambda}{\sqrt{i^2 + ij + j^2}} \left(\sqrt{\frac{\varepsilon_{Pd} n^2}{\varepsilon_{Pd} + n^2}} - n \sin \theta_i \right), \qquad (6.1)$$

where Λ is the period of the array, n is the refractive index of the incident dielectric, θ is the incident angle, and ε is the permittivity. The integers *i* and *j* determine the scattering order. Given the sharp resonances of such structures large changes in the reflection and transmission spectra could be produced for small hydrogen concentrations as ε, θ, and Λ will all vary with H_2. Using Eq. (6.1) the required period for resonance at a given wavelength and incident angle (to the substrate) can be calculated from tabulated refractive index data for palladium and the curvatures measured in Chapter 5. Devices have been designed and fabricated according to Eq. (6.1) and literature concerning the spectra shifts due to hole geometry [26] using focused ion beam and can be seen in Fig. 55.

In addition to laying groundwork for sensors such as the proposed SPR-cantilever hybrid, the work presented in this dissertation raises interesting and practical questions about how to reduce the systemic error in Pd-based hydrogen sensors. Specifically, a deeper look can be made into the dynamics of thin film palladium using techniques such as x-ray diffraction (XRD) and transmission electron microscopy (TEM) to characterize the lattice and grain structure and x-ray photoelectron spectroscopy (XPS) to gain more insight into the surface composition of the film. This information could potentially be used to explain the drift seen in experimental measurements and to improve calibration, or to help improve sensor selectivity to variables such as humidity and temperature. Aside from selectivity concerns surrounding temperature, humidity, and other gases which were not studied, the ability to operate in a wide variety of these conditions is also desirable for many sensing applications. Adapting these sensors to operate in harsh environments would be one logical and important next step.

This work was also primarily concerned with low concentration measurements in the α phase of PdH leaving room for research into how to design and build robust sensors that can reliably bridge the α to β phase transition. To this end, a further study of the plastic deformation of the film at high concentrations and the mechanical strength and stability of thin film structures under these conditions would be required. One final mechanical consideration that was touched upon but not fully explored was the effect and role of adhesion and adhesion layers on the expansion of thin films, specifically relating to the induced strain at the interface. This was seen experimentally to affect both the response magnitude and response time.

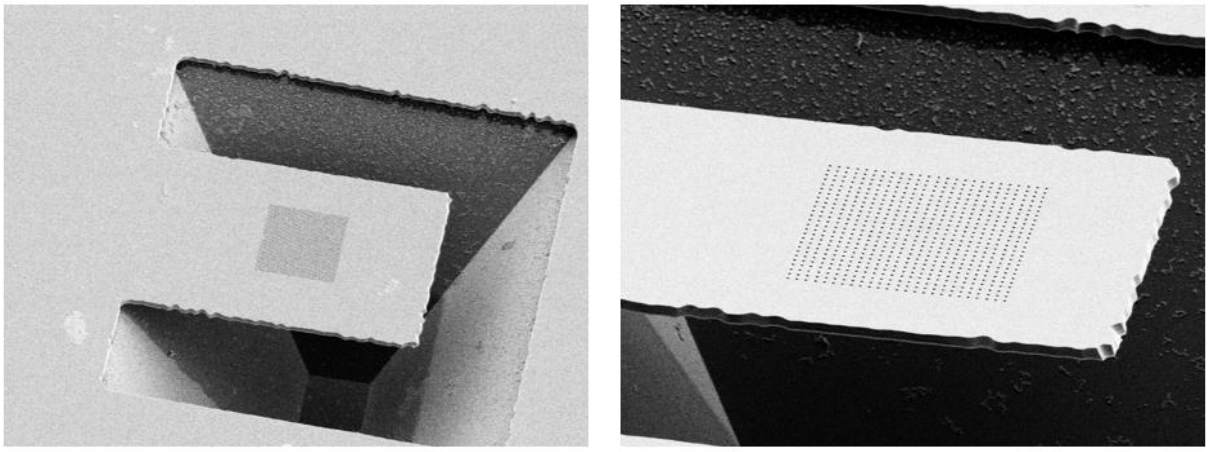

Fig. 55: SEM images of fabricated hybrid SPR-cantilever sensors.

In addition to these potential new areas of research, we believe that the methodologies discussed in this dissertation for empirical data collection in thin films and for optomechanical sensor design will allow for the development of more sensitive and predictable functionalized optomechanical sensors, such as the device in Fig. 55, that can detect, identify, and quantify different gases, chemicals, or biological agents.

REFERENCES

[1] T. Wei, X. Lan, H. Xiao, Y. Han, and H.-L. Tsai, "Optical fiber sensors for high temperature harsh environment sensing," in *2011 IEEE Instrumentation and Measurement Technology Conference (I2MTC)*, 2011, pp. 1–4.

[2] T. N. Veziroğlu and S. Şahi˙n, "21st Century's energy: Hydrogen energy system," *Energy Convers. Manag.*, vol. 49, no. 7, pp. 1820–1831, Jul. 2008.

[3] C. Christofides and A. Mandelis, "Solid-state sensors for trace hydrogen gas detection," *J. Appl. Phys.*, vol. 68, no. 6, p. R1, 1990.

[4] Z. Zhao, Y. Sevryugina, M. A. Carpenter, D. Welch, and H. Xia, "All-optical hydrogen-sensing materials based on tailored palladium alloy thin films," *Anal. Chem.*, vol. 76, no. 21, pp. 6321–6326, Nov. 2004.

[5] G. Choi, G. Jin, S.-H. Park, W. Lee, and J. Park, "Material and sensing properties of Pd-deposited WO3 thin films," *J. Nanosci. Nanotechnol.*, vol. 7, no. 11, pp. 3841–3846, 2007.

[6] J. Dai, M. Yang, Y. Chen, K. Cao, H. Liao, and P. Zhang, "Side-polished fiber Bragg grating hydrogen sensor with WO3-Pd composite film as sensing materials," *Opt. Express*, vol. 19, no. 7, pp. 6141–6148, Mar. 2011.

[7] T. B. Flanagan and W. A. Oates, "The palladium-hydrogen system," *Annu. Rev. Mater. Sci.*, vol. 21, no. 1, pp. 269–304, 1991.

[8] Y. Morita, K. Nakamura, and C. Kim, "Langmuir analysis on hydrogen gas response of palladium-gate FET," *Sens. Actuators B Chem.*, vol. 33, no. 1–3, pp. 96–99, Jul. 1996.

[9] J. F. Lynch and T. B. Flanagan, "Dynamic equilibrium between chemisorbed and absorbed hydrogen in the palladium/hydrogen system," *J. Phys. Chem.*, vol. 77, no. 22, pp. 2628–2634, Oct. 1973.

[10] D. D. Eley, "Molecular hydrogen and metallic surfaces," *J. Phys. Chem.*, vol. 55, no. 6, pp. 1017–1036, Jun. 1951.

[11] E. Wicke, H. Brodowsky, G. Alefeld, and J. Völkl, "Hydrogen in metals II," *Top Appl Phys*, vol. 29, p. 73, 1978.

[12] A. Mandelis and J. A. Garcia, "Pd/PVDF thin film hydrogen sensor based on laser-amplitude-modulated optical-transmittance: dependence on H2 concentration and device physics," *Sens. Actuators B Chem.*, vol. 49, no. 3, pp. 258–267, 1998.

[13] C. Edwards, A. Arbabi, S. J. McKeown, R. Zhou, G. Popescu, and L. L. Goddard, "Optical inspection and metrology using diffraction phase microscopy," in *Surface Analysis Symposium 2013*, Urbana-Champaign, IL, 2013.

[14] C. Edwards, S. J. McKeown, J. Zhou, G. Popescu, and L. L. Goddard, "Observing hydrogen induced deformations in palladium thin-films," presented at the IEEE Photonics Conference 2013, Washington, USA, 2013.

[15] M. Raval, S. McKeown, A. Arbabi, and L. L. Goddard, "Palladium based Fabry-Pérot etalons for hydrogen sensing," presented at the Optical Sensors, Monterey, CA, 2012, p. STh2B.5.

[16] B. G. Griffin, A. Arbabi, A. M. Kasten, K. D. Choquette, and L. L. Goddard, "Hydrogen detection using a functionalized photonic crystal vertical cavity laser," *Quantum Electron. IEEE J. Of*, vol. 48, no. 2, pp. 160–168, 2012.

[17] B. G. Griffin, A. Arbabi, and L. L. Goddard, "Engineering the sensitivity and response time of edge-emitting laser hydrogen sensors," *IEEE Sens. J.*, vol. 13, no. 8, pp. 3098–3105, 2013.

[18] B. G. Griffin, A. Arbabi, and L. L. Goddard, "Functionalized distributed feedback lasers for hydrogen sensing applications," presented at the IEEE Photonics Conference.

[19] B. Griffin, A. Arbabi, and L. Goddard, "Coupled mode analysis of a distributed Bragg reflector laser for hydrogen detection," presented at the OSA Optical Sensors Conference, Monterey CA, 2012.
[20] S. J. McKeown and L. L. Goddard, "Hydrogen detection using polarization diversity via a subwavelength fiber aperture," *IEEE Photonics J.*, vol. 4, no. 5, pp. 1752–1761, 2012.
[21] N. Liu, M. L. Tang, M. Hentschel, H. Giessen, and A. P. Alivisatos, "Nanoantenna-enhanced gas sensing in a single tailored nanofocus," *Nat. Mater.*, vol. 10, no. 8, pp. 631–636, 2011.
[22] M. A. Butler, "Optical fiber hydrogen sensor," *Appl. Phys. Lett.*, vol. 45, no. 10, pp. 1007–1009, 1984.
[23] M. A. Butler, "Micromirror optical-fiber hydrogen sensor," *Sens. Actuators B Chem.*, vol. 22, no. 2, pp. 155–163, Nov. 1994.
[24] T. Hübert, L. Boon-Brett, G. Black, and U. Banach, "Hydrogen sensors – A review," *Sens. Actuators B Chem.*, vol. 157, no. 2, pp. 329–352, Oct. 2011.
[25] S. F. Silva, L. Coelho, O. Frazão, J. L. Santos, and F. X. Malcata, "A review of palladium-based fiber-optic sensors for molecular hydrogen detection," *Sens. J. IEEE*, vol. 12, no. 1, pp. 93–102, 2012.
[26] C. Genet and T. W. Ebbesen, "Light in tiny holes," *Nature*, vol. 445, no. 7123, pp. 39–46, Jan. 2007.
[27] H. A. Bethe, "Theory of diffraction by small holes," *Phys. Rev.*, vol. 66, no. 7–8, pp. 163–182, Oct. 1944.
[28] W. L. Barnes, A. Dereux, and T. W. Ebbesen, "Surface plasmon subwavelength optics," *Nature*, vol. 424, no. 6950, pp. 824–830, Aug. 2003.
[29] R. F. Oulton, V. J. Sorger, D. A. Genov, D. F. P. Pile, and X. Zhang, "A hybrid plasmonic waveguide for subwavelength confinement and long-range propagation," *Nat. Photonics*, vol. 2, no. 8, pp. 496–500, Aug. 2008.
[30] A. Chandran, E. S. Barnard, J. S. White, and M. L. Brongersma, "Metal-dielectric-metal surface plasmon-polariton resonators," *Phys. Rev. B*, vol. 85, no. 8, p. 085416, Feb. 2012.
[31] X. Shi and L. Hesselink, "Design of a C aperture to achieve λ/10 resolution and resonant transmission," *JOSA B*, vol. 21, no. 7, pp. 1305–1317, 2004.
[32] X. Shi, L. Hesselink, and R. L. Thornton, "Ultrahigh light transmission through a C-shaped nanoaperture," *Opt. Lett.*, vol. 28, no. 15, pp. 1320–1322, 2003.
[33] Y. Xie, A. Zakharian, J. Moloney, and M. Mansuripur, "Transmission of light through slit apertures in metallic films," *Opt. Express*, vol. 12, no. 25, pp. 6106–6121, Dec. 2004.
[34] G. Veronis and S. Fan, "Modes of subwavelength plasmonic slot waveguides," *J. Light. Technol.*, vol. 25, no. 9, pp. 2511–2521, Sep. 2007.
[35] E. X. Jin and X. Xu, "Finite-difference time-domain studies on optical transmission through planar nano-apertures in a metal film," *Jpn. J. Appl. Phys.*, vol. 43, no. 1, pp. 407–417, 2004.
[36] L. Goddard and S. Mckeown, "Sub-wavelength patterned fiber tips for hydrogen detection," presented at the (invited) 1st Annual World Congress of Nano Science and Technology (Nano S&T), Dalian, China, 2011.
[37] S. McKeown and L. Goddard, "Nano-aperture fiber hydrogen sensors," presented at the Nanoelectronic Devices for Defense and Security Conference (NanoDDS), New York, NY, 2011.
[38] S. McKeown, "Fiber optic hydrogen sensing utilizing facet etched palladium nano-apertures," Master's Thesis, University of Illinois at Urbana-Champaign, 2011.
[39] Steven J. McKeown and Lynford L. Goddard, "Hydrogen detection using a single palladium nano-aperture on a fiber tip," in *Lab on Fiber Technology*, 1st ed., vol. 56, Springer International Publishing, 2015, pp. 181–208.
[40] S. J. McKeown, B. G. Griffin, and L. L. Goddard, "Fiber optic hydrogen sensor utilizing facet-etched metal nano-apertures," in *IEEE Photonics Society, 2010 23rd Annual Meeting of the*, Denver, CO, 2010, pp. 730–731.
[41] S. L. Chuang, *Physics of Photonic Devices*. John Wiley & Sons, 2012.

[42] A. D. Rakic, A. B. Djurisic, J. M. Elazar, and M. L. Majewski, "Optical properties of metallic films for vertical-cavity optoelectronic devices," *Appl. Opt.*, vol. 37, no. 22, pp. 5271–5283, Aug. 1998.
[43] L. L. Goddard, K. Wong, A. Garg, E. Behymer, G. Cole, and T. Bond, "Measurements of the complex refractive index of Pd and Pt films in air and upon adsorption of H2 gas," presented at the IEEE LEOS Annual Meeting, Newport Beach, CA, 2008.
[44] P. Tobiška, O. Hugon, A. Trouillet, and H. Gagnaire, "An integrated optic hydrogen sensor based on SPR on palladium," *Sens. Actuators B Chem.*, vol. 74, no. 1, pp. 168–172, 2001.
[45] Y. Fu and N. K. A. Bryan, "Investigation of physical properties of quartz after focused ion beam bombardment," *Appl. Phys. B*, vol. 80, no. 4–5, pp. 581–585, Feb. 2005.
[46] R. J. Smith and D. A. Otterson, "The effect of hydrogen on the tensile properties of palladium," *J. Common Met.*, vol. 24, no. 4, pp. 419–426, Aug. 1971.
[47] A. Hubaux and G. Vos, "Decision and detection limits for calibration curves," *Anal. Chem.*, vol. 42, no. 8, pp. 849–855, 1970.
[48] M.-F. Xue, Y. M. Kang, A. Arbabi, S. J. McKeown, L. L. Goddard, and J.-M. Jin, "Fast and accurate finite element analysis of large-scale three-dimensional photonic devices with a robust domain decomposition method," *Opt. Express*, vol. 22, no. 4, p. 4437, Feb. 2014.
[49] M. Wang and Y. Feng, "Palladium–silver thin film for hydrogen sensing," *Sens. Actuators B Chem.*, vol. 123, no. 1, pp. 101–106, 2007.
[50] C. Edwards, S. J. McKeown, J. Zhou, G. Popescu, and L. L. Goddard, "In situ measurements of the axial expansion of palladium microdisks during hydrogen exposure using diffraction phase microscopy," *Opt. Mater. Express*, vol. 4, no. 12, p. 2559, Dec. 2014.
[51] C. Edwards, A. Arbabi, G. Popescu, and L. L. Goddard, "Optically monitoring and controlling nanoscale topography during semiconductor etching," *Light Sci. Appl.*, vol. 1, no. 9, p. e30, Sep. 2012.
[52] C. Edwards, K. Wang, R. Zhou, B. Bhaduri, G. Popescu, and L. L. Goddard, "Digital projection photochemical etching defines gray-scale features," *Opt. Express*, vol. 21, no. 11, pp. 13547–13554, Jun. 2013.
[53] R. Zhou, C. Edwards, A. Arbabi, G. Popescu, and L. L. Goddard, "Detecting 20 nm wide defects in large area nanopatterns using optical interferometric microscopy," *Nano Lett.*, vol. 13, no. 8, pp. 3716–3721, Aug. 2013.
[54] B. Bhaduri, C. Edwards, H. Pham, R. Zhou, T. H. Nguyen, L. L. Goddard, and G. Popescu, "Diffraction phase microscopy: principles and applications in materials and life sciences," *Adv. Opt. Photonics*, vol. 6, no. 1, p. 57, Mar. 2014.
[55] C. Edwards, R. Zhou, S.-W. Hwang, S. J. McKeown, K. Wang, B. Bhaduri, R. Ganti, P. J. Yunker, A. G. Yodh, J. A. Rogers, L. L. Goddard, and G. Popescu, "Diffraction phase microscopy: monitoring nanoscale dynamics in materials science [Invited]," *Appl. Opt.*, vol. 53, no. 27, p. G33, Sep. 2014.
[56] C. Edwards, B. Bhaduri, B. G. Griffin, L. L. Goddard, and G. Popescu, "Epi-illumination diffraction phase microscopy with white light," *Opt. Lett.*, vol. 39, no. 21, pp. 6162–6165, Nov. 2014.
[57] M. Pedersen, W. Olthuis, and P. Bergveld, "On the mechanical behaviour of thin perforated plates and their application in silicon condenser microphones," *Sens. Actuators Phys.*, vol. 54, no. 1–3, pp. 499–504, Jun. 1996.
[58] R. F. S. Hearmon, "The elastic constants of anisotropic materials—II," *Adv. Phys.*, vol. 5, no. 19, pp. 323–382, Jul. 1956.
[59] D. R. Baselt, B. Fruhberger, E. Klaassen, S. Cemalovic, C. L. Britton Jr., S. V. Patel, T. E. Mlsna, D. McCorkle, and B. Warmack, "Design and performance of a microcantilever-based hydrogen sensor," *Sens. Actuators B Chem.*, vol. 88, no. 2, pp. 120–131, Jan. 2003.
[60] J. Henriksson, L. G. Villanueva, and J. Brugger, "Ultra-low power hydrogen sensing based on a palladium-coated nanomechanical beam resonator," *Nanoscale*, vol. 4, no. 16, pp. 5059–5064, Jul. 2012.

[61] S. Okuyama, Y. Mitobe, K. Okuyama, and K. Matsushita, “Hydrogen gas sensing using a Pd-coated cantilever,” *Jpn. J. Appl. Phys.*, vol. 39, no. 6R, p. 3584, Jun. 2000.
[62] X. Feng, Y. Huang, and A. J. Rosakis, “On the Stoney formula for a thin film/substrate system with nonuniform substrate thickness,” *J. Appl. Mech.*, vol. 74, no. 6, p. 1276, 2007.
[63] P. Ferraro and W. Osten, “Digital holography and its application in MEMS/MOEMS inspection,” in *Optical Inspection of Microsystems*, vol. 109, W. Osten, Ed. CRC Press, 2006, pp. 351–425.
[64] J. P. Hirth, “Effects of hydrogen on the properties of iron and steel,” *Metall. Trans. A*, vol. 11, no. 6, pp. 861–890, Jun. 1980.
[65] K. Lin, Y. Lu, J. Chen, R. Zheng, P. Wang, and H. Ming, “Surface plasmon resonance hydrogen sensor based on metallic grating with high sensitivity,” *Opt. Express*, vol. 16, no. 23, pp. 18599–18604, Nov. 2008.
[66] M. E. Stewart, C. R. Anderton, L. B. Thompson, J. Maria, S. K. Gray, J. A. Rogers, and R. G. Nuzzo, “Nanostructured plasmonic sensors,” *Chem. Rev.*, vol. 108, no. 2, pp. 494–521, Feb. 2008.
[67] A. Tittl, P. Mai, R. Taubert, D. Dregely, N. Liu, and H. Giessen, “Palladium-based plasmonic perfect absorber in the visible wavelength range and its application to hydrogen sensing,” *Nano Lett.*, vol. 11, no. 10, pp. 4366–4369, Oct. 2011.
[68] J. M. McMahon, J. Henzie, T. W. Odom, G. C. Schatz, and S. K. Gray, “Tailoring the sensing capabilities of nanohole arrays in gold films with Rayleigh anomaly-surface plasmon polaritons,” *Opt. Express*, vol. 15, no. 26, pp. 18119–18129, Dec. 2007.